Phonon heat conduction probed by means of an electro-thermal method involving deposited micro and nanowires

Wassim Jaber

N°d'ordre NNT : 2016LYSEI109

THESE de DOCTORAT DE L'UNIVERSITE DE LYON
opérée au sein de
L'INSA de Lyon

Ecole Doctorale ED 162
MEGA de Lyon

Spécialité de doctorat : Energétique
Discipline : Thermique

Soutenue publiquement le 25/10/2016, par :

Wassim JABER

Phonon heat conduction probed by means of an electro-thermal method involving deposited micro and nanowires

---

Devant le jury composé de :

BOURGEOIS	Olivier	Directeur de recherche (Institut Néel Grenoble)	Rapporteur
CHAPUIS	Pierre-Olivier	Chargé de recherche (CETHIL Lyon)	Co-directeur de thèse
CHEVALIER	Céline	Ingénieur de recherche (INL Lyon)	Examinateur
DUQUESNE	Jean-Yves	Chargé de recherche (Institut des NanoSciences Paris)	Examinateur
VAILLON	Rodolphe	Directeur de recherche (CETHIL Lyon)	Directeur de thèse
VAIRAC	Pascal	Professeur (FEMTO – ST Besançon)	Rapporteur
ABO RAS	Mohamad	Ingénieur (Nanotest Berlin)	Invité

Département FEDORA – INSA Lyon – Ecoles Doctorales – Quinquennal 2016-2020

SIGLE	ECOLE DOCTORALE	NOM ET COORDONNEES DU RESPONSABLE
CHIMIE	**CHIMIE DE LYON** **http://www.edchimie-lyon.fr** Sec : Renée EL MELHEM Bat Blaise Pascal 3e étage 04 72 43 80 46 INSA : R. GOURDON secretariat@edchimie-lyon.fr	M. Stéphane DANIELE Institut de Recherches sur la Catalyse et l'Environnement de Lyon IRCELYON-UMR 5256 Équipe CDFA 2 avenue Albert Einstein 69626 Villeurbanne cedex directeur@edchimie-lyon.fr
E.E.A.	**ELECTRONIQUE, ELECTROTECHNIQUE, AUTOMATIQUE** **http://edeea.ec-lyon.fr** Sec : M.C. HAVGOUDOUKIAN Ecole-doctorale.eea@ec-lyon.fr	M. Gérard SCORLETTI Ecole Centrale de Lyon 36 avenue Guy de Collongue 69134 ECULLY Tél : 04.72.18 60.97 Fax : 04 78 43 37 17 Gerard.scorletti@ec-lyon.fr
E2M2	**EVOLUTION, ECOSYSTEME, MICROBIOLOGIE, MODELISATION** **http://e2m2.universite-lyon.fr** Sec : Bat Atrium – UCB Lyon 1 04.72.44.83.62 INSA : S. REVERCHON secretariat.e2m2@univ-lyon.fr	Mme Gudrun BORNETTE CNRS UMR 5023 LEHNA Université Claude Bernard Lyon 1 1 Bât Forel 43 bd du 11 novembre 1918 69622 VILLEURBANNE Cédex Tél : 06.07.53.89.13 e2m2@univ-lyon1.fr
EDISS	**INTERDISCIPLINAIRE SCIENCES-SANTE** **http://www.ediss-lyon.fr** Sec : Bat Atrium – UCB Lyon 1 04 72 44 83 62 INSA : Safia.ait-chalal@univ-lyon1.fr	Mme Emmanuelle CANET-SOULAS INSERM U1060, CarMeN lab, Univ. Lyon 1 Bâtiment IMBL 11 avenue Jean Capelle INSA de Lyon 696621 Villeurbanne Tél : 04.72.11.90.13 Emmanuelle.canet@univ-lyon1.fr
INFOMATHS	**INFORMATIQUE ET MATHEMATIQUES** **http://infomaths.univ-lyon1.fr** Sec : Renée EL MELHEM Bat Blaise Pascal 3e étage infomaths@univ-lyon1.fr	Mme Sylvie CALABRETTO LIRIS – INSA de Lyon Bat Blaise Pascal 7 avenue Jean Capelle 69622 VILLEURBANNE Cedex Tél : 04.72. 43. 80. 46 Fax 04 72 43 16 87 Sylvie.calabretto@insa-lyon.fr
Matériaux	**MATERIAUX DE LYON** **http://ed34.universite-lyon.fr** Sec : M. LABOUNE PM : 71.70 –Fax : 87.12 Bat. Direction 1er étage Ed.materiaux@insa-lyon.fr	M. Jean-Yves BUFFIERE INSA de Lyon MATEIS Bâtiment Saint Exupéry 7 avenue Jean Capelle 69621 VILLEURBANNE Cedex Tél : 04.72.43 71.70 Fax 04 72 43 85 28 Ed.materiaux@insa-lyon.fr
MEGA	**MECANIQUE, ENERGETIQUE, GENIE CIVIL, ACOUSTIQUE** **http://mega.universite-lyon.fr** Sec : M. LABOUNE PM : 71.70 –Fax : 87.12 Bat. Direction 1er étage mega@insa-lyon.fr	M. Philippe BOISSE INSA de Lyon Laboratoire LAMCOS Bâtiment Jacquard 25 bis avenue Jean Capelle 69621 VILLEURBANNE Cedex Tél : 04.72 .43.71.70 Fax : 04 72 43 72 37 Philippe.boisse@insa-lyon.fr
ScSo	**ScSo*** **http://recherche.univ-lyon2.fr/scso/** Sec : Viviane POLSINELLI Brigitte DUBOIS INSA : J.Y. TOUSSAINT viviane.polsinelli@univ-lyon2.fr	Mme Isabelle VON BUELTZINGLOEWEN Université Lyon 2 86 rue Pasteur 69365 LYON Cedex 07 Tél : 04.78.77.23.86 Fax : 04.37.28.04.48

*ScSo : Histoire, Géographie, Aménagement, Urbanisme, Archéologie, Science politique, Sociologie, Anthropologie

Acknowledgements

"Energy flows where attention goes"

Really, it's a great sense of honor and modesty to stay with you for the duration of this thesis. My experience at CETHIL was awesome because all of you. The words may not be sufficient to express how I am grateful, to Dr. P. Olivier Chapuis for his great leadership. I thank him so much for offering me this important subject and for his guidance through his very contribution to the filed of heat transfer at micro and nanoscale. He gave me a great resources and freedom to accomplish this job. I thank him for his confidence, patience, constructive discussion and the ultimate support. I am so lucky person to work with him.

I would to extend my gratitude to Prof. Rodolphe Vaillon who was my official supervisor for his support and encouragement. I thank all the members of our MiNT group (Micro and Nano Scale Heat Transfer group).

I am also very grateful to the members of the jury: Pascal Vairac, Olivier Bourgeois, Jean–Yves Duquesne, Céline Chevalier and Mohamad Abo Ras for reviewing and commenting on this manuscript.

This thesis is the result of many experiences I encountered during the period of my work at the CETHIL laboratory. I wish to acknowledge many remarkable individuals who helped me to achieve the works that are presented in this manuscript.

- Dr Céline Chevalier and Mr Pierre Cremillieu for the nanolines.
- Mr Khaled Ayadi, Ms Joëlle Grégoire, Dr Patrick Pittet, Mr Jérôme Degouttes, Mr Nicolas Terrier, Dr Céline Chevalier and Dr Jean–Louis Leclercq from NanoLyon platform for the microlines.
- Mr Pascal Bevilacqua (AMPERE) and Ms Irène Peck (CIME) for the bonding.
- Dr Elyes Nefzaoui (ESIEE) for the simulations with the EPRT.
- Dr Francois Rousset (Mathematica).

- Mr Christophe Ducat from Atelier, Mr Bernard Lacroix and Mr Bertrand Lecareux in CETHIL.

I appreciate the great moments I had with different persons in the lab. Thanks to Jocelyn Bonjour, the director of the lab, for his understanding and listening ear. Thanks to Corinne Dayeyan for her support and administrative help. I also thank the other members in the secretary office who always helped me with different tasks. I especially mention Sophie Grenier, Florence Canale ...

Special thanks to every one of my friends for the good moments that we shared together. Nabil Djati, Maria Cristina Muresan, Christophe Kinkelin, David Renahy, Eloise Guen, Ali Assy, Mouhannad Massoud, Kassem Moghrabi, Mohammad Haidar, Iman Abdallah, Khodor Hodroj, Ali Hallal and Fatima Ibrahim ....Thank you all.

I would like to thank my parents whose presence during my defence meant a lot to me. Thank you for supporting and encouraging me during all these years no matter what I say I can not thank you enough.

Finally, a special thank you to sir Baqiyatallah and I hope to see him soon.

Abstract

The context of this PhD is the reduction of sizes involved in material development and the confinement of heat in modern devices, which are known to lead to the apparition of hot spots. The goal is to investigate heat conduction from micro- to nanoscale wide Joule-heated wires standing on flat layered materials. A particular focus is given to the analysis of phonon heat dissipation when departing from the well-known Fourier diffusive conduction and entering the ballistic regime.

The manuscript starts with a summary of the main observed effects on the effective thermal conductivity in nanoscale materials, especially in light of the values of thermally-averaged phonon mean free paths and the associated Knudsen number. Then the advantages and drawbacks of various measurement techniques are discussed. The analysis of the experimental configuration requires 2D analytical and 3D finite-element method based numerical studies of diffusive heat conduction from a finite source into a medium. Limitations of the 3ω method due to wire length, substrate geometry and thin oxide layers are highlighted. The electro-thermal setup developed and the procedure used to deposit the devices on top of the samples are then detailed. A set of well-known materials with mean free path ranging from few nanometers to hundreds of nanometers is characterized with microwires. The thermal conduction properties of multilayer materials are investigated. Heat dissipation from finite sources on top of silicon substrates is then measured as a function of temperature. The mean free path is known to become large when temperature decreases. As a result, this configuration provides clues for understanding heat conduction from ballistic sources. The observed behavior is very different from the one predicted by Fourier's law and shows a strong reduction of the dissipation. It is found that the results are comparable to earlier measurements involving ridges. They are analyzed with various levels of approximations of predictions using the Boltzmann transport equation.

The results obtained may be useful in many fields, in particular for electronics and thermoelectric designs.

Keywords: nanoscale thermal transport, microscale heat transfer, phonon heat conduction, thermal conductivity, four–probe electrical technique

Contents

List of Figures

List of Tables

Nomenclature

Abbreviation	**Term**
AFM	Atomic Force Microscope
AC	Alternating current
ALD	Atomic Layer Deposition
DC	Direct current
DOM	Discrete ordinates method
EBL	Electron beam lithography
ESD	ElectroStatic Discharges
FEM	Finite element method
LIA	Lock-in amplifier
LTE	Local thermal equilibrium
PTS	Photo–Thermal spectroscopy
PCB	Printed Circuit Board
SEM	Scanning Electron Microscope
SThM	Scanning Thermal Microscopy
TBR	Thermal Boundary Resistance
TCR	Temperature coefficient of resistance
TDTR	Time Domain Thermo–Reflectance
TTR	Transient Thermo–Reflectance
TTG	Transient Thermal Grating

Symbols	Units	Description
b	m	Heater half-width
C	$\mathrm{J.Kg^{-1}.K^{-1}}$	Heat capacity
C_V	$\mathrm{J.kg^{-1}.K^{-1}}$	Heat capacity at constant volume
D	$\mathrm{m^2.s^{-1}}$	Thermal diffusivity
d_S	m	Substrate thickness
d_f	m	Heater thickness
d_F	m	Film thickness
$D(\omega)$	–	Density of states (DOS) for phonons
E	J	Energy of phonon
f	–	Distribution function
f^0	–	Distribution function at equilibrium
$\hbar$	J.s	Reduced Planck constant
I_0	–	Bessel function of the second kind of order zero
k_B	s	Boltzmann constant
Kn	–	Knudsen number
K_0	–	Bessel function of the first kind of order zero
n	–	Number of phonon modes
P	W	Power
q	$\mathrm{m^{-1}}$	Thermal wavenumber
q	$\mathrm{W.m^{-2}}$	Heat flux
R_F	$\mathrm{W^{-1}.m^2.K}$	Thin film thermal resistance
T	K	Temperature
t	s	Time
U	J	Internal energy
V	$\mathrm{m^3}$	Volume
V_0	V	Electrical potential at room temperature
$V_{1\omega}$	V	First harmonic voltage
$V_{3\omega}$	V	Third harmonic voltage
ν	$\mathrm{m.s^{-1}}$	Speed of sound, or group velocity

Greek letters

α	–	Transmissivity
β	1.0484	Constant

θ	$^\circ$	Scatter angle of phonons
θ_D	K	Debye temperature
$\bar{\theta}_{ac}$	K	Average temperature
θ_{DC}	K	DC temperature
κ	$\mathrm{W.m^{-1}.K^{-1}}$	Thermal conductivity
κ_{eff}	$\mathrm{W.m^{-1}.K^{-1}}$	Effective thermal conductivity
κ_D	$\mathrm{m^{-1}}$	Debye wave vector of phonons
λ	m	Wavelength
Λ	m	Mean free path
$\bar{\Lambda}$	m	Average mean free path
μ	$\mathrm{m^2.V^{-1}.s^{-1}}$	Mobility
μ_e	$\mathrm{m^2.V^{-1}.s^{-1}}$	Electron mobility
μ_h	$\mathrm{m^2.V^{-1}.s^{-1}}$	Hole mobility
ξ_E	$\mathrm{eV.K^{-1}}$	Specific constant for Si
ξ	0.922	Constant
ρ	$\mathrm{kg.m^{-3}}$	Density
τ	s	Relaxation time
ρ	$\mathrm{kg.m^{-3}}$	Density
υ	$\mathrm{m.s^{-1}}$	Velocity of acoustic phonons
Υ	$\mathrm{W.m^{-3}}$	Volumetric electrical power
$\varphi_{2\omega}$	–	Phase angle
ω	$\mathrm{rad.s^{-1}}$	Angular frequency
ω_D	$\mathrm{s^{-1}}$	Debye angular frequency

Introduction

Thermal transport at nanoscale is differing from that at macroscale. This is due to the fact that the characteristic lengths associated to the energy carriers are of the same order as that of the material sizes in nanomaterials and nanodevices. Modifications from the usual behaviors at macroscale have been evidenced both for thermal radiation and for heat conduction. It is very important to find the new laws governing heat transfer at nanoscale due to the widespread use of nanomaterials in many industrial sectors, especially in electronics–related fields. Many opportunities can also be envisaged for nanomaterials due to these novel behaviors, for example in the design of new thermoelectric materials.

Fourier's diffusive law of heat conduction was shown to fail when material dimensions become comparable to, or smaller than, the mean free path of the energy carriers [1, 2, 3, 4, 5, 6, 7] . In solids, the reason for the apparent reduction of heat transfer capability is due in particular to phonon–boundary scattering. The phenomenon was studied early at low temperature, and was demonstrated in the last two decades in academic configurations such as nanowires and thin layers. In many operating devices, the confinement of heat in nanostructures is leading to strong constriction effects which cannot be described simply by extrapolating the results found for those simple academic configurations. Effective parameters included in usual numerical tools, which were found for example by studying experimentally in the 1D configuration, cannot be used for 2D and 3D configurations. As a result, the management of heat generated in nanodevices has

become a very important challenge for electronics and efficient tools for predicting heat dissipation in complex geometries are still lacking. Despite many progresses in the recent years, a complete fundamental description of heat conduction at nanoscale in complex geometries is still elusive, and current efforts are limited by a lack of experimental validation.

This thesis takes place in the framework of the current works aiming at understanding and controlling heat dissipation from nanoscale heat sources. We are interested in studying phonon heat conduction into a solid from a surface where a micro–to–nanoscale heat source dissipates. Different transport regimes are considered, from the usual diffusive one to the ballistic one. To this aim, Joule heated metallic deposited on top of surfaces. This allows performing the measurements with a four–probe electro-thermal technique similar to the 3ω method used to determine the thermal conductivity of flat samples [8, 9, 10]. If the mean free path is larger than the wire width, heat dissipates from 2D sub–mean free path sources. The investigations are performed as a function of temperature, which allows tuning the mean free path, and wire widths. A key dimensionless number is the ratio of the mean free path to the wire width, known as the Knudsen number. To provide an idea, the average mean free path of silicon at room temperature is considered to be close to 300 nm. Wire widths from 10 microns down to tens of nanometers have therefore been fabricated. The temperature range of the study is [10–300] K. While silicon is the material of choice here due to its wide use in electronics, some other materials with specific average mean free paths have also been considered for particular tasks.

The manuscript is divided into six chapters. An introduction to phonon heat conduction at nanoscale is provided in the first chapter. Key features of the diffusive and ballistic regimes, mostly in the monodimensional configuration, are presented. The importance of boundary thermal resistances is highlighted. Some domains of application where nanoscale heat conduction is significant are mentioned. The second chapter tackles the experimental techniques that can be used for studying thermal transport in low–dimensional systems. A comparison between the optical techniques, which have been successful in recent years, and the non-optical techniques is introduced. The goal is to explain when electro–thermal probing can highlight novel physical results. These two first chapters allow putting forward the state of the art in nanoscale heat conduction studies of interest for our work.

Chapters 3 and 4 are devoted to the design and fabrication of the electro–thermal de-

vices. The third chapter is dedicated to analytical and numerical analysis of diffusive heat conduction in idealized and real geometries considered in the experimental work. Main features of the bidimensional geometry are introduced, for simple substrates or multilayer materials involving thin films. Then the impact of real 3D dissipation, thin oxide layers, device thickness and device connection are investigated and proven to be very significant under some conditions. The result of the work is that an experiment can be fully simulated despite its complexity when in non-ideal configuration. Chapter 4 is devoted to the fabrication and characterization of the deposited devices. Non-thermal requirements which are also needed are mentioned and the lithography techniques considered are described. Wire widths down to few dozens of nanometers were fabricated.

Chapters 5 and 6 present the experimental results and their interpretations. Chapter 5 is devoted to micrometer–wide metallic wires for various lengths ranging from few tens of micrometers to millimeter ones. The experimental setup is detailed. Temperature coefficients of electrical resistances are measured for different wires as a function of temperature. Room–temperature tests with the standard 3ω methods are performed and results of measurements on a multilayer are provided. Chapter 6 deals with the nanometer–wide metallic wires. The observed thermal conductances are very different from those predicted by the usual Fourier law. A comparison with ballistic predictions and with earlier measurements involving a ridge configuration is performed.

The manuscript ends with a discussion of the main points raised and the prospects that this work opens.

References

[1] Y. K. Koh and D. G. Cahill, *Frequency dependence of the thermal conductivity of semiconductor alloys*, Physical Review B **76**, 075207 (2007).

[2] A. J. Minnich, J. Johnson, A. Schmidt, K. Esfarjani, M. Dresselhaus, K. A. Nelson and G. Chen, *Thermal conductivity spectroscopy technique to measure phonon mean free paths*, Physical Review Letters **107**, 095901 (2011).

[3] A. Minnich, *Determining phonon mean free paths from observations of quasiballistic thermal transport*, Physical Review Letters **109**, 205901 (2012).

[4] K. T. Regner, D. P. Sellan, Z. Su, C. H. Amon, A. J. McGaughey and J. A. Malen, *Broadband phonon mean free path contributions to thermal conductivity measured using frequency domain thermoreflectance*, Nature communications **4**, 1640 (2013).

[5] J. P. Freedman, J. H. Leach, E. A. Preble, Z. Sitar, R. F. Davis and J. A. Malen, *Universal phonon mean free path spectra in crystalline semiconductors at high temperature*, Scientific reports **3**, (2013).

[6] A. J. Minnich, *Towards a microscopic understanding of phonon heat conduction*, arXiv:1405.0532 (2014).

[7] K. M. Hoogeboom-Pot, J. N. Hernandez-Charpak, X. Gu, T. D. Frazer, E. H. Anderson, W. Chao, R. W. Falcone, R. Yang, M. M. Murnane, H. C. Kapteyn *et al.*, *A new regime of nanoscale thermal transport: Collective diffusion increases dissipation efficiency*, Proceedings of the National Academy of Sciences **112**, 4846 (2015).

[8] D. G. Cahill, *Thermal conductivity measurement from 30 to 750 K: the 3ω method*, Review of Scientific Instruments **61**, 802 (1990).

[9] T. Borca-Tasciuc, A. Kumar and G. Chen, *Data reduction in 3ω method for thin-film thermal conductivity determination*, Review of Scientific Instruments **72**, 2139 (2001).

[10] J.-Y. Duquesne, D. Fournier and C. Frétigny, *Analytical solutions of the heat diffusion equation for 3ω method geometry*, Journal of Applied Physics **108**, 086104 (2010).

CHAPTER 1

Nanoscale heat conduction

Rapid advancement of modern technology has raised the scientific demands to understand the fundamental description of heat conduction and energy transport at nanoscale. Controlling the thermophysical properties of materials at nanoscale for thermoelectricity or nanophononics and for lowering hot spots in electronic devices has shown a great promise for improving the performances and reliability. Recent studies have shown that thermal transport at the nanoscale is fundamentally different from that at the macroscale. In fact, the nanostructuration permits a large reduction of the effective thermal conductivity, which results from phonon–boundary scattering, particularly at low temperatures. The phenomenon has been demonstrated in nanowires and thin films.

This chapter provides an overview of micro- and nanoscale thermal transport phenomena. In the first section, we introduce the physical mechanism of heat conduction. In the second section, the (kinetic) theory of phonons for heat conduction is introduced and values of the mean free path are given. In the third section, we provide an overview on different transport regimes depending on the material size and on the characteristic lengths of phonons. The size effect of nanostructures on thermal transport at room and low temperatures is discussed in Section 1.4. In Section 1.5, we introduce different high thermal conductivity materials that can be useful for our experiments. Finally, we

focus on the applications of nanostructures and show their importances in advanced technologies.

1.1. Heat diffusion

Heat conduction is represented by the flow of the thermal energy caused by a temperature difference. In the case of diffusion a thermal gradient is required. The process is then modeled on the basis of Fourier's law:

$$\overrightarrow{q} = -\kappa \overrightarrow{\nabla} T, \tag{1.1}$$

where q $[\mathrm{W.m^{-2}}]$ is the density of heat flux, κ $[\mathrm{W.m^{-1}.K^{-1}}]$ is the thermal conductivity and $\overrightarrow{\nabla}\mathrm{T}$ $[\mathrm{K}]$ is the gradient of temperature. The physical mechanism of conduction is often explained by considering a gas inside a medium and studying it by using the concepts of thermodynamics. The particles may occupy the space between two surfaces of different temperatures. Particles that are localized at the location where the temperature is higher will possess more energy than particles localized close to the surface at lower temperature, as shown in Fig. 1.1. As a consequence, this will create energy transfer due to random motion of the particles (or heat carriers) from higher energy states to the less energized ones of the colder regions [1, 2, 3].

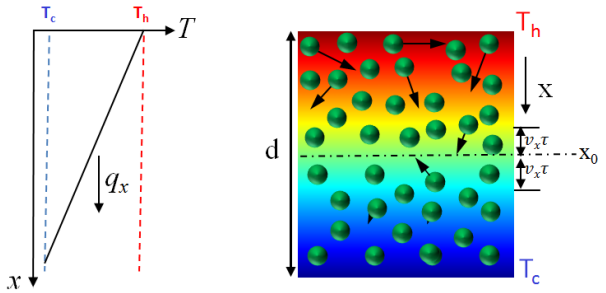

Figure 1.1. *Heat conduction process through particles*

Considering a one-dimensional model as shown in Fig. 1.1, Fourier's law is expressed by:

$$q_x = -\kappa \frac{dT}{dx}, \tag{1.2}$$

where d is the characteristic length of the substance.

1.2. Kinetic theory for heat diffusion in a gas

Solids are composed of a crystalline structure or an amorphous one. The thermal gradient is imposed on the structure, creates lattice vibrations, i.e., phonons. Indeed, thermal energy transport happens when the lattice is driven out of the equilibrium. This energy is transported by the heat carriers. Basically, each heat carrier has a position $\overrightarrow{r}$ and a momentum velocity $\overrightarrow{p}$.

1.2.1. Simplified model for a gas

Let us assume that n is the concentration number of heat carriers and c is the heat capacity of each carrier. We take an imaginary surface perpendicular to the heat flow direction (see Fig. 1.1). By considering a positive direction, the carriers from both sides will cover a distance $\upsilon_x \tau$ before colliding at $x = x_0$. υ_x is the particle speed in x-direction and τ is the relaxation time, i.e. the average time needed by the particles before the collision (free collision time). Half of the particles arriving from the high temperature side carry an energy $E(T(x_0 - \upsilon_x \tau))$ per particle while the other half of particles arriving from the low temperature side carry an energy $E(T(x_0 + \upsilon_x \tau))$. Thereby, the net energy flux across the surface at $x = x_0$ is given by

$$q_x = \frac{1}{2}(nE\upsilon_x)|_{x_0 - \upsilon_x \tau} - \frac{1}{2}(nE\upsilon_x)|_{x_0 + \upsilon_x \tau}, \tag{1.3}$$

where the factor $\frac{1}{2}$ implies that half of carriers are moving in the positive x-direction while the other half of the carriers are moving in the negative x-direction. As a result:

$$q_x = -\upsilon_x \tau \frac{d(nE\upsilon_x)}{dx}, \tag{1.4}$$

where $nE = U$ is the local energy density per unit volume. Assuming that velocity v_x of the heat carriers is independent of direction, then $v_x^2 = \frac{v^2}{3}$ and v^2 represent an average velocity over all random particles. Therefore Eq. 1.4 becomes

$$q_x = -\frac{v^2\tau}{3}\frac{dU}{dT}\frac{dT}{dx}, \tag{1.5}$$

$C = \frac{dU}{dT}$ is the total heat capacity, which is equal to density ρ times the specific heat per unit mass c of the heat carrier: $C = \rho c$. Then

$$q_x = -\frac{v^2\tau}{3}C\frac{dT}{dx}. \tag{1.6}$$

Combining Eqs 1.2 and 1.6 leads to Fourier's law:

$$-\frac{v^2\tau}{3}C\frac{dT}{dx} = -\kappa\frac{dT}{dx}. \tag{1.7}$$

Hence, the kinetic theory yields the following expression of thermal thermal conductivity:

$$\kappa = \frac{1}{3}Cv^2\tau = \frac{1}{3}Cv\Lambda, \tag{1.8}$$

where Λ is the mean free path (MFP) – the characteristic length for energy carriers to scatter with each other.

1.2.2. Case of phonons

The first thermal conductivity models for bulk solids were based on the solution of the phonon Boltzmann transport equation (BTE) under the single mode relaxation time approximation [4, 5, 6, 7]. Eq. 1.1 establishes a link between the heat flux, $\overrightarrow{q}$, and the temperature gradient, $\overrightarrow{\nabla}T$. The total thermal conductivity can be expressed as a sum of all heat carrier contributions. In bulk solids, the energy carriers are the phonons, i.e., waves associated to the displacement of the atoms. Consider the temperature gradient along the x–direction, then the thermal current can be expressed as:

$$\overrightarrow{q} = \frac{1}{V}\sum_{\overrightarrow{p}} \overrightarrow{v}E(\overrightarrow{p})f(\overrightarrow{r},\overrightarrow{p}), \tag{1.9}$$

where V is volume of the system, $\overrightarrow{v}$ is the velocity of phonons, E the energy of phonons and $f(\overrightarrow{r},\overrightarrow{p})$ the distribution function in the $(\overrightarrow{r},\overrightarrow{p})$ space. The main problem is to determine the distribution function $f(\overrightarrow{r},\overrightarrow{p})$. In order to do so, one can use a Boltzmann equation, that describes phonons in a similar way than a classical particle gas:

$$\frac{\partial f}{\partial t} + \frac{d\overrightarrow{r}}{dt} \bullet \overrightarrow{\nabla}_{\overrightarrow{r}} f + \frac{d\overrightarrow{p}}{dt} \bullet \overrightarrow{\nabla}_{\overrightarrow{p}} f = \left(\frac{\partial f}{\partial t}\right)_{coll}, \tag{1.10}$$

where the subscripts ($\overrightarrow{r}$ and $\overrightarrow{p}$) are operators of the particle as a function of the coordinate $\overrightarrow{r}$ and momentum $\overrightarrow{p}$. $\left(\frac{\partial f}{\partial t}\right)_{coll}$ is the collision term and it is given by:

$$\left(\frac{\partial f}{\partial t}\right)_{coll} = -\frac{f - f^0}{\tau}, \tag{1.11}$$

where f^0 is the distribution function of phonons at equilibrium. It is given by Bose-Einstein statistics:

$$f^0 = \frac{1}{e^{\left(\frac{\hbar\omega}{k_B T}\right)} - 1}, \tag{1.12}$$

where k_B is the Boltzmann constant, ω is the phonon angular frequency and T is the absolute temperature. For phonons, no external force is possible, i.e., $\frac{d\overrightarrow{p}}{dt} = \overrightarrow{0}$, and using the hypothesis of stationary regime $\frac{\partial f}{\partial t} = 0$, one can use Eq. 1.12 to solve Eq. 1.10. Therefore the distribution function can be expressed as:

$$f(\overrightarrow{r},\overrightarrow{k}) = f^0 - \tau\frac{df^0}{dT}\overrightarrow{v} \bullet \overrightarrow{\nabla}T, \tag{1.13}$$

where we have replaced the dependency on momentum $\overrightarrow{p}$ by a dependency on the wave vector $\overrightarrow{k} = \overrightarrow{p}/\hbar$. Consider the temperature gradient along the x–axis, then the thermal current can be expressed as:

$$q_x = \sum_s \left[\frac{1}{V}\sum_{\kappa_{x1}=-\kappa_{max}}^{\kappa_{max}}\sum_{\kappa_{y1}=-\kappa_{max}}^{\kappa_{max}}\sum_{\kappa_{z1}=-\kappa_{max}}^{\kappa_{max}} v_x\hbar\omega f(\overrightarrow{r},\overrightarrow{k})\right], \tag{1.14}$$

where s represents the summation over all polarizations and v_x is the phonon group velocity. Transform Eq. 1.14 into an integration over frequency ω, then one can write:

$$q_x = \frac{1}{V}\sum_s \int_{\kappa_{x1=-\kappa_{max}}}^{\kappa_{max}} \int_{\kappa_{y1=-\kappa_{max}}}^{\kappa_{max}} \int_{\kappa_{z1=-\kappa_{max}}}^{\kappa_{max}} v_x \hbar\omega f dk_x dk_y dk_z/(2\pi/L)^3, \tag{1.15}$$

where $L^3 = V$ is the volume of the solid. If the Debye assumption of an isotropic medium with linear dispersion relation between the frequency and the wavevector is made i.e. $\omega = v_D k$, we find another expression over the energy and solid angle:

$$q_x = \int_0^{\omega_{max}} d\omega \left[\int_0^{2\pi} \left\{ \int_0^{\pi} v_x \cos(\theta) \hbar\omega f \frac{D(\omega)}{4\pi} \sin(\theta) d\theta \right\} d\phi \right] \tag{1.16}$$

where ω_{max} represents the highest phonon frequency and $D(\omega)$ is the density of states (DOS) for phonons per unit volume. Under the Debye approximation, DOS is given as

$$D(\omega) = \frac{3\omega^2}{2\pi^2 v_D^3}. \tag{1.17}$$

Substituting Eq. 1.13 in the Eq. 1.16, we obtain:

$$q_x = \int_0^{\omega_{max}} d\omega \left[\int_0^{2\pi} \left\{ \int_0^{\pi} \cos(\theta) \hbar\omega \left[f^0 - \tau \frac{df^0}{dT} \frac{dT}{dx} v \cos(\theta) \right] \frac{D(\omega)}{4\pi} \sin(\theta) d\theta \right\} d\phi \right] \tag{1.18}$$

$$= -\frac{1}{2} \frac{dT}{dx} \int_0^{\omega_{max}} d\omega \left\{ \int_0^{\pi} \tau v_D^2 \sin(\theta) \cos^2(\theta) \times \hbar\omega f D(\omega) \frac{df^0}{dT} d\theta \right\}. \tag{1.19}$$

Since f^0 is the equilibrium distribution, it contributes to the same amount of energy that goes from left to the right direction and vice versa. As a results, it cannot contribute to the integral. Thus, Eq. 1.19 along the x–direction can be expressed as the Fourier law

$$q_x = -\kappa \frac{dT}{dx}. \tag{1.20}$$

Therefore, by making a comparison, one can get the thermal conductivity:

$$\kappa = \frac{1}{2}\int_0^{\omega_{max}} \left\{ \tau v_D^2 C_\omega \int_0^{\pi} \sin(\theta) \times \cos^2(\theta) d\theta \right\} d\omega, \tag{1.21}$$

where $C_\omega = \hbar\omega D(\omega)\dfrac{df^0}{dT}$ is the specific heat per unit frequency. Eq. 1.21 can be integrated as:

$$\kappa = \frac{1}{3}\int \tau v_D^2 C_\omega d\omega. \tag{1.22}$$

If we assume v_D and τ are independent of frequency, therefore, Eq. 1.22 reverts to the same kinetic relation as Eq. 1.8:

$$\kappa = \frac{1}{3} C v_D \Lambda. \tag{1.23}$$

Note that Eq. (1.21) is general and no Debye assumption is required. Only isotropy has been considered.

1.2.3. Phonon mean free path

The phonon MFP is the average distance covered by a phonon between successive collisions. It is defined by $\Lambda = v\tau$, where v is the average velocity and τ is the relaxation time. Fourier's law fails to predict the thermal transport when the characteristic length of the system d is comparable to the mean free path Λ of the heat carrier of the system. Thus, determining the MFP is important to know whether the heat transfer belongs to the macroscale regime which is diffusive or to the ballistic regime. The experimental thermal properties can be used to estimate an average MFP according to the kinetic theory (see Eq. 1.8):

$$\bar{\Lambda}(T) = \frac{3\kappa(T)}{v C_V(T)}. \tag{1.24}$$

Fig. 1.2 shows the estimated average MFP of bulk silicon $\bar{\Lambda}$ as a function of temperature [8]. At low temperatures, the mean free path is large and comparable to the sample size d. In this case, the transport is confined by phonon scattering with the boundaries and as a consequence, apparent thermal conductivity of the material is reduced. In the intermediate temperature range, one can observe a very strong temperature dependence with a behavior $\dfrac{1}{\Lambda} \propto \dfrac{1}{T^4}$, which softens at large temperatures to $\bar{\Lambda} \propto \dfrac{1}{T}$.

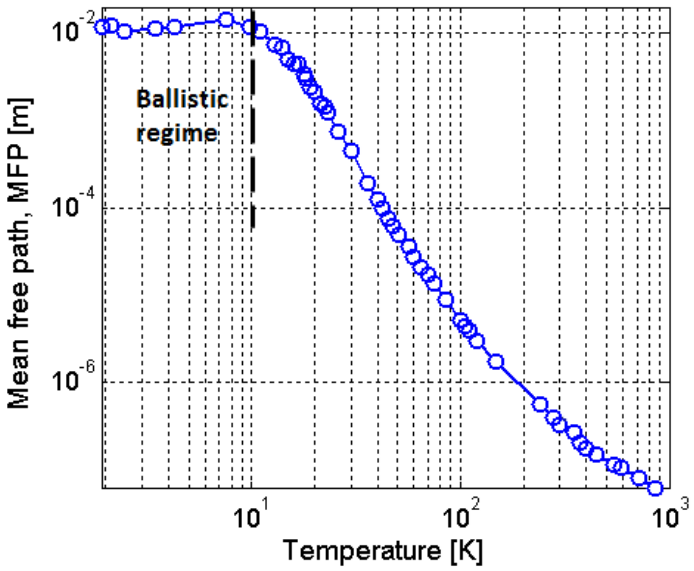

Figure 1.2. *Silicon average mean free path as a function of temperature [8].*

Peierls [9] showed two kinds of phonon–phonon scattering events: the U-processes (Umklapp processes) where the momentum is not conserved and the N-processes (Normal) where the momentum is conserved. Around room temperature, thermal conductivity is led by scattering mechanism of phonon-phonon-interaction. The U-processes are those responsible for resistance to the heat flux in bulks, while the N-processes act more indirectly [1].

1.3. Transition to ballistic regime

1.3.1. Knudsen number

Thermal transport is controlled by the distribution of the carriers mean free path, the length scale of the heat sources, the energy dispersion in the material and the size d of the material. Heat conduction can be probed in different transport regimes depending on the ratio between the MFP of phonons and the system size. The Knudsen number

$$Kn = \frac{\Lambda}{d} \tag{1.25}$$

is the key to know which regime is taking place. The transition between the transport regimes depends on the value of Kn [10, 11]. It is important to know that we can probe different ranges of Knudsen number, either by changing the characteristic geometric length d, such as a wire size, or by changing the temperature of the studied material which modifies the MFP as shown in Fig.1.2.
In the first case, where the MFP of the energy carriers is smaller than d, $Kn < 1$, Fourier's law is valid and Eq. 1.2 in the stationary regime can be written in 1D as:

$$q = -\kappa \frac{T_h - T_c}{d}. \tag{1.26}$$

The phonons will have a small deviation from their equilibrium state, a situation known as a local thermal equilibrium (LTE).

In the second case, Fourier's diffusive law will be violated and fails to predict the heat transfer phenomena, when the characteristic dimension d of a material is smaller than the average MFP of energy carriers. In this case the transfer becomes largely ballistic with $Kn > 1$. The phonons collide with the boundaries and are not scattered inside the material. They have no chance for relaxing to a near local-equilibrium state [12, 13, 14, 15] as shown in Fig. 1.3.

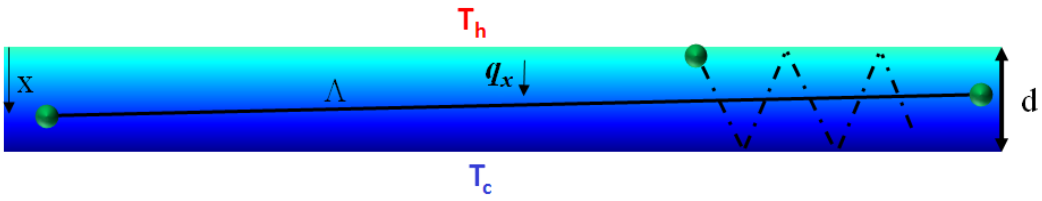

Figure 1.3. *Heat transfer between two heat sources in the ballistic regime.*

In a third case, the MFP of the energy carriers is comparable to the characteristic length d of the system, thus the transport is semi-ballistic with $Kn \approx 1$. To analyze the transport in this regime, a ballistic-diffusive approximation can be introduced to interpolate between the ballistic and diffusive transport regimes. The heat diffusion equation in 1D can be expressed following Eq. 1.26. The effective mean free path is obtained by applying a Matthiessen rule:

$$\frac{1}{\Lambda_{eff}} = \frac{1}{\Lambda} + \frac{1}{d}. \tag{1.27}$$

Hence, the ratio between the bulk κ_b and effective κ_{eff} thermal conductivity yields to the following expression:

$$\frac{\kappa_{eff}}{\kappa_b} = \frac{\Lambda_{eff}}{\Lambda_b} = \frac{1}{1+Kn}. \tag{1.28}$$

Therefore, the flux can be expressed as:

$$q = -\kappa_{eff}\frac{\Delta T}{d}, \tag{1.29}$$

where $\kappa_{eff} = \kappa_b \frac{1}{1+Kn}$ is the effective thermal conductivity that introduces the dependence on the size. The reduction of the effective thermal conductivity can be investigated when the characteristic length d of the material is moving from micron to nanometer scale. Note that a geometrical factor can appear in Eq. (1.27), which has been neglected here [16]. In reality, $\Lambda = \frac{4}{3}\bar{\Lambda}$.

1.3.2. Ballistic regime in 1D

Non–local thermal equilibrium can be achieved when the MFP of the heat carriers becomes greater than dimension d of the system. Here, ballistic regime in one dimensional system is considered. For $\Lambda >> d$

$$q = -\frac{1}{3}Cv\bar{\Lambda}\frac{\Delta T}{\frac{4}{3}\bar{\Lambda}+d} \tag{1.30}$$

$$\approx -\frac{1}{3}Cv\bar{\Lambda}\frac{\Delta T}{\frac{4}{3}\bar{\Lambda}} \tag{1.31}$$

$$\approx -\frac{1}{4}C(T)v\Delta T, \tag{1.32}$$

Eq. 1.32 demonstrates that thermal conductivity depends only on the heat capacity C and not anymore on $\bar{\Lambda}$. The maximal conductance is $G = q/\Delta T = 1/4C(T)v$ [17].
Since the velocity only weakly depends on temperature, the ballistic flux is driven by the heat capacity. We now pay attention to its behavior. Under the Debye isotropic

continuum approximation, taking into account the contribution from all phonon acoustic branches, the total energy of phonons in thermal equilibrium can be expressed as

$$U = \int_0^{\omega_D} \hbar\omega f(T,\omega) D(\omega) d\omega. \tag{1.33}$$

Insert Eq.1.17 into Eq.1.33, then

$$U = \frac{3}{2\pi^2 v_D^3} \int_0^{\omega_D} \frac{\hbar\omega^3}{e^{\frac{\hbar\omega}{k_B T}} - 1} d\omega. \tag{1.34}$$

where ω_D is the Debye frequency. At low temperature, Debye considers that the dispersion relation is linear until a limit wave vector κ_D defined by the density n, with $n = \kappa_D^3/6\pi^2$. The volumetric specific heat of phonons is obtained by deriving U with respect to temperature:

$$C_V = \frac{3\hbar^2}{2\pi^2 v_D^3 k_B T^2} \int_0^{\omega_D} \frac{\omega^4 e^{\frac{\hbar\omega}{k_B T}}}{[e^{\frac{\hbar\omega}{k_B T}} - 1]^2}. \tag{1.35}$$

The relation between the Debye velocity, frequency and temperature can be expressed as

$$\omega_D = \frac{\pi v_D}{a_D} = \frac{k_B \theta_D}{\hbar}. \tag{1.36}$$

Substituting these definitions into Eq.1.35 and introducing the dimensional quantities, $x = \dfrac{\hbar\omega}{k_B T}$ and $\omega_D = \dfrac{\theta_D}{T}$, then the specific heat can be written as

$$C_V = 9nk_B \left(\frac{T}{\theta_D}\right)^3 \int_0^{\theta_D/T} \frac{x^4 e^x dx}{(e^x - 1)^2} \tag{1.37}$$

Fig. 1.4 presents the experimental specific heat of silicon as a function of temperature.

At low temperatures, $\theta_D/T \to \infty$, then heat capacity becomes

$$C_V = \frac{36\pi^4 k_B}{15} n \left(\frac{T}{\theta_D}\right)^3 \propto T^3. \tag{1.38}$$

In the ballistic regime, the thermal conductance $G = q/\Delta T$ will therefore follow the same

behavior. At high temperatures ($T >> \theta_D, x << 1$), heat capacity becomes

$$C_V = 9nk_B \left(\frac{T}{\theta_D}\right)^3 \int_0^{\theta_D/T} x^2 dx = 3nk_B \propto T^0. \tag{1.39}$$

While the Debye model is certainly an approximation, we find that it reproduces well the behaviors observed in Fig. 1.4. Note that considering different velocities for the transverse and longitudinal polarizations would not change the main observations.

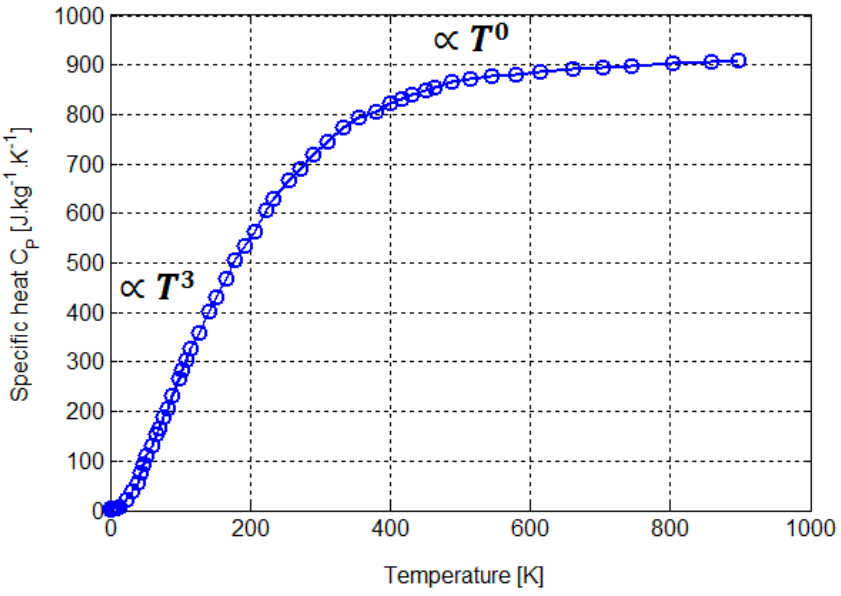

Figure 1.4. *Silicon specific heat as a function of temperature [8].*

1.4. Size effect in nanostructures on heat transfer at room and low temperatures

As the material size decreases, the ratio of the surface to the volume increases and therefore heat conduction at the interfaces and boundaries becomes extremely important. In particular, the confinement of heat in nanostructures leads to strong constriction effects [18, 19]. When the characteristic lengths of phonons are comparable or smaller than the characteristic length (size) of the material, phonons collide with the boundaries more often than in bulk material. As a consequence, the resistance to the heat flow associated to in–plane transfer in thin films and nanowires increases and therefore the

effective thermal conductivity of nanostructures [3, 20, 21, 22, 23] reduces strongly [24, 25]. Fig.1.5 shows values of the thermal conductivity as a function of temperature, based on experimental results of silicon nanowires. The thermal conductivity of bulk silicon at room temperature is 149 $\mathrm{W.m^{-1}.K^{-1}}$. Fig. 1.5 shows that the thermal conductivity is dependent on the diameter of nanowires with large reduction from the bulk value by more than two orders of magnitude.

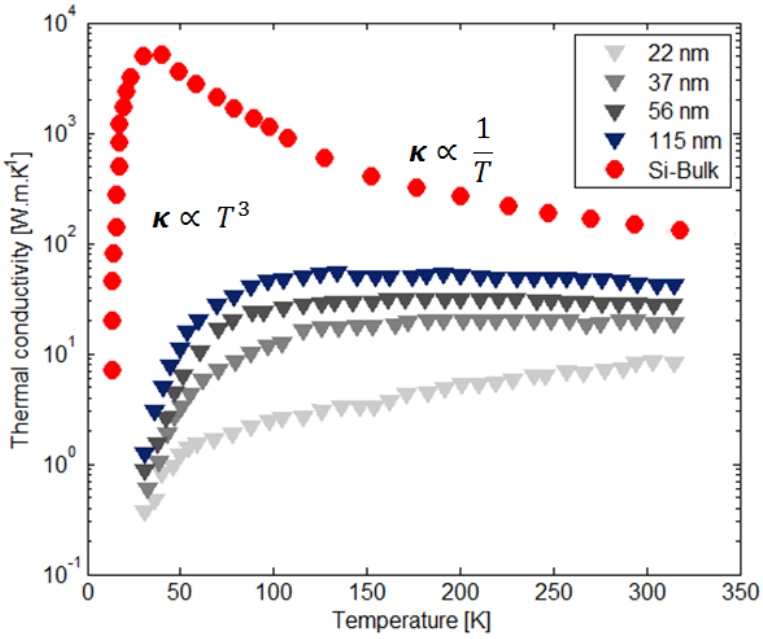

Figure 1.5. *Experimental measurement of effective thermal conductivity of single crystalline Si nanowires with different diameters [26].*

Generally, phononic transfer can be recognized by two fundamental length scales of phonon, the mean free path as explained in Sec. 1.2, and the wavelength linked to the wave behavior. Phonon wavelength can be estimated by using dominant wavelength approximation. The principle is the same as for the blackbody emission of photons that connects the photon energy E associated with its wave frequency. Phonon wavelengths span over the large range of the acoustic phonon spectrum. At given temperature T, lattice vibrations (phonons) will be emitted at an angular frequency ω related to the Bose-Einstein distribution. As a result, a Planck law for phonons can be introduced. Thus, the dominant phonon wavelength can be simply estimated $\hbar\frac{c}{\lambda} = k_B T$, where $\hbar$ is the reduced Planck constant. Fig.1.6 represents the approximate dominant phonon wavelength estimated by $\lambda_{max} = \frac{h\upsilon_s}{2.8\kappa_B T}$, where υ_s is the sound velocity and 2.8 is a

constant resulting from the derivation of Planck's law for phonons by relating the temperature and maximum frequency ω_{max}. Note that around room temperature this estimate leads to values lower than the atomic lattice, which is not possible as the lattice sets a lower limit.

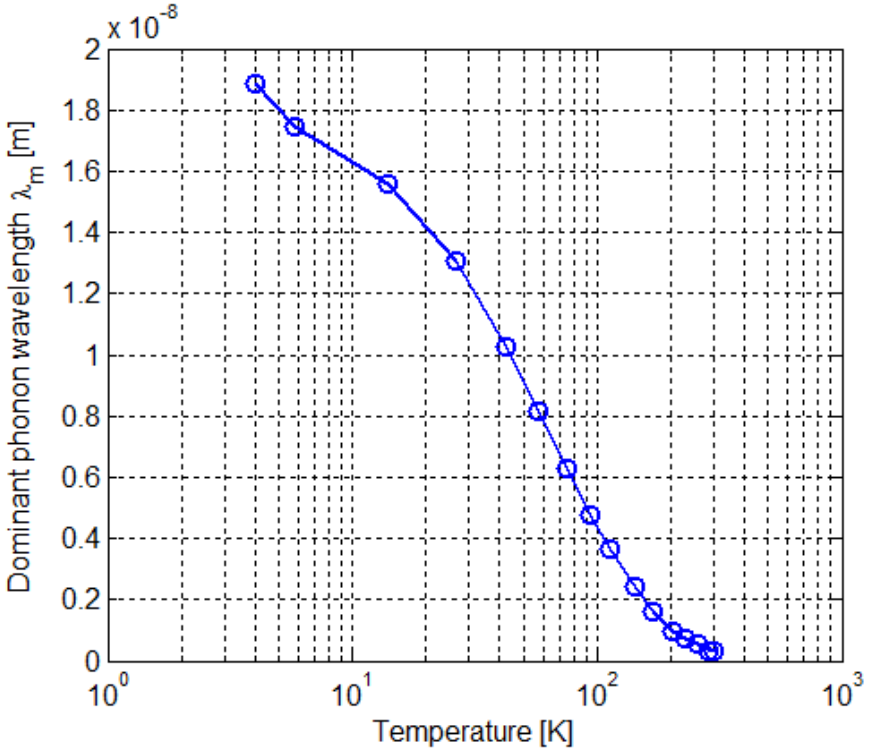

Figure 1.6. *Phonon dominant wavelength as a function of temperature [18].*

1.5. Selection of high thermal conductivity materials

Controlling the thermal conductivity of crystalline materials such as semiconductors plays an important role in microelectronics, electronic packaging, heat sinks and in designing power-dissipation devices. High thermal conductivity materials are required in thermal management for the purpose of cooling. The material that has a thermal conductivity which exceeds 100 $\mathrm{W.m^{-1}.K^{-1}}$ at room temperature can be considered to possess a high thermal conductivity [1]. Our goal will be to choose a high thermal conductivity material with a large MFP, a high electrical resistivity to prevent significant

current from flowing inside the material and low piezoelectric coefficient to avoid electro–thermal stress. Table 1.1 below shows the thermal properties of different materials. The average mean free paths are calculated from the kinetic theory (Eq. 1.24).

Material	Thermal conductivity κ $[\mathrm{Wm^{-1}K^{-1}}]$	Volumetric heat capacity $\times 10^8[\mathrm{Jm^{-3}K}]$	Sound velocity υ $[\mathrm{ms^{-1}}]$	Mean free path Λ $[\mathrm{nm}]$	References
Diamond	2000	1.82	8218	400	[27, 28]
Boron nitride	1300	2.76	7065	200	[29]
Silicon carbide (SiC)	490	2.21	1660	400	[28, 30]
Aluminum nitride (AlN)	320	1.98	1584	306 (min)	[28, 29]
Silicon (Si)	149	1.63	1370	300	[31]
Sapphire (Al_2O_3)	30-35	1.66	4190	150	[8]
Silicon dioxide (SiO_2)	12.5	1.96	8433	225	[8]

Table 1.1. *Relevant physical properties of high thermal conductivity materials and few other crystalline materials.*

1.6. Thermal boundary resistance

One of the most important aspects that needed to be considered at the nanoscale is the solid–solid interface that can control the overall transport. Here, we will illustrate the effect of the interfaces on the transport between two solid materials and analyse the effect of heat confinement due to interfacial boundary resistance issue.

Interfacial thermal resistance R_K [25, 32, 33, 34, 35, 36, 37, 38, 39] is the measure of interface's resistance to heat flow. It is defined as the ratio of the temperature drop at the interface to the power per unit area flowing across that interface and it can be expressed as

$$R_K = \frac{\Delta T}{q}, \tag{1.40}$$

where ΔT (K) is the temperature discontinuity at the interface and q is the thermal flux (W) across the interfacial region. The imperfection of the interface between two materials is due to many characteristics such as thin oxide layer, bonding, structure, geometry and irregularity. Fig. 1.7 presents the effect of the interface between two materials on the temperature profile. The effect of the boundary resistance at nanoscale can become larger due to the increase of the surface–to–volume ratio.

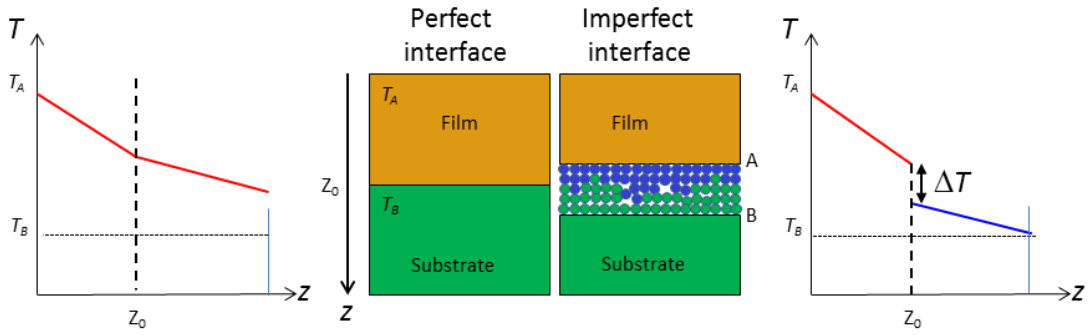

Figure 1.7. *Schematic illustration showing the effect of the perfect and imperfect interfaces on the temperature profile.*

We shall introduce the thermal boundary resistance (TBR), also called Kapitza resistance due to the phonon scattering at interface. The interface can be imagined as the plane in–between two different materials. The temperature drop is due to the mismatch in phonon velocity and density of the two materials. Imposing a temperature difference at the two sides of the interface will create a non equilibrium state of phonons. Imagine an emitted phonon coming toward the interface at a temperature T_A, the transmitted and the reflected phonons may have a different spectral distribution. The phonon heat flux that is transmitted from material A to B can be described as [32] (see the similarity with Eq. 1.14)

$$q_{A\to B} = \sum_s \left[\frac{1}{V_A} \sum_{\kappa_x=-\kappa_{max}}^{\kappa_{max}} \sum_{\kappa_y=-\kappa_{max}}^{\kappa_{max}} \sum_{\kappa_z=0}^{\kappa_{max}} v_{zA} \hbar\omega \alpha_{AB} f(\omega, T_A) \right], \tag{1.41}$$

where v_{zA} is the phonon velocity along z–direction of material A, $\hbar$ is the reduced Planck constant, T_A represents the temperature of phonons coming toward the interface, α_{AB} is the phonon transmissivity from medium A into medium B and $f(\omega, T_A)$ is the

Bose–Einstein distribution for phonons at T_A. The summations are over all the wave vectors of κ_x, κ_y and positive wave vector of κ_z. The division by the volume allows to obtain the flux per unit surface. The summation over s denotes that over the phonon polarizations. Transform Eq. 1.41 into an integration over all the wavevectors k, then one can write:

$$q_{A\to B} = \iint\limits_{\Omega_A>2\pi} \left[\int_0^{\omega_{D_A}} v_{zA}\hbar\omega\alpha_{AB} f(\omega,T_A)\frac{D_A(\omega)}{4\pi}d\omega \right] d\Omega_A \tag{1.42}$$

$$= \frac{1}{4\pi}\int_0^{2\pi} d\phi_A \int_0^{\pi/2} \theta_{\mathrm{A}} d\theta_A \left[\int_0^{\omega_{D_A}} v_A\cos(\theta_A)\alpha_{AB}(\omega,\theta_A,\phi_A)\hbar\omega\alpha_{AB} f(\omega,T_A)\frac{D_A(\omega)}{4\pi}d\omega \right] \tag{1.43}$$

where $\Omega_A > 2\pi$ is the half–space solid angle towards the interface from medium A, $d\Omega = \sin(\theta)d\theta d\phi$ and ω_{D_A} is the Debye frequency of medium A. An expression similar to Eq. 1.43 can be found for the heat flux from material B to A. The net heat flux is the difference of the two and can be expressed as

$$q = \iint\limits_{\Omega_A\geqslant 2\pi} \left[\int v_A\cos(\theta_A)\hbar\omega f(\omega,T_A)\alpha_{AB}(\omega,\theta_A,\phi_A)\frac{D_A(\omega)}{4\pi}d\omega \right] d\Omega_A \tag{1.44}$$

$$- \iint\limits_{\Omega_B\leqslant 2\pi} \left[\int v_B\cos(\theta_B)\hbar\omega f(\omega,T_B)\alpha_{BA}(\omega,\phi_B,\theta_B)\frac{D_B(\omega)}{4\pi}d\omega \right] d\Omega_B. \tag{1.45}$$

At thermal equilibrium when $T_A = T_B$, the net heat flux is zero. Then $\int_{\Omega_A\geqslant 2\pi}\left[\int v_A\cos(\theta_A)\hbar\omega f(\omega,T_A)\alpha_{AB}(\omega,\theta_A,\phi_A)\frac{D_A(\omega)}{4\pi}d\omega \right] d\Omega_A$. Thus Eq. 1.43 can be written as

$$q = \int_{\Omega_A\geqslant 2\pi}\left[\int v_A\cos(\theta_A)\hbar\omega\left[f(\omega,T_A) - f(\omega,T_B)\right]\alpha_{AB}(\omega,\theta_A,\phi_A)\frac{D_A(\omega)}{4\pi}d\omega \right] d\Omega_A. \tag{1.46}$$

$h_K = \dfrac{1}{R_K}$ is the thermal boundary conductance. For $\Delta T \to 0$, thermal conductance is given by the derivative of the flux with respect to temperature, i.e.

$$h_K = \frac{dq}{dT} = \int_{\Omega_A\geqslant 2\pi}\left[\int v_A\cos(\theta_A)\hbar\omega\left[\frac{df(\omega,T)}{dT}\right]\alpha_{AB}(\omega,\theta_A,\phi_A)\frac{D_A(\omega)}{4\pi}d\omega \right] d\Omega_A. \tag{1.47}$$

The key information related to the boundary conductance is encoded in the transmission coefficient $\alpha_{AB}(\theta,\phi)$. The study of the interfacial resistance depends on the atomic

structure of each material at the interface. If both sides are made of the same material, the construction at interface leads to perfect contact so that the transmission coefficient from A to B will be the same from B to A. In the case where we have different materials, the atomic disorders at interface creates a bad contact and can lead to constrictions of the heat flux lines. The thermal contact at the interface will never be perfect since some roughness is often present [40]. While we do not try to estimate the α_{AB} in this work, we will need to consider thermal interfaces effect at the macroscopic scale. The Diffuse Mismatch Model (DMM) [32] allows to provide a first estimate of the TBR in the case of dissimilar materials. Under many approximations, the transmittivity α_{AB} can be written:

$$\alpha_{AB} = \frac{4Z_A Z_B}{(Z_A Z_B)^2}, \tag{1.48}$$

where Z is the acoustic impedance. All this section is related to phonon transmission at interfaces. When a metal is involved, electron-phonon coupling is also involved. Such effects will not be discussed in this thesis and should deserve further investigation in the future.

1.7. Some consequences and applications of heat conduction in nanowires

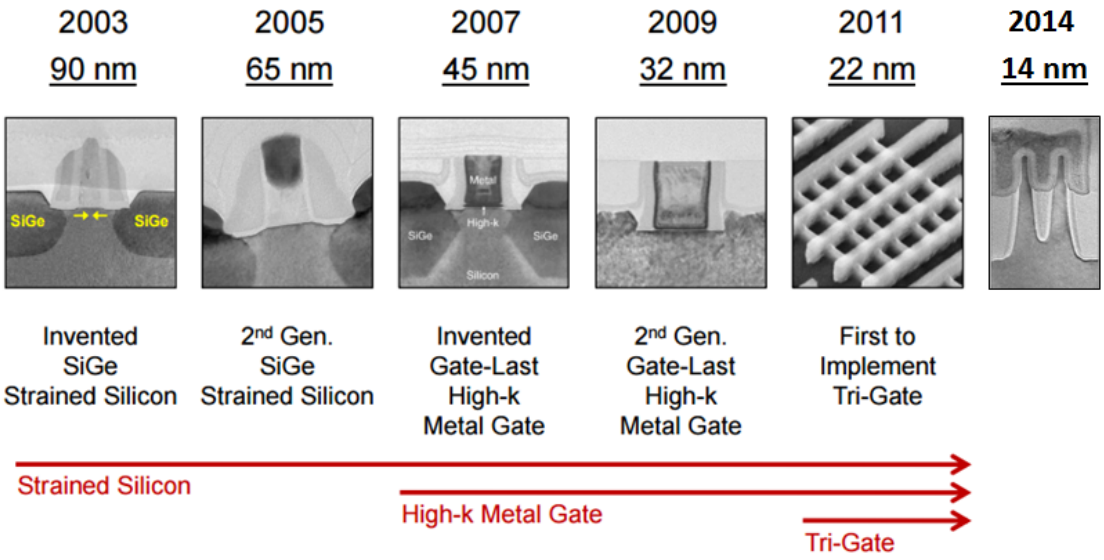

Figure 1.8. *14 and 22 nm high performance and low-power CMOS technology featuring fully-depleted tri-gate transistors [41].*

Thermal management becomes critical in many modern technological applications such as thermoelectrics, nanoelectronics and nanophononics. The main interest of heat transfer at nanoscale is to increase the efficiency and get a power reduction at constant performance. Moreover, there is also a need to increase the focus on how to utilize the new physics offered at the nanoscale to increase device functionality.

Thermal management in electronic circuits is becoming an integral part of design [42]. Thermal generation rate $\rho(T)\frac{I^2}{\lambda S}$ increases with temperature, where $\rho(T) = \rho_0(1 + \alpha\Delta T)$ and S is a wire cross section. As the performance of ultralarge scale integrated (ULSI) circuits depends on temperature, even a small increase of temperature results in reduction of the device lifetime, for instance every increase of 10 K in operating temperature cuts product lifetimes in half [43]. Overheating in the computer industry is a big problem for the roomfuls of servers in data storage and leads to cease operation of the processors and then damaging it.

Thus, finding a material with a high thermal conductivity, which can be integrated with Si complementary metal–oxide semiconductors (CMOS), may allow for solving the thermal problem.

In addition, the electromigration (EM) which is the electrical current–induced diffusion of atoms in the metallic nanowire can lead to failure. Black's law allows to study the effect of the current density on the nanowire lifetime and to determine interconnect reliability. The median time to failure is $MTF = Aj^{-2}e^{\frac{E_a}{\kappa T}}$, known as the Black equation, where A is a sample dependent constant, j the current density and E_a an activation energy for atomic motion [44]. It can be noticed that electromigration failure depends on the inverse square of the current density. In nanowires, the current and temperature are both changing rapidly, while the current densities in metallic nanowires are at least two orders of magnitude than in the bulk wires. The law shows that the electromigration time decreases with temperature.

Another challenge at the nanoscale is the thermal flow across the boundary and the impact of TBR [45]. As the heater width becomes narrower then interfacial boundary resistance blocks heat through the wire for being dissipated by the substrate. Consequently the temperature rises through the wire and becomes higher. However, at high temperatures, nanowires tend to expand due to the thermal expansion. Thus, the change in size over a small length scales different from the real one cracks the wire.

Many technological applications rely on thin wires, such as trigate transistors for the information technologies [46, 47]. Nanowire width is key to determine the heat dissipation: as the heater width becomes narrower, the temperature rises. As a result, the efficiency decreases while the thermal conductivity can be reduced due to the interface scattering. For instance, the confinement of heat in 22 and 14 nm node and trigate transistor concept [41, 48] (see Fig. 1.8) can lead to strong constriction effects.

Semiconductor Nanowire is a configuration that can be used for several applications. For instance, logic gates [49] (see Fig. 1.9) have been used to implement basic computation. Semiconductor nanowires can be used as building blocks for assembling a range of nanodevices including FETs, p-n diodes and bipolar junction. This nanowire junction array have been configured as key OR, AND, and NOR logic–gate.

Figure 1.9. *Multiple junction [49].*

In addition, energy conversion devices can benefit from nanoscale energy transport. The reduction of thermal conductivity can be exploited to enhance the thermoelectricity figure of merit

$$ZT = \frac{S^2\sigma}{K}T \tag{1.49}$$

where S is the Seebeck coefficient, σ is the electrical conductivity in $\mathrm{S.m^{-1}}$ and $k = \kappa_p + \kappa_e$ is the total thermal conductivity which has contributions from electron and phonon thermal conductivity respectively. Thermoelectric materials involves the conversion from thermal to electric energy [50] or the reverse as well as it can be useful for heat and cooling systems. Materials with a large thermoelectric figure of merit can be used to develop efficient solid-state devices that convert waste heat into electricity. Up to now, suspended nanowires have been considered [3, 20, 51, 52] but construction effect could be useful for blocking heat in the future.

1.8. Summary

Thermal transport at the nanoscale is different from that at the macroscale. When the material shrinks from bulk to nanoscale size, the distribution of the heat carriers becomes different. Based on the characteristic lengths of the heat carriers and on the device sizes, different transport regimes can be detected. Phonon–boundary scattering at nanoscale can impact and significantly change the thermal transport from the bulk counterpart and this leads to a large reduction of the thermal conductivity. We have seen that interfacial boundary resistance can influence the temperature rise at interface of two materials. Controlling the thermal properties and understanding the thermal transport at the nanoscale is promising for technological applications in various fields. Thermal transport regime can be investigated, either by changing the characteristic length of the material or by selecting the mean free path of the heat carriers by controlling temperatures. We will see in the following how we have tackled such issue, especially in two–dimensional and tri–dimensional heat dissipation from their wires.

References

[1] G. P. Srivastava, *The physics of phonons*, (1990).

[2] C. Dames, B. Poudel, W. Wang, J. Huang, Z. Ren, Y. Sun, J. Oh, C. Opeil, M. Naughton and G. Chen, *Low-dimensional phonon specific heat of titanium dioxide nanotubes*, Applied Physics Letters **87**, 031901 (2005).

[3] D. Li, Y. Wu, P. Kim, L. Shi, P. Yang and A. Majumdar, *Thermal conductivity of individual silicon nanowires*, Applied Physics Letters **83**, 2934 (2003).

[4] P. Klemens, *Proceedings of the Royal Society of London A: Mathematical, Physical and Engineering Sciences*, **208**, 108 (1951).

[5] J. Callaway, *Model for lattice thermal conductivity at low temperatures*, Physical Review **113**, 1046 (1959).

[6] A. H. Nayfeh, *Wave propagation in layered anisotropic media: With application to composites*, (1995).

[7] C. Glassbrenner and G. A. Slack, *Thermal conductivity of silicon and germanium from 3 K to the melting point*, Physical Review **134**, A1058 (1964).

[8] Y. S. Touloukian, *Thermophysical Properties of High Temperature Solid Materials. Volume 4. Oxides and Their Solutions and Mixtures. Part I. Simple Oxygen Compounds and Their Mixtures*, (1966).

[9] R. Peierls, *Zur kinetischen theorie der wärmeleitung in kristallen*, Annalen der Physik **395**, 1055 (1929).

[10] G. Chen, *Ballistic-diffusive heat-conduction equations*, Physical Review Letters **86**, 2297 (2001).

[11] R. Yang, G. Chen, M. Laroche and Y. Taur, *Simulation of nanoscale multidimensional transient heat conduction problems using ballistic-diffusive equations and phonon Boltzmann equation*, Journal of Heat Transfer **127**, 298 (2005).

[12] R. Wilson and D. G. Cahill, *Anisotropic failure of Fourier theory in time-domain thermoreflectance experiments*, Nature communications **5**, (2014).

[13] Y. Hu, L. Zeng, A. J. Minnich, M. S. Dresselhaus and G. Chen, *Spectral mapping of thermal conductivity through nanoscale ballistic transport*, Nature nanotechnology **10**, 701 (2015).

[14] P.-O. Chapuis, Y. Wang and N. Djati, *Congrès Français de Thermique 2014*, 8 (2014).

[15] J.-J. Freffet and S. Volz, *Transferts de chaleur à l'échelle du nanomètre*, (2007).

[16] A. Majumdar, J. Carrejo and J. Lai, *Thermal imaging using the atomic force microscope*, Applied Physics Letters **62**, 2501 (1993).

[17] A. Majumdar, *Microscale heat conduction in dielectric thin films*, Journal of Heat Transfer **115**, 7 (1993).

[18] P.-O. Chapuis, M. Prunnila, A. Shchepetov, L. Schneider, S. Laakso, J. Ahopelto and C. Sotomayor Torres, *Thermal Investigations of ICs and Systems (THERMINIC), 2010 16th International Workshop*, 1 (2010).

[19] M. Bartkowiak and G. Mahan, *Heat and electricity transport through interfaces*, Semiconductors and Semimetals **70**, 245 (2001).

[20] A. I. Hochbaum, R. Chen, R. D. Delgado, W. Liang, E. C. Garnett, M. Najarian, A. Majumdar and P. Yang, *Enhanced thermoelectric performance of rough silicon nanowires*, Nature **451**, 163 (2008).

[21] J.-S. Heron, C. Bera, T. Fournier, N. Mingo and O. Bourgeois, *Blocking phonons via nanoscale geometrical design*, Physical Review B **82**, 155458 (2010).

[22] A. I. Boukai, Y. Bunimovich, J. Tahir-Kheli, J.-K. Yu, W. A. Goddard Iii and J. R. Heath, *Silicon nanowires as efficient thermoelectric materials*, Nature **451**, 168 (2008).

[23] J. Lim, K. Hippalgaonkar, S. C. Andrews, A. Majumdar and P. Yang, *Quantifying surface roughness effects on phonon transport in silicon nanowires*, Nano Letters **12**, 2475 (2012).

[24] D. G. Cahill, W. K. Ford, K. E. Goodson, G. D. Mahan, A. Majumdar, H. J. Maris, R. Merlin and S. R. Phillpot, *Nanoscale thermal transport*, Journal of Applied Physics **93**, 793 (2003).

[25] K. Termentzidis, J. Parasuraman, C. A. Da Cruz, S. Merabia, D. Angelescu, F. Marty, T. Bourouina, X. Kleber, P. Chantrenne and P. Basset, *Thermal conductivity and thermal boundary resistance of nanostructures*, Nanoscale Research Letters **6**, 1 (2011).

[26] D. Li, S. T. Huxtable, A. R. Abramson and A. Majumdar, *Thermal transport in nanostructured solid-state cooling devices*, Journal of Heat Transfer **127**, 108 (2005).

[27] Z. Cao and D. Aslam, *Fabrication technology for single-material MEMS using polycrystalline diamond*, Diamond and Related Materials **19**, 1263 (2010).

[28] D. Chung, *Materials for thermal conduction*, Applied Thermal Engineering **21**, 1593 (2001).

[29] K. Shimada, T. Sota and K. Suzuki, *First-principles study on electronic and elastic properties of BN, AlN, and GaN*, Journal of Applied Physics **84**, 4951 (1998).

[30] Y. Goldberg, M. Levinshtein and S. Rumyantsev, *Silicon carbide (SiC)*, Properties of Advanced Semiconductor Materials: GaN, AIN, InN, BN, SiC, SiGe 93 (2001).

[31] Y. Ju and K. Goodson, *Phonon scattering in silicon films with thickness of order 100 nm*, Applied Physics Letters **74**, 3005 (1999).

[32] E. T. Swartz and R. O. Pohl, *Thermal boundary resistance*, Reviews of Modern Physics **61**, 605 (1989).

[33] O. Käding, H. Skurk and K. Goodson, *Thermal conduction in metallized silicon-dioxide layers on silicon*, Applied Physics Letters **65**, 1629 (1994).

[34] K. Goodson, O. Käding, M. Rösler and R. Zachai, *Experimental investigation of thermal conduction normal to diamond-silicon boundaries*, Journal of Applied Physics **77**, 1385 (1995).

[35] A. N. Smith, J. L. Hostetler and P. M. Norris, *Thermal boundary resistance measurements using a transient thermoreflectance technique*, Microscale Thermophysical Engineering **4**, 51 (2000).

[36] D. G. Cahill, K. Goodson and A. Majumdar, *Thermometry and thermal transport in micro/nanoscale solid-state devices and structures*, Journal of Heat Transfer **124**, 223 (2002).

[37] R. J. Stevens, A. N. Smith and P. M. Norris, *Measurement of thermal boundary conductance of a series of metal-dielectric interfaces by the transient thermoreflectance technique*, Journal of Heat Transfer **127**, 315 (2005).

[38] C. Cardenas, D. Fabris, S. Tokairin, F. Madriz and C. Y. Yang, *Thermoreflectance measurement of temperature and thermal resistance of thin film gold*, Journal of Heat Transfer **134**, 111401 (2012).

[39] P. E. Hopkins, *Thermal transport across solid interfaces with nanoscale imperfections: effects of roughness, disorder, dislocations, and bonding on thermal boundary conductance*, ISRN Mechanical Engineering **2013**, (2013).

[40] J. H. Lienhard, *A heat transfer textbook*, (2013).

[41] M. Bohr and K. Mistry, *Intels revolutionary 22 nm transistor technology*, Intel website (2011).

[42] A. Vassighi and M. Sachdev, *Thermal and power management of integrated circuits*, (2006).

[43] P. Q. Initiative and T. Edition, *Led luminaire lifetime: Recommendations for testing and reporting*, (2014).

[44] J. R. Lloyd, *Electromigration for designers: An introduction for the non-specialist*, IBM TJ Watson Research Center 1 (2002).

[45] P. Zolotavin, A. Alabastri, P. Nordlander and D. Natelson, *Plasmonic Heating in Au Nanowires at Low Temperatures: The Role of Thermal Boundary Resistance*, ACS nano **10**, 6972 (2016).

[46] B. Doyle, S. Datta, M. Doczy, S. Hareland, B. Jin, J. Kavalieros, T. Linton, A. Murthy, R. Rios and R. Chau, *High performance fully-depleted tri-gate CMOS transistors*, Electron Device Letters, IEEE **24**, 263 (2003).

[47] R. Rios, A. Cappellani, M. Armstrong, A. Budrevich, H. Gomez, R. Pai, N. Rahhal-Orabi and K. Kuhn, *Comparison of junctionless and conventional trigate transistors with down to 26 nm*, Electron Device Letters, IEEE **32**, 1170 (2011).

[48] C. Auth, C. Allen, A. Blattner, D. Bergstrom, M. Brazier, M. Bost, M. Buehler, V. Chikarmane, T. Ghani, T. Glassman *et al.*, *VLSI Technology (VLSIT), 2012 Symposium on*, 131 (2012).

[49] Y. Huang, X. Duan, Y. Cui, L. J. Lauhon, K.-H. Kim and C. M. Lieber, *Logic gates and computation from assembled nanowire building blocks*, Science **294**, 1313 (2001).

[50] M. S. Dresselhaus, G. Chen, M. Y. Tang, R. Yang, H. Lee, D. Wang, Z. Ren, J.-P. Fleurial and P. Gogna, *New Directions for Low-Dimensional Thermoelectric Materials*, Advanced Materials **19**, 1043 (2007).

[51] R. Chen, A. I. Hochbaum, P. Murphy, J. Moore, P. Yang and A. Majumdar, *Thermal conductance of thin silicon nanowires*, Physical Review Letters **101**, 105501 (2008).

[52] K. Hippalgaonkar, B. Huang, R. Chen, K. Sawyer, P. Ercius and A. Majumdar, *Fabrication of microdevices with integrated nanowires for investigating low-dimensional phonon transport*, Nano Letters **10**, 4341 (2010).

CHAPTER 2

Experimental techniques for thermal transport in low–dimensional systems

2.1. Introduction

There are a broad variety of experimental techniques that have been developed to measure the fundamental thermal properties of materials. Achieving a high spatial resolution comparable to phonon MFPs and obtaining a high accuracy in temperature measurements requires to face different challenges. In addition, measuring high–thermal conductivity materials at the nanoscale [1] or measuring thermal properties of interfaces [2, 3, 4] can be different. Temperature measurements at length and time scales comparable to the mean free path and relaxation times of the energy carriers in materials has been a topic of considerable interest. Various techniques allow measuring the thermal properties of materials ranging from bulk to thin-film sizes. This chapter provides a review of optical and electrical techniques for the study of thermal transport in low–dimensional systems. It is divided into three sections. Importance of the experimental techniques for thermal transport in low–dimensional system is introduced in the first section. In the second section, we provide an overview on different nanoscale thermometry techniques versus demands. A short review on different optical and electrical techniques

to measure the thermal properties of the materials will be introduced. It shows that electrical methods are useful for the determination of the thermal properties, particularly at nanoscale. In the third section, it is demonstrated that the thermal properties can be determined based on four-probe electrical technique. Thermal conductivity of materials is measured in dc and ac regimes based with the so–called 3ω method. Thermal conductance measurement of the material by a four probe device was investigated. A small comparison between optical and non optical techniques is introduced in Section 2.4.

2.2. Nanoscale thermometry techniques

This section provides an overview of thermometry techniques applicable for investigating thermal transport in low–dimensional structures. It is composed of two parts. The first discusses different experimental optical techniques while in the second part electrical methods are presented. All these techniques are usually based on the determination of local temperature after excitation by providing a certain amount of heat to the system. This gives the possibility to determine the conductance, and to trace back the parameter to be determined such as the thermal conductivity with the help of some model.

2.2.1. Optical techniques

1. *Pump–probe method*

   The sample is heated through a pump laser that creates a transient temperature field in the sample. Another time–delayed probe beam is used to detect the changes in the reflectivity of the heated sample. If the sample is not reflective, a thin metallic film of tens of nanometers with a high reflectance is deposited on top of the sample and serves as the transducer [5, 6]. The changes in the surface temperature of the sample can be obtained from the change of the surface reflectivity. The small changes in the probe intensity induced by the pump is recorded by a photodiode and a lock–in amplifier (LIA).

   Several transient methods such as time domain thermoreflectance (TDTR), thermal conductivity spectroscopy technique and transient thermoreflectance (TTR) allow measuring the thermophysical properties of the samples.

A transient method used to measure the thermal conductivity of materials and electron-phonon coupling is the time domain thermo-reflectance (TDTR) [7, 8, 9]. A schematic of TDTR experimental setup is shown in Fig. 2.1.

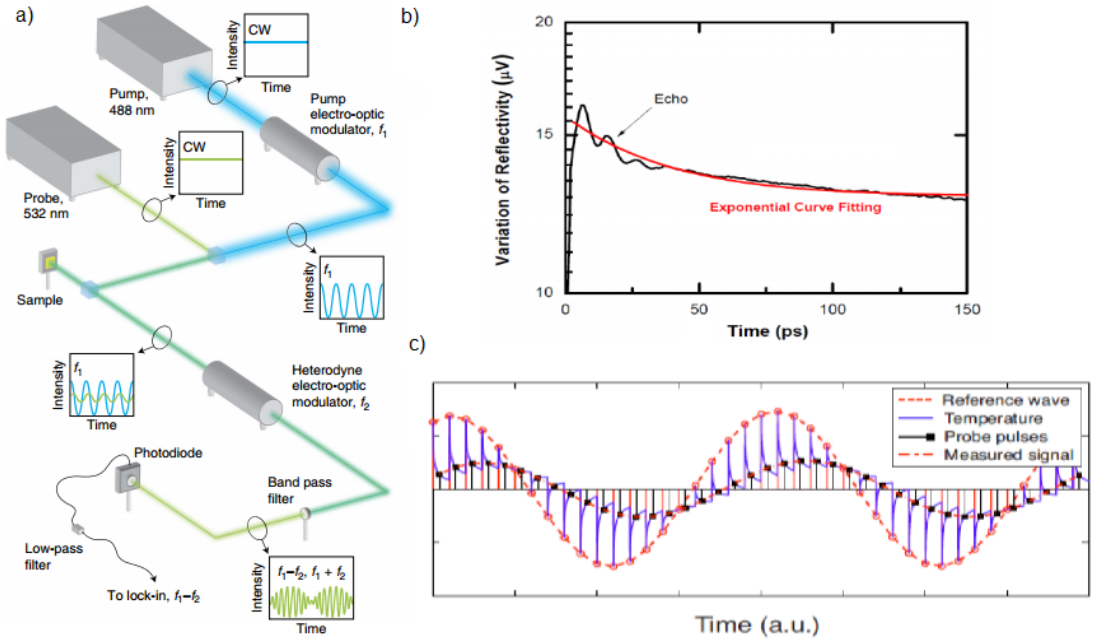

Figure 2.1. *(a) Broadband frequency domain thermo–reflectance (BB-FDTR) technique [10], (b) variation of reflectivity, (c) pump-probe pulses.*

A pump beam (448 nm) modulated by an electro-optic modulator at low frequency f_1 heats the transducer. The surface temperature of the sample is compared from the change in reflectance of the surface which is small compared to the temperature of the sample. A probed beam of 532 nm modulated by an electro-optic modulator at high frequency f_2 is used to detect the changes in the reflectivity of the material 2.1(c). The small changes in the probe intensity induced by the pump are measured by a photodiode 2.1(b) and a LIA that gives the in-phase and out-of-phase voltage at frequency f.

Thermal conductivity spectroscopy [6, 11, 12] is a transient method used to measure phonon MFPs distribution over a wide range of scales and materials. Fig. 2.2 presents experimental measurements of thermal conductivity accumulation distribution and first principle calculations of silicon versus MFP. As shown, the technique is based on varying the pump beam diameter D and observing the

change in thermal conductivity. This technique has been extended to measure the accumulation of mean free path.

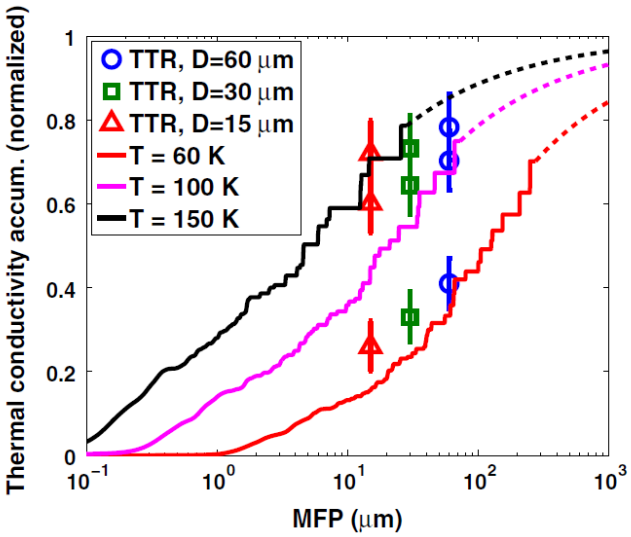

Figure 2.2. *Thermal conductivity accumulation distribution obtained by experimental measurements (symbols) and first principles calculations (lines) of natural silicon versus MFP [13].*

Transient thermoreflectance technique (TTR) is another transient method and has been also used for measurements of thermal conductivity accumulation λ_{accum} of thin films ranging in depth from microns down to hundreds of nanometers.

Table 2.1 summarizes the properties of different very–close transient techniques that are used to investigate the thermal properties of materials.

Techniques	Spatial resolution	Setup	Modulation frequency	Probed volume	Length scale	References
TDTR	10–50 μm	Optical: pump-probe	10^5 – 10^8 Hz	Given by the penetration depth: $\sqrt{\frac{D}{\omega}}$	Spot size limited by diffraction limit of light	[14, 15, 16, 17]
TTR	∽ μm	Optical: pump-probe	ns heat pulses	Given by the penetration depth: $\sqrt{\frac{D}{\omega}}$	Spot size limited by diffraction limit of light	[13, 3]
Thermal conductivity spectroscopy	∽ μm	Optical: pump-probe	1 - 12 MHz	∽ 500 nm	Spot size limited by diffraction limit of light	[13, 18, 19]

Table 2.1. *Specifications of different transient techniques.*

2. *Infrared (IR) thermometry*

Infrared thermometry technique utilizes the fact that electromagnetic radiation emitted from a solid body can be correlated to temperature. The technique consists of three elements: the emitting source, the propagation medium and the measuring device [20]. A solid emits energy in the form of thermal radiation due to its temperature. Infrared thermometer such as infrared (IR) camera of high resolution in pixels is used to characterize the temperature profile. The quantity of thermal radiation increases by rising the temperature of the sample. Quantitative temperature profiles of the solid can be determined. Heating the sample can be performed by many methods (hot plate, Joule heating, etc. - see next section for laser excitation). The main advantages of this technique are the speed and the ability to measure in high temperature range. This technique can be affected by some factors for instance the ambient radiation is hotter than the target or by dust, vapor, and particles in the atmosphere and high operating temperature.

3. *Photothermal spectroscopy*

Photothermal spectroscopy (PTS) [21] is a group of high–sensitivity spectroscopy methods used to measure optical absorption and thermal characterization of a given sample. The basis of photothermal spectroscopy is a photo–induced change in thermal state of the sample resulting from the absorption of radiation. Light is absorbed and not lost by emission results in heating. The heat raises the temperature thereby influencing the thermodynamic properties of the sample or of a suitable material adjacent to it. Measurement of the temperature, pressure, or density changes that occur due to optical absorption are ultimately the basis for the photothermal spectroscopic measurements.

4. *Raman thermometry*

The phenomenon of inelastic scattering of light by matter can be used to determine temperature. Raman spectroscopy uses monochromatic light, usually from a laser source applied to the intended sample [20, 22, 23]. Photons from the incident probe light source is either absorbed or passed through the sample unchanged, but a small fraction is elastically scattered with the same frequency as the incident light, i.e. elastic Rayleigh scattering, and an even smaller fraction is scattered inelastically due to interaction between the photons from the incident probe and the optical phonon modes of the sample. The Raman fraction is scattered with either lower

or higher frequency than that of the incident light. Lower frequencies are called Stokes scattering and higher frequencies are called Anti Stokes scattering. The Raman spectrum is presented in Fig. 2.3 (a). Raman thermometry is a contactless technique for thermal conductivity determination based on the probe of the local temperature due to different physical mechanism. Any aspect of the vibrational modes that changes with temperature can be used to probe the thermal state of the system. These changes are reflected in the peak position and linewidth (full width at half maximum, or FWHM) and intensity of a Raman signal, all of which vary with temperature, as is shown in Fig. 2.3 (b). Raman thermometry can be performed by using one of three different aspects of spectrum.

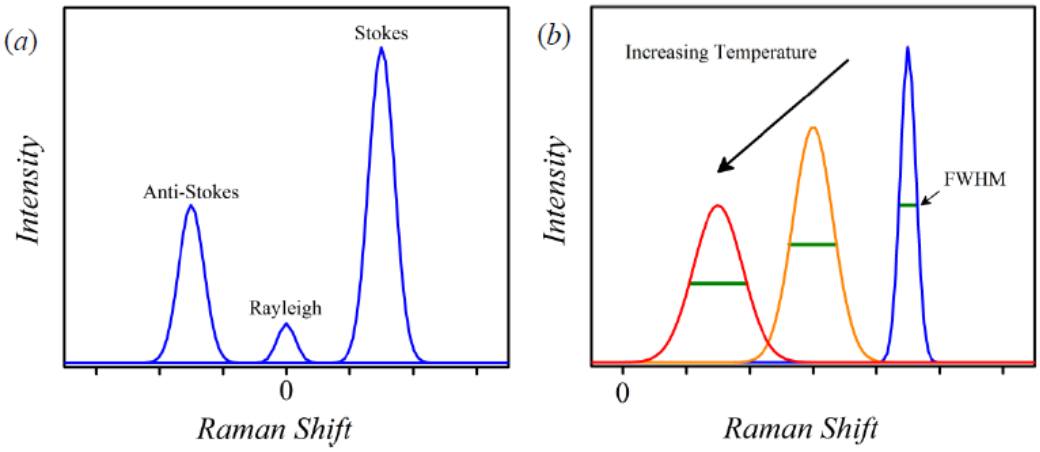

Figure 2.3. *Schematic of the Raman spectra as thermometer: (a) typical Raman spectrum showing the anti-Stokes, Rayleigh, and Stokes signal, (b) Peak position shifts and broadening of the linewidth due to temperature increasing [23].*

5. *Transient Thermal Grating*

Transient Thermal Grating (TTG) at the surfaces of absorbing materials is a contactless technique. It has been used to measure thin film thickness and for investigating heat diffusion in bulk materials [24, 25, 26]. In this method, two short laser pulses of central optical wavelength λ_{opt} are crossed in a sample resulting in an interference pattern with period $L = \lambda_{opt}/2\sin(\theta/2)$ defined by angle θ between the beams (see Fig. 2.4).

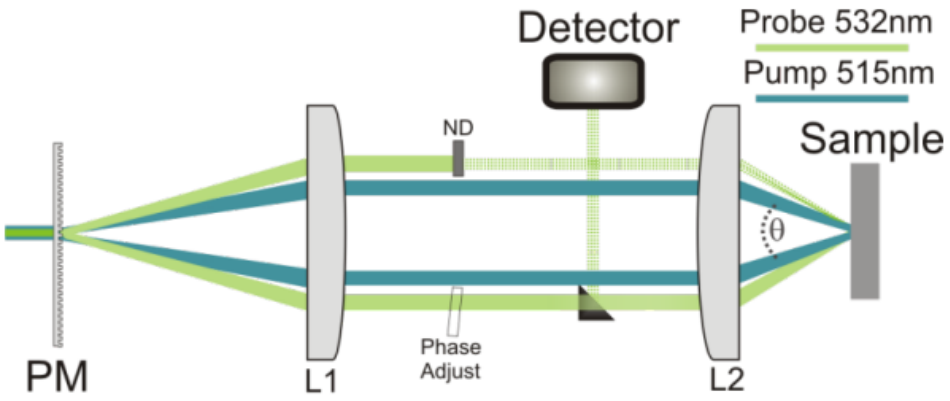

Figure 2.4. *Schematic illustration of transient thermal grating experiment in reflection geometry [26].*

The two interfering laser pulses give rise to spatially periodic heating, leading to a corresponding periodic expansion or a change in the refractive index. The relaxation of such grating is monitored by a probing laser beam and provides information about the heat diffusion. The advantages of this technique is the ability to impart length scale for thermal transport, which can be varied in the range 0.5 – 100 μm.

6. *Ultrafast coherent x-ray*

Ultrafat X-rays are femtosecond X-ray pulses with wavelengths occurring at interatomic distances. They can be used in a pumb–probe configuration. Coherent extreme ultraviolet (EUV) light detection allows probing ultrathin films with a wide range of mechanical properties and thicknesses well under 100 nm [27, 28]. In the experiment performed in [29], metallic nanowires are heated by a 25 fs pump pulse centered at a wavelength of 800 nm. Short-wavelength acoustic waves are generated through laser excitation of a nanopatterned metallic nanostructures creating an array of nanoscale hot spots (lines) on the surface of the substrate (see Fig. 2.5). The use of nanopatterned structures rather than direct optical absorption allows to explore the dissipation of heat sources much smaller than the diffraction limit of visible light. This wavelength and interferometric diffraction measurement give high lateral and axial spatial resolution to follow the dynamics in nanostructured systems with sensitivity to surface displacements at the picosecond scale. Then short wavelengths are probed by diffracting coherent EUV beams from the

dynamic surface deformation. The time delay between the EUV probe pulse and the laser pump pulse is adjusted by a mechanical delay stage between 400 and 8000 ps, with step size as small as 1 ps. As the EUV light diffracts from the periodic array of the nanowires, expansion and cooling of the nanograting change the diffraction efficiency, and this signal is recorded by a CCD camera as a function of delay time between pump and probe pulses. The change in the diffraction signal can be uniquely attributed to physical deformations in the surface profile. Moreover, because the thermally expanded nanowires will change the diffraction signal as long as their temperature is higher than their initial state, this serves as a measure of the cooling rate of the nanowires rather than the rate of heat transfer across a specific distance as in optical transient grating. This technique is parallel to the one developed in this thesis. These studies also use nanowires on top of silicon substrate, but the measurements are performed optically [29] while our measurements are performed electrically (see Chapter 6). However, this technique requires special facility and cannot be implemented everywhere. In addition, it mixes thermal dissipation with transient response of the wires.

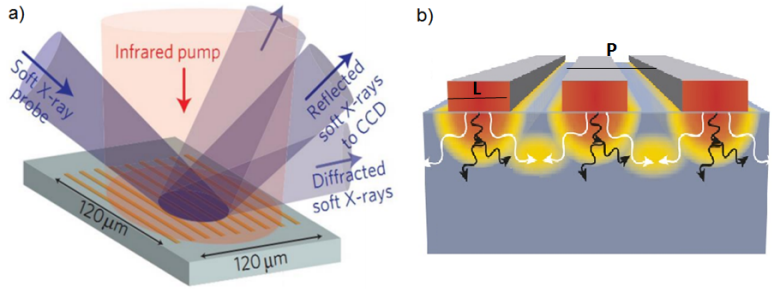

Figure 2.5. *(a) Schematic illustration of the pump and probe beam illumination geometry at the sample, (b) Schematic illustration of the nanowires on top of the probed substrate [29].*

Other optics-based techniques are also possible. Some of them are widespread, such as the Laser Flash Method [30, 31] but can be classified among the previous categories since they are based on the same principles. We refer the reader to the literature for those methods [32].

2.2.2. Electrical probe techniques

1. *Scanning thermal microscopy*

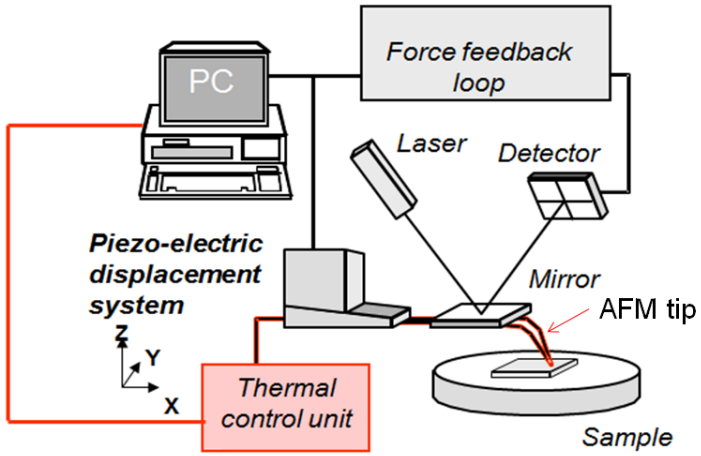

Figure 2.6. *A schematic of SThM mounted on an AFM tip [33].*

Scanning thermal microscopy (SThM) [34, 35, 36, 37] is an atomic force microscopy (AFM)–based technique. The technique was invented in 1986 by Williams and Wickramasinghe [38] to provide the topography of electrically insulating materials. The technique is a non-destructive technique that allows the characterization of sample materials. It operates by attaching a temperature sensor on the apex of the tiny tip in close proximity to a sample solid surface. In a spread configuration, the tip heats due to Joule effect. Thereby, one realizes nanoscale temperature measurement while simultaneously obtaining topographical and contact thermal images [38, 39, 40, 41]. Since SThM signals depends strongly on the surface state of the material, the spatial resolution of this technique is limited by the size of the thermal probe. However, a high spatial resolution $\backsim$ 10 nm and quantitatively mapping temperature fields with $\backsim$ 15 mK temperature resolution [42] has been recently described with an ultra-high vacuum (UHV)-based SThM technique. A schematic diagram of SThM that is based on AFM is presented in Fig. 2.6.

There are two different configurations modes while working with SThM, the passive mode which is mainly used to map the temperature at the surface of active/heating samples to study local heat source as an example [43] and the passive probe based on a resistance wire which is used as a heater/thermometer, aiming at measuring the thermal conductivity of the sample (at least its local thermal conductance). In both modes, the electrical resistance is made of thermosensitive element and thus temperature is controlled through an electrical unit.

The 3ω method (see below) and SThM with thermo–resistance are both based

on resistive thermometry. But AFM with other sensors than resistive wires are possible (eg. thermocouple, etc.).

2. *Electrothermal technique with deposited wires*

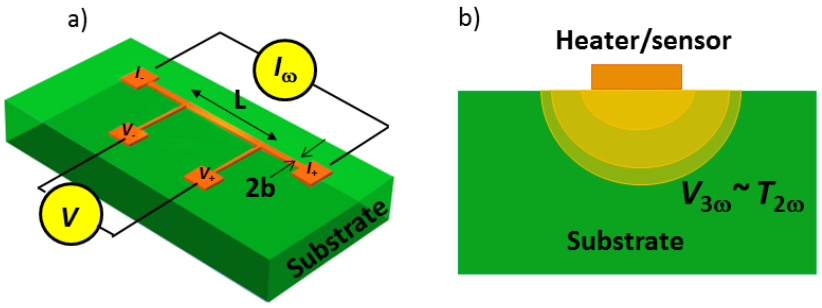

Figure 2.7. *Deposited metallic wire on top of substrate: (a) Heater/sensor in the 3ω method. (b) Cross sectional view.*

The method consists in depositing a narrow metal line (often Au or Pt, the detail will be explained in Chapter 4) on top of a flat substrate. The line serves both a heater and a thermometer. A schematic of the 3ω method is presented in Fig. 2.7, where L is the length of the heater and can be as large as 1 cm in the longitudinal direction, $2b$ is the width. This is the focus of the next section.

2.3. Focus on the four-probe electrical measurement technique

In this section, we will describe the technique used to measure the thermal conductivity of different materials either in steady state with the dc method, or with a time–dependent (transient) method. The measurement technique is based on a four–probe electrical device involving a metallic filament that serves both a resistance heater and a resistance thermometer detector concomitantly. The schematic setup of the sample is shown in Fig. 2.7. The principle of the measurement is that the electrical resistance R of the heater depends linearly on its temperature at first order,

$$R = R_0 \left(1 + \alpha \Delta T\right), \tag{2.1}$$

where R_0 is the heater resistance without considering any heating conditions and α is the temperature coefficient of the resistance (TCR) in K^{-1}. The sensitivity of the thermometer is calculated from the slope of the resistance

$$R_0\alpha = \frac{dR}{dT}. \tag{2.2}$$

2.3.1. DC measurements

By passing a current through the heater, heat will be generated due to Joule effect according to the following formula:

$$P = RI^2. \tag{2.3}$$

This heat will generate an increase of temperature θ_{DC}:

$$T = T_0 + \theta_{DC}. \tag{2.4}$$

The temperature can be measured by monitoring the variation of the electrical resistance R. Measuring R can be done in DC with the help of a Wheatstone bridge or more smartly by passing also a small sine current in addition to the DC one:

$$I(t) = I_{DC} + I_0\cos(\omega t), \qquad I_0 \ll I_{DC} \tag{2.5}$$

with a lock-in amplifier, it is possible to measure directly R and its increase due to the heating. Therefore, thermal conductance G_{th} can be expressed as

$$G_{th} = \frac{P}{\theta_{DC}}. \tag{2.6}$$

This technique was used in [44].

2.3.2. 3ω method

The 3ω method [45, 46, 47, 48, 49, 39] was designed for measuring the thermal conductivity of thin films and bulk materials. A schematic of the 3ω method is presented in Fig.

2.7. An AC driving current of frequency f is applied through the two outer pads of the device

$$I(t) = I_0 \cos(\omega t), \tag{2.7}$$

with angular frequency $\omega = 2\pi f$ is applied through the metallic wire, where I_0 is the current amplitude passing through the heater. Due to the Joule effect, the metallic wire will undergo Joule heating. The power is defined as

$$P(t) = RI^2(t), \tag{2.8}$$

which can be expended:

$$P = \frac{1}{2} I_0^2 R_0 (1 + \cos(2\omega t)). \tag{2.9}$$

The power dissipated through the heater is composed of two components: P_{AC} is the component that depends on the second harmonic oscillation 2ω and the constant component is P_{DC} which is independent of frequency.

$$\begin{cases} P_{DC} = \frac{1}{2} I_0^2 R_0 \\ P_{AC}(t) = \frac{1}{2} I_0^2 R_0 \cos(2\omega t) \end{cases} \tag{2.10}$$

Since the resistance of the heater is linearly proportional to the temperature rise of the heater, the corresponding temperature in the substrate is composed of two components, the DC component and the second harmonic (2ω) AC component. The temperature of the heater in response to the thermometer is expressed as:

$$T(t) = T_0 + \theta_{DC} + |\theta_{2\omega}| \cos(2\omega t + \varphi_{2\omega}), \tag{2.11}$$

where $\varphi_{2\omega}$ is a phase due to possible lag between temperature and the flux. Therefore, the variation of temperatures yields to:

$$\Delta T(t) = T(t) - T_0 \tag{2.12}$$

$$= \theta_{DC} + |\theta_{2\omega}| \cos(2\omega t + \varphi_{2\omega}), \tag{2.13}$$

where $|\theta_{2\omega}|$ is the amplitude of the temperature rise corresponding to AC component of power $P_{AC}(t)$, θ_{DC} is the steady state temperature increase due to time independent

component of power P_{DC}. Substituting Eq. 2.13 in Eq. 2.1, the resistance of the metallic line due to temperature increase is

$$\begin{aligned} R(t) &= R_0\left(1+\alpha\Delta T(t)\right) && (2.14)\\ &= R_0(1+\alpha(\theta_{DC}+|\theta_{2\omega}|\cos(2\omega t+\varphi_{2\omega}))) && (2.15)\\ &= R_0+R_0\alpha\theta_{DC}+R_0\alpha|\theta_{2\omega}|\cos(2\omega t+\varphi_{2\omega}). && (2.16)\end{aligned}$$

Consequently, the resistance is modulated at second harmonic frequency. If we consider Ohm's law, the voltage drop across the heater results from the multiplication of the heater resistance (Eq. 2.16) by the input current (Eq. 2.7) yielding

$$\begin{aligned} V(t) &= R(t)I(t)\\ &= R_0\left(1+\alpha\Delta T(t)\right)I_0\cos(\omega t)\\ &= R_0\left(1+\alpha(\theta_{DC}+|\theta_{2\omega}|\cos(2\omega t+\varphi_{2\omega}))\right)I_0\cos(\omega t)\\ &= R_0I_0\cos(\omega t)+\alpha\theta_{DC}R_0I_0\cos(\omega t)+\alpha|\theta_{2\omega}|R_0I_0\cos(\omega t)\cos(2\omega t+\varphi_{2\omega})\\ &= R_0I_0(1+\alpha\theta_{DC})\cos(\omega t)+\alpha|\theta_{2\omega}|R_0I_0\cos(\omega t)\cos(2\omega t+\varphi_{2\omega})\\ &= \left[R_0I_0(1+\alpha\theta_{DC})\cos(\omega t)+\frac{\alpha|\theta_{2\omega}|R_0I_0\cos(\omega t+\varphi_{2\omega})}{2}\right]+\left[\frac{\alpha|\theta_{2\omega}|R_0I_0\cos(3\omega t+\varphi_{2\omega})}{2}\right]. \end{aligned} \quad (2.17)$$

In the above expression, the voltage at 1ω is based on the DC resistance of the heater and the components θ_{DC} and $\theta_{2\omega}$. Measuring the voltage signal at 3ω is challenging because it is smaller by three order of magnitude of the first voltage signal 1ω due to the low value of α ($\approx 10^{-3}$K). However, the voltage at 3ω is directly proportional to the temperature oscillation at 2ω: it is a direct thermometer of $\theta_{2\omega}$. The voltage $V_{3\omega}$ of the wire is measured by using a lock-in amplifier (LIA) set–up, which can also be used as bridge to remove a large $V_{1\omega}$ before measuring the third harmonic voltage signal 3ω. Consequently, the third harmonic component leads us to the values of $\theta_{2\omega}$ and $\varphi_{2\omega}$ as

$$V_{3\omega} = \frac{\alpha|\theta_{2\omega}|R_0I_0\cos(3\omega t+\varphi_{2\omega})}{2} \quad (2.18)$$

$$|V_{3\omega}| = \frac{1}{2}V_0\alpha|\theta_{2\omega}| \qquad \text{and} \qquad \arg(V_{3\omega}) = \varphi_{2\omega}, \quad (2.19)$$

where $V_0 = R_0 I_0$ is close to the peak amplitude of the voltage in the metallic line at first harmonic. We recall that both the third harmonic voltage $V_{3\omega}$ and the temperature oscillation temperature $\theta_{2\omega}$ are composed of an in–phase (real) and an out–of–phase (imaginary) components. By rearranging $V_{3\omega}$, the temperature amplitude of the heater can be measured as:

$$|\theta_{2\omega}| = \frac{2|V_{3\omega}|}{\alpha R_0 I_0} \simeq \frac{2|V_{3\omega}|}{\alpha |V_{1\omega}|}. \tag{2.20}$$

The complete solution starting from the 2D heat conduction equation till finding the exact equation of temperature oscillation through which the thermal conductivity of the sample can be determined will be explained in Chapter 3. The analysis of the change of temperature amplitude with respect to frequency and the phase provides clues about the thermal properties of the sample it is lying on. Indeed, if the sample is thermally conductive, the wire will not be heated enough, since the thermal flux spreads into the sample. Conversely, if the sample is thermally insulating, the temperature of the wire will increase, because the heat will not be allowed to flow into the sample. The 3ω method was adapted for the measurement of freestanding membranes [50, 51, 52], anisotropic thin–films in–plane and cross–plane thermal conductivity [6, 53] and nanowires [54, 55]. Furthermore, it has been recently extended to thermal characterization of 20 nm thin films [56, 57]. In our experiment we have often measured the first harmonic, at low frequency when $|\theta_{2\omega}| \approx \theta_{DC}$.

2.4. Comparison between optical and non optical techniques

Various techniques have been proposed with spatial resolutions varying between few microns and a few tens of nanometers. The goal of this brief section is to show that electrical methods and optical ones are comparable for the determination of thermal properties of nanomaterials of interest. The comparison between different techniques is presented in the following Table 2.2.

Very recently, the combination of ultrafast techniques with patterned surfaces has been developed, in order to study sizes smaller than that limited by diffraction. The first studies [58] allow finding results on sub-mean free path sources, in a similar fashion to the one we will deal with (see Section 2.3 and Chapters 5 and 6).

Technique	Advantages	Disadvantages
TTR [3, 9] **TDTR** [6, 43, 44, 45, 46] **Photothermal Spectroscopy** [12, 29, 47]	- Non-invasive - Spatially-resolved - One spot → radial geometry - Temperature range [20 K-RT or higher] - Achieves micronscale spatial resolution, comparable to phonon MFPs. - No need for electrical insulation - Can separate the metal/film boundary conductance from the thermal conductivity - Dynamics down to 100 fs regime	- Limited in µm size regime - Requires often metal film deposition - Accuracy is limited due to metal film thickness and the heat capacity of the sample if the film is thick - It is not always possible to totally separate surface deformation effects from the refractive-index gradient effects
Infrared (IR) thermometry [11, 21]	- Non-invasive - No external source required, only heating - Spectroscopy is possible - Possible at very-high temperature	- Constraints on sample thickness - Limited in ~10 µm size regime - No dynamics
Raman thermometry [11, 13, 14, 48, 49, 50]	- Non-invasive - Spatially-resolved at µm - Spectroscopy is possible	- Limitations: micron spot size - Long acquisition times - Sensitivity in temperature limited at ~1K - No dynamics
Transient Thermal Grating (TTG) [15, 51, 17]	- Non-invasive - Small amount of a sample is required for the signal detection - Time response in the ns regime	- Limited in µm size regime
SThM [28, 52, 53, 54, 55, 56]	- Spatial resolution 100 nm or larger - May be nanometric at contact - Non-destructive but surface contact - Amount of heat input into the sample can be precisely controlled	- Materials thermal conductivity should be much smaller than tip's material - Thermal contact between the probe and the sample becomes strongly affected by the nanoscale - No dynamics
3ω [18, 33 , 38, 57]	- Temperature rise can be accurately determined, down to <0.01 K - High accuracy in thermal conductivity measurement, particularly for bulks and low thermal conductivity dielectric films - Wide temperature range	- Huge material flat surface required - Can require additional insulating thin film for electrically-conducting materials - Cannot separate the metal/film interfacial boundary conductance from the thermal conductivity - Invasive and requires lithography steps - Very-low frequency dynamics

Table 2.2. *Comparison between different characterization techniques*

2.5. Summary

There is a variety of nanoscale thermometry techniques which are useful for the determination of thermal properties of nanomaterials. We have seen that local measurement as well as accurate ones as a function of temperature can be performed with the same type of setups. Different strategies can be dedicated to measure thermal properties of materials either by optical or electrical methods. Using the four–probe electrical technique, thermal conductivity measurements can be performed either in steady state (DC) or by using an AC time-dependent 3ω method. A comparison between the different techniques were performed.

In our study, we choose an electrical technique instead of an optical one to perform measurements with the smallest possible heat sources as they are not diffraction-limited. We have seen that other methods involving optics can maybe now compete with our choice, but they do not allow to study the single heater case. Our goal is to move toward the study of the 2D Cartesian geometry as a function of temperature. While this was not discussed in detail in this Chapter, note that our configuration may also help us to find clues about the boundary conductance at interfaces.

References

[1] D. Li, S. T. Huxtable, A. R. Abramson and A. Majumdar, *Thermal transport in nanostructured solid-state cooling devices*, Journal of Heat Transfer **127**, 108 (2005).

[2] P. E. Hopkins and J. C. Duda, *Introduction to nanoscale thermal conduction*, (2011).

[3] R. J. Stevens, A. N. Smith and P. M. Norris, *Measurement of thermal boundary conductance of a series of metal-dielectric interfaces by the transient thermoreflectance technique*, Journal of Heat Transfer **127**, 315 (2005).

[4] K. Termentzidis, J. Parasuraman, C. A. Da Cruz, S. Merabia, D. Angelescu, F. Marty, T. Bourouina, X. Kleber, P. Chantrenne and P. Basset, *Thermal conductivity and thermal boundary resistance of nanostructures*, Nanoscale Research Letters **6**, 1 (2011).

[5] Y. K. Koh, S. L. Singer, W. Kim, J. M. Zide, H. Lu, D. G. Cahill, A. Majumdar and A. C. Gossard, *Comparison of the 3w method and time-domain thermoreflectance for measurements of the cross-plane thermal conductivity of epitaxial semiconductors*, Journal of Applied Physics **105**, 54303 (2009).

[6] D. G. Cahill, K. Goodson and A. Majumdar, *Thermometry and thermal transport in micro/nanoscale solid-state devices and structures*, Journal of Heat Transfer **124**, 223 (2002).

[7] N. Del Fatti, C. Voisin, M. Achermann, S. Tzortzakis, D. Christofilos and F. Vallée, *Nonequilibrium electron dynamics in noble metals*, Physical Review B **61**, 16956 (2000).

[8] C. Voisin, N. Del Fatti, D. Christofilos and F. Vallée, *Ultrafast electron dynamics and optical nonlinearities in metal nanoparticles*, The Journal of Physical Chemistry B **105**, 2264 (2001).

[9] A. Arbouet, C. Voisin, D. Christofilos, P. Langot, N. Del Fatti, F. Vallée, J. Lermé, G. Celep, E. Cottancin, M. Gaudry *et al.*, *Electron-phonon scattering in metal clusters*, Physical Review Letters **90**, 177401 (2003).

[10] K. T. Regner, D. P. Sellan, Z. Su, C. H. Amon, A. J. McGaughey and J. A. Malen, *Broadband phonon mean free path contributions to thermal conductivity measured using frequency domain thermoreflectance*, Nature communications **4**, 1640 (2013).

[11] D. G. Cahill, P. V. Braun, G. Chen, D. R. Clarke, S. Fan, K. E. Goodson, P. Keblinski, W. P. King, G. D. Mahan, A. Majumdar *et al.*, *Nanoscale thermal transport. II. 2003–2012*, Applied Physics Reviews **1**, 011305 (2014).

[12] Y. Ezzahri, S. Grauby, S. Dilhaire, J. Rampnoux and W. Claeys, *Cross-plan Si/SiGe superlattice acoustic and thermal properties measurement by picosecond ultrasonics*, Journal of Applied Physics **101**, 3705 (2007).

[13] A. J. Minnich, J. Johnson, A. Schmidt, K. Esfarjani, M. Dresselhaus, K. A. Nelson and G. Chen, *Thermal conductivity spectroscopy technique to measure phonon mean free paths*, Physical Review Letters **107**, 095901 (2011).

[14] J. P. Freedman, J. H. Leach, E. A. Preble, Z. Sitar, R. F. Davis and J. A. Malen, *Universal phonon mean free path spectra in crystalline semiconductors at high temperature*, Scientific reports **3**, (2013).

[15] A. J. Schmidt, X. Chen and G. Chen, *Pulse accumulation, radial heat conduction, and anisotropic thermal conductivity in pump-probe transient thermoreflectance*, Review of Scientific Instruments **79**, 114902 (2008).

[16] D. Ding, X. Chen and A. Minnich, *Radial quasiballistic transport in time-domain thermoreflectance studied using Monte Carlo simulations*, Applied Physics Letters **104**, 143104 (2014).

[17] Y. K. Koh and D. G. Cahill, *Frequency dependence of the thermal conductivity of semiconductor alloys*, Physical Review B **76**, 075207 (2007).

[18] A. Minnich, *Determining phonon mean free paths from observations of quasiballistic thermal transport*, Physical Review Letters **109**, 205901 (2012).

[19] L. Zeng, Dissertation, Massachusetts Institute of Technology, 2013.

[20] L. M. Phinney, W.-Y. Lu and J. R. Serrano, *Raman and Infrared Thermometry for Microsystems*, Journal of Thermal Science and Engineering Applications **5**, 031011 (2013).

[21] S. Bialkowski, *Photothermal spectroscopy methods for chemical analysis*, **134**, (1996).

[22] Y. Yue, G. Eres, X. Wang and L. Guo, *Characterization of thermal transport in micro/nanoscale wires by steady-state electro-Raman-thermal technique*, Applied Physics A **97**, 19 (2009).

[23] T. E. Beechem III and J. R. Serrano, *Raman Thermometry of Microdevices: Comparing Methods to Minimize Error.*, (2011).

[24] I.-C. Khoo and R. Normandin, *The mechanism and dynamics of transient thermal grating diffraction in nematic liquid crystal films*, Quantum Electronics, IEEE Journal of **21**, 329 (1985).

[25] A. A. Maznev, J. A. Johnson and K. A. Nelson, *Onset of nondiffusive phonon transport in transient thermal grating decay*, Physical Review B **84**, 195206 (2011).

[26] J. A. Johnson, A. A. Maznev, M. T. Bulsara, E. A. Fitzgerald, T. Harman, S. Calawa, C. Vineis, G. Turner and K. A. Nelson, *Phase-controlled, heterodyne laser-induced transient grating measurements of thermal transport properties in opaque material*, Journal of Applied Physics **111**, 023503 (2012).

[27] Q. Li, K. Hoogeboom-Pot, D. Nardi, M. M. Murnane, H. C. Kapteyn, M. E. Siemens, E. H. Anderson, O. Hellwig, E. Dobisz, B. Gurney *et al.*, *Generation and control of ultrashort-wavelength two-dimensional surface acoustic waves at nanoscale interfaces*, Physical Review B **85**, 195431 (2012).

[28] D. Nardi, K. M. Hoogeboom-Pot, J. N. Hernandez-Charpak, M. Tripp, S. W. King, E. H. Anderson, M. M. Murnane and H. C. Kapteyn, *SPIE Advanced Lithography*, 86810N (2013).

[29] K. M. Hoogeboom-Pot, J. N. Hernandez-Charpak, X. Gu, T. D. Frazer, E. H. Anderson, W. Chao, R. W. Falcone, R. Yang, M. M. Murnane, H. C. Kapteyn *et al.*, *A new regime of nanoscale thermal transport: Collective diffusion increases dissipation efficiency*, Proceedings of the National Academy of Sciences **112**, 4846 (2015).

[30] H. Mehling, G. Hautzinger, O. Nilsson, J. Fricke, R. Hofmann and O. Hahn, *Thermal diffusivity of semitransparent materials determined by the laser-flash method applying a new analytical model*, International Journal of Thermophysics **19**, 941 (1998).

[31] T. Baba and A. Ono, *Improvement of the laser flash method to reduce uncertainty in thermal diffusivity measurements*, Measurement Science and Technology **12**, 2046 (2001).

[32] S. Volz, *Microscale and nanoscale heat transfer*, (2007).

[33] A. Assy and S. Gomès, *Heat transfer at nanoscale contacts investigated with scanning thermal microscopy*, Applied Physics Letters **107**, 043105 (2015).

[34] H. Pollock and A. Hammiche, *Micro-thermal analysis: techniques and applications*, Journal of Physics D: Applied Physics **34**, R23 (2001).

[35] P.-O. Chapuis, S. K. Saha and S. Volz, *Quantitive 3w-sxanning thermal microscopy: Modelling the AC/DC coupling and the sample heat conduction*, arXiv preprint arXiv:0709.1835 (2007).

[36] B. Cretin, S. Gomes, N. Trannoy and C. . Vairac, Pascal, *Microscale and nanoscale heat transfer*, 181 (2007).

[37] S. Lefèvre and S. Volz, *3ω-scanning thermal microscope*, Review of Scientific Instruments **76**, 033701 (2005).

[38] C. Williams and H. Wickramasinghe, *Scanning thermal profiler*, Applied Physics Letters **49**, 1587 (1986).

[39] W. Jaber, A. Assy, S. Lefèvre, S. Gomès and P.-O. Chapuis, *Thermal Investigations of ICs and Systems (THERMINIC), 2013 19th International Workshop*, 54 (2013).

[40] A. Majumdar, J. Carrejo and J. Lai, *Thermal imaging using the atomic force microscope*, Applied Physics Letters **62**, 2501 (1993).

[41] A. Majumdar, J. Lai, M. Chandrachood, O. Nakabeppu, Y. Wu and Z. Shi, *Thermal imaging by atomic force microscopy using thermocouple cantilever probes*, Review of Scientific Instruments **66**, 3584 (1995).

[42] K. Kim, W. Jeong, W. Lee and P. Reddy, *Ultra-high vacuum scanning thermal microscopy for nanometer resolution quantitative thermometry*, Acs Nano **6**, 4248 (2012).

[43] B. Gotsmann, M. A. Lantz, A. Knoll and U. Dürig, *Nanoscale thermal and mechanical interactions studies using heatable probes*, Nanotechnology (2010).

[44] P.-O. Chapuis, M. Prunnila, A. Shchepetov, L. Schneider, S. Laakso, J. Ahopelto and C. Sotomayor Torres, *Thermal Investigations of ICs and Systems (THERMINIC), 2010 16th International Workshop*, 1 (2010).

[45] D. G. Cahill, *Thermal conductivity measurement from 30 to 750 K: the 3ω method*, Review of Scientific Instruments **61**, 802 (1990).

[46] T. Borca-Tasciuc, A. Kumar and G. Chen, *Data reduction in 3ω method for thin-film thermal conductivity determination*, Review of Scientific Instruments **72**, 2139 (2001).

[47] D. De Koninck, *Thermal Conductivity Measurements Using the 3-Omega Technique: Application to Power Harvesting Microsystems (Thesis)*, McGill University (2008).

[48] J.-Y. Duquesne, D. Fournier and C. Frétigny, *Analytical solutions of the heat diffusion equation for 3ω method geometry*, Journal of Applied Physics **108**, 086104 (2010).

[49] T. Hnninen, *Implementing the 3-omega technique for thermal conductivity measurements*, (2013).

[50] A. Jain and K. E. Goodson, *Measurement of the thermal conductivity and heat capacity of freestanding shape memory thin films using the 3ω method*, Journal of Heat Transfer **130**, 102402 (2008).

[51] Y. Ju and K. Goodson, *Phonon scattering in silicon films with thickness of order 100 nm*, Applied Physics Letters **74**, 3005 (1999).

[52] W. Liu, T. Borca-Tasciuc, G. Chen, J. Liu and K. Wang, *Anisotropic thermal conductivity of Ge quantum-dot and symmetrically strained Si/Ge superlattices*, Journal of nanoscience and nanotechnology **1**, 39 (2001).

[53] T. Borca-Tasciuc, D. Song, J. Meyer, I. Vurgaftman, M. Yang, B. Nosho, L. Whitman, H. Lee, R. Martinelli and G. Turner, *Thermal Conductivity of AlAs (0.07) Sb (0.93) and Al (0.9) Ga (0.1) As (0.07) Sb (0.93) Alloys and (AlAs) 1/(AlSB) 11 Digital-Alloy Superlattices*, (2002).

[54] O. Bourgeois, T. Fournier and J. Chaussy, *Measurement of thermal conductance of silicon nanowires at low temperature*, Journal of Applied Physics, 016104 (2007).

[55] D. Li, Y. Wu, P. Kim, L. Shi, P. Yang and A. Majumdar, *Thermal conductivity of individual silicon nanowires*, Applied Physics Letters **83**, 2934 (2003).

[56] K. E. Goodson and Y. S. Ju, *Heat conduction in novel electronic films*, Annual Review of Materials Science **29**, 261 (1999).

[57] T. Borca-Tasciuc and G. Chen, *Thermal Conductivity*, 205 (2004).

[58] Y. Hu, L. Zeng, A. J. Minnich, M. S. Dresselhaus and G. Chen, *Spectral mapping of thermal conductivity through nanoscale ballistic transport*, Nature nanotechnology (2015).

CHAPTER 3

Analytical and numerical studies of diffusive heat conduction

This chapter is mainly devoted to analytical and numerical studies of diffusive heat conduction depending on the heater size on top of flat substrate and on the geometry. In Section 3.1, we study analytically the 2D heat conduction in cylindrical geometry. First we introduce the transient regime for a line heat source and then we study it in the case of the 3ω method. The effect of an oxide layer on the temperature field is analysed. General solution for 2D heat conduction across a multilayer structure and the impact of oxide layer on thermal conductance is presented in Section 3.2. Section 3.3 is dedicated to the 2D and 3D numerical simulations. The effect of the packaging on the thermal conductance is introduced. Finally, we show the impact of the heater thickness and the impact of the thermal boundary resistance in 3D on thermal conductance.

3.1. 2D heat conduction in cylindrical geometry

3.1.1. Physics of heat conduction in cylindrical geometry

When there is no heat generation, the heat equation in cylindrical geometry can be written as

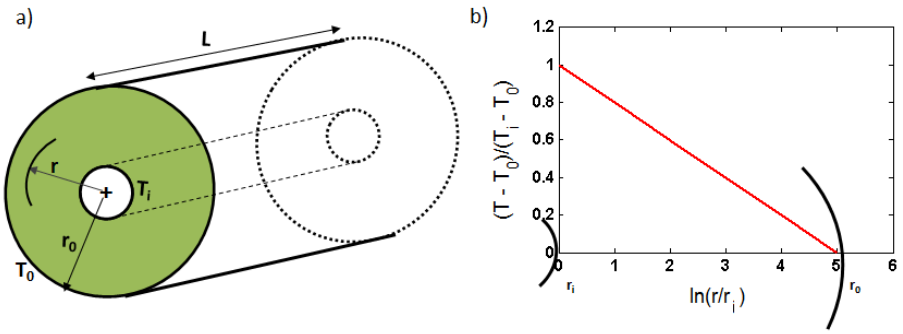

Figure 3.1. *A schematic illustration of (a) the geometry of the hollow cylinder, and (b) the temperature profile.*

$$\frac{1}{r}\frac{\partial}{\partial r}\left(\kappa r\frac{\partial T(r)}{\partial r}\right)+\kappa\frac{1}{r}\frac{\partial T(r)}{\partial \theta}+\kappa\frac{\partial^2 T(r)}{\partial^2 z}=0. \tag{3.1}$$

Consider the infinite hollow cylinder with inner and outer radii r_i and r_0, respectively. Then $T(r,z)=T(r)$ and

$$\frac{1}{r}\frac{\partial}{\partial r}\left(\kappa r\frac{\partial T(r)}{\partial r}\right)=0. \tag{3.2}$$

The temperature distribution in the cylinder can be determined by solving Eq. 3.2 and applying the boundary conditions. Integrate twice Eq. 3.2 and then we can obtain the solution by introducing the boundary conditions:

$$T(r_i)=T_i \qquad \text{and} \qquad T(r_0)=T_0. \tag{3.3}$$

The solution is

$$\frac{T(r)-T_0}{T_i-T_0}=\frac{\ln\left(\frac{r}{r_0}\right)}{\ln\left(\frac{r_i}{r_0}\right)}. \tag{3.4}$$

It is plotted in Fig. 3.1-b where the temperature profile is logarithmic. From Fourier's law the heat transfer rate is linked to the temperature difference across the cylinder:

$$P=\frac{2\pi L\kappa}{\ln\left(\frac{r_0}{r_i}\right)}(T_i-T_0), \tag{3.5}$$

where P is the power dissipated from the inner radius. Hence, the thermal conductance can be expressed as:

$$G_{th_{cyl}} = \frac{2\pi\kappa L}{\ln\left(\frac{r_0}{r_i}\right)}. \tag{3.6}$$

We find that logarithmic behavior will drive the conductance in cylindrical geometry. This a key point for all the following works.

3.1.2. Transient regime for a line heat source

We now consider the AC case. The following is based on many useful documents, as [1, 2, 3, 4, 5, 6]. Under the transient state conditions in a cylindrical system, where heat transfer is dependent of t and r, the steady–state heat equation in absence of volumetric heat source can be written as

$$\frac{\partial T(r,t)}{\partial t} = D\frac{1}{r}\frac{\partial}{\partial r}\left(r\frac{\partial T(r,t)}{\partial r}\right), \tag{3.7}$$

where D is the thermal diffusivity. Here we consider the diffusivity as independent of temperature, which is valid for small temperature variations. As introduced in Eq. 2.13, the temperature field inside the cylinder can be expressed as:

$$T(r,t) = T_0 + \Delta T_{dc}(r) + \Delta T_{ac}(r,t). \tag{3.8}$$

In the following we only consider the time–dependent part:

$$\frac{1}{D}\left(\frac{\partial \Delta T_{ac}(r,t)}{\partial t}\right) - \frac{1}{r}\frac{\partial}{\partial r}\left(r\frac{\partial \Delta T_{ac}(r,t)}{\partial r}\right) = 0. \tag{3.9}$$

The analytical solution can be obtained using the method of separation of variables. The solution is of the form

$$\Delta T_{ac}(r,t) = \theta_{ac}(r)F(t), \tag{3.10}$$

where $\theta_{ac}(r)$ is the spatial evolution of the temperature oscillation that depends on the position in space and $F(t)$ is the temporal evolution that depends only on time. Based on Eq. 2.13, the temperature oscillation takes place at the second harmonic of the excitation frequency. Therefore,

$$F(t) = \cos(2\omega t + \varphi_{2\omega}) = \Re\left(\exp(i2\omega t + \varphi_{2\omega})\right). \tag{3.11}$$

Substituting Eq. 3.10 and Eq. 3.11 in Eq. 3.9, we then obtain

$$\frac{d^2\theta_{ac}(r)}{dr^2} + \frac{1}{r}\frac{d\theta_{ac}(r)}{dr} - q^2\theta_{ac}(r) = 0, \tag{3.12}$$

where q is the wavenumber of the thermal wave given by $q^2 = \frac{2i\omega}{D}$. The real part of the reciprocal factor of the wave vector q defines the thermal wavelength and the imaginary part is referred to as the depth of the heat wave. The thermal penetration depth is a measure of how deep the thermal wave penetrates into the substrate. It is defined as follows:

$$\frac{1}{\Im(q)} = \sqrt{D/\omega}. \tag{3.13}$$

The frequency dependence of the thermal penetration depth for different materials, gold (Au), silicon (Si), germanium (Ge), sapphire (Al_2O_3 crystalline), alumina (Al_2O_3 amorphous or polycrystalline), crystal quartz, fused quartz (SiO_2 amorphous) and acrylic plastic (PCB) is shown in Fig. 3.2.

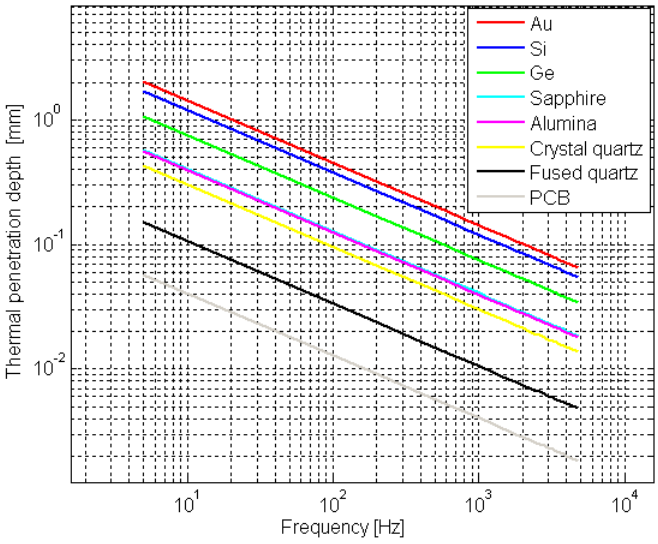

Figure 3.2. *Frequency dependence of the thermal penetration depth of different materials.*

Eq. 3.12 is the modified Bessel equation of order zero of the argument given by qr. The general solution is given by

$$\Delta T_{ac}(r,t) = \{[(C_1 \mathrm{I}_0(qr) + C_2 \mathrm{K}_0(qr)]\exp(i2\omega t + \varphi_{2\omega})\}\,, \tag{3.14}$$

where I_0 and K_0 are the Bessel functions of the first and second kinds of order zero respectively. For small qr the modified Bessel functions of zeroth order can be approximated as

$$\mathrm{K}_0(r) = -\left[\ln(\frac{r}{2})I_0(r) + \frac{r^2}{4} + ...\right], \tag{3.15}$$

and

$$\mathrm{I}_0(r) = \left[1 + \frac{r^2}{4} + ...\right]. \tag{3.16}$$

The constants C_1 and C_2 can be determined with the boundary conditions. By means of Matlab, Bessel functions of the first and second kinds of zeroth order are computed, the first function I_0 diverges for a large value of qr while the second function K_0 converges as shown in Fig. 3.3.

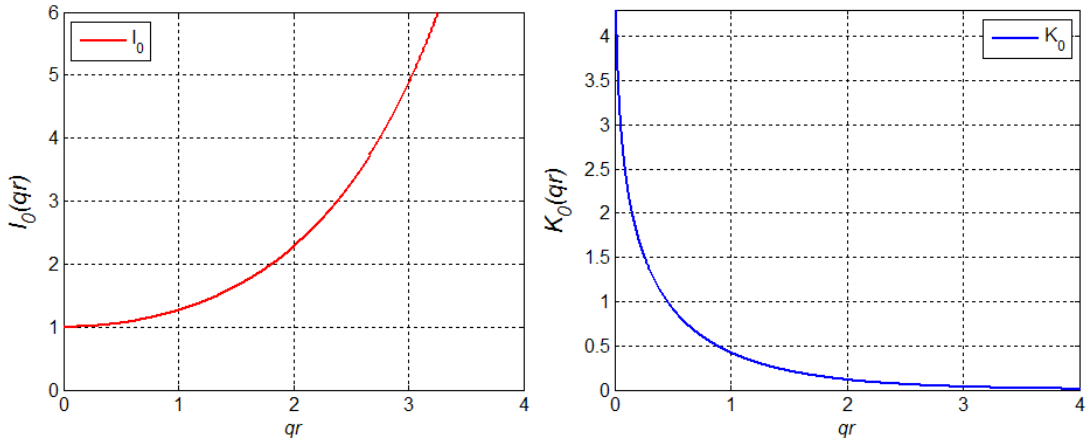

Figure 3.3. *Modified Bessel functions of the first and second kinds of zeroth order $I_0(qr)$ and $K_0(qr)$, respectively.*

As a result,

$$\lim_{r \to +\infty} \Delta T_{ac}(r,t) = 0 \Longrightarrow C_1 = 0. \tag{3.17}$$

The second boundary conditions is at the inner radius r_i, where the total heat flux across

the surface is imposed to be constant. We consider the case $r_i \to 0$. As the radius r tends to zero, one can write

$$\lim_{r\to 0}\left[-\kappa(2\pi r_i L)\left[\frac{\partial}{\partial r}\left(C_2 \mathrm{K}_0(qr)\exp(i2\omega t)\right)\right]_{r=r_i}\right] = P\exp(i2\omega t + \varphi_{2\omega}), \tag{3.18}$$

where P/L is the dissipated electrical power per unit length. The two following relations found in Carslaw and Jaeger [5] and Cahill [6] allow to calculate C_2:

$$\begin{cases} \dfrac{d}{dr}\mathrm{K}_0(qr) = -q\mathrm{K}_1(qr) \\ r \to 0, \quad \mathrm{K}_1(qr) \sim \frac{1}{q.r} \end{cases} \tag{3.19}$$

$$C_2 = \frac{P}{2\pi L\kappa}. \tag{3.20}$$

Therefore, the oscillating temperature field is

$$\Delta T_{ac}(r,t) = \Re\left\{\left[\frac{P}{2\pi L\kappa}\mathrm{K}_0(qr)\right]\exp(i2\omega t + \varphi_{2\omega})\right\} = |\hat{\theta}_{ac}(r)|\cos(2\omega t + \varphi_{2\omega}), \tag{3.21}$$

with

$$\hat{\theta}_{ac}(r) = \frac{P}{2\pi L\kappa}\mathrm{K}_0(qr) = \hat{\theta}_{ac,x}(r) + i\hat{\theta}_{ac,y}(r), \tag{3.22}$$

and therefore

$$\begin{cases} \hat{\theta}_{ac,x}(r) = \frac{P}{2\pi L\kappa}\Re(\mathrm{K}_0(qr)) \\ \hat{\theta}_{ac,y}(r) = \frac{P}{2\pi L\kappa}\Im(\mathrm{K}_0(qr)) \end{cases} \tag{3.23}$$

where $\Re$ and $\Im$ are the real and imaginary parts of K_0 respectively.

3.1.3. Case of the 3ω method

Eq. 3.22 is derived for a one dimensional line heater on the surface of the substrate. For the heater with a finite width $2b$, we have to consider a large number of 1D line

sources over the width of the heater [6]. Mathematically, this is done by taking the Fourier transform of Eq. 3.23 with respect to x coordinate and convoluting it with the size of the heater temperature, which is the same as the substrate surface temperature under the heater, thus the oscillation at the surface is important. As such, let $y = 0, r = x$. Therefore

$$\hat{\theta}_{ac}(\lambda) = \int_{-\infty}^{\infty} \hat{\theta}_{ac}(x) e^{-i\lambda x} dx \tag{3.24}$$

$$\hat{\theta}_{ac}(x) = \frac{1}{\sqrt{2\pi}} \int_{-\infty}^{\infty} \hat{\theta}_{ac}(\lambda) e^{i\lambda x} d\lambda, \tag{3.25}$$

where λ is the wave vector. Bessel function of an odd integer order is considered an odd function while a Bessel function of an even integer order is an even function. Thus, Eq. 3.24 and Eq. 3.25 are reduced to the cosine Fourier transform since the temperature field is an even function:

$$\hat{\theta}_{ac}(\lambda) = 2 \int_{0}^{\infty} \hat{\theta}_{ac}(x) \cos(\lambda x) dx \tag{3.26}$$

$$\hat{\theta}_{ac}(x) = \frac{1}{\sqrt{\pi}} \int_{0}^{\infty} \hat{\theta}_{ac}(\lambda) \cos(\lambda x) d\lambda. \tag{3.27}$$

It happens that the temperature oscillation (3.23) in the Fourier space λ is given by a simple formula [7]:

$$\hat{\theta}_{ac}(\lambda) = \frac{P}{L\kappa} \left(\frac{1}{\sqrt{\lambda^2 + q^2}} \right). \tag{3.28}$$

For a finite heater width, the heat is assumed to enter the substrate uniformly across the finite width $2b$. This behavior can be expressed as the rectangular function ($\mathrm{rect}(x)$) with values 1 for $x < b$ and 0 elsewhere. The Fourier transform of such source is given by:

$$\int_{0}^{\infty} \mathrm{rect}(x) \cos(\lambda x) dx = \int_{0}^{b} \cos(\lambda x) dx = \frac{\sin(\lambda b)}{(\lambda b)}. \tag{3.29}$$

To include the finite heater width from x=0 to b, Eq. 3.28 is multiplied by Eq. 3.29 to perform the convolution. This yields

$$\frac{P}{L\kappa}\left(\frac{1}{\sqrt{\lambda^2+q^2}}\right)\int_0^b \cos(\lambda x)dx = \frac{P}{L\kappa}\frac{\sin(\lambda b)}{(\lambda b)\sqrt{\lambda^2+q^2}}. \tag{3.30}$$

Performing the inverse Fourier transform with Eq. 3.27, we get the steady–state expression in the real space

$$\hat{\theta}_{ac}(x) = \frac{1}{\pi}\int_0^\infty \theta_{ac}(\lambda)\cos(\lambda x)dx = \frac{P}{L\kappa}\int_0^\infty \frac{\sin(\lambda b)}{(\lambda b)\sqrt{\lambda^2+q^2}}\cos(\lambda x)d\lambda. \tag{3.31}$$

Since the heater measures the average temperature over the width of the heater, Eq. 3.31 is then integrated and averaged by dividing by $2b$

$$\bar{\theta}_{ac} = \frac{1}{2b}\int_{-b}^b \theta_{ac}(x)dx = \frac{P}{\pi L\kappa}\int_{-b}^b\int_0^\infty \frac{\sin(\lambda b)}{(\lambda b)\sqrt{\lambda^2+q^2}}\cos(\lambda x)d\lambda dx. \tag{3.32}$$

Hence, by solving Eq. 3.32, the magnitude of the temperature oscillation for a finite width heater deposited on the surface of the substrate is expressed as [6]

$$\theta_{ac} = \frac{P}{\pi L\kappa}\int_0^\infty \frac{\sin^2(\lambda b)}{(\lambda b)^2\sqrt{\lambda^2+q^2}}d\lambda. \tag{3.33}$$

Note that Duquesne et al. [3] have proposed an analytical solution of Eq. 3.33 by means of Meijer-G function. Due to its simplicity we here solve directly Eq. 3.33 numerically with Mathematica. The integration is carried out for λ varying between 10^{-10} and 10^{10} m^{-1}. Fig. 3.4 shows the real and imaginary components of the temperature oscillations as a function of excitation frequency. It exhibits a "linear regime" at low frequencies and a planar regime at high frequencies. Between these two extremes, there is a transition regime.

At low frequencies the linear regime can be characterized by a constant negative out-of-phase temperature oscillation and by an in–phase temperature oscillation decaying linearly with respect to the excitation frequency. In Eq. 3.33, the integrand decreases very quickly as a function of λ because the squared cardinal sine function $\left(\frac{\sin(\mathrm{x})}{x}\right)^2$

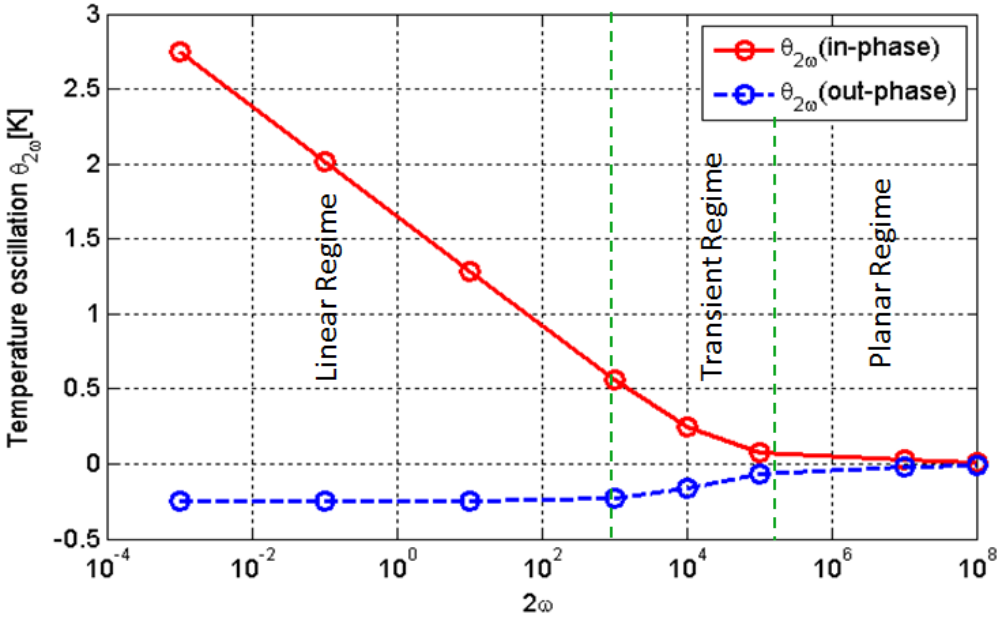

Figure 3.4. *In-phase and out-of-phase components of the temperature oscillations vs thermal excitation frequency 2ω.*

decreases quickly while it is multiplied by another decaying function. For low values of λb,

$$\lim_{b\lambda \to 0} \frac{\sin(b\lambda)}{b\lambda} = 1. \tag{3.34}$$

On the other hand, we restrict ourselves to the linear regime where the metallic line half width is much smaller than the thermal penetration depth, i.e. $b << |1/q|$. In this regime $1/b >> |q|$ and as λ takes values up to $1/b$, the integrand will behave as $1/\lambda$ provided that λ is larger than $|q|$. We find that θ will behave logarithmically. It has been shown numerically that the integral of Eq. 3.33 can be approximated by

$$\bar{\theta}_{ac}(2\omega) \approx \frac{P}{\pi L \kappa} \int_0^{1/b} \frac{1}{\sqrt{\lambda^2 + q^2}} d\lambda \approx -\frac{P}{\pi L \kappa} (\ln(qb) + Cst). \tag{3.35}$$

Here, we have included the constant as a numerical parameter ξ equal to 0.923 [8, 9]. Its analytical value has been provided by Duquesne et al., who found that $\xi = 3/2 - \gamma$, where γ is the Euler constant. Substituting $q = \sqrt{\frac{i2\omega}{D}}$ in Eq. 3.35 gives a relation between the

temperature oscillation magnitude and the excitation frequency 2ω. One gets

$$\bar{\theta}_{ac}(2\omega) = -\frac{P}{2\pi L\kappa}\left[\ln(2\omega) + \frac{1}{2}\ln(\frac{b^2}{D}) - 2\xi\right] - i\frac{P}{4L\kappa}. \tag{3.36}$$

It is composed of two parts, the real part where the in-phase temperature oscillation decays logarithmically with respect to the excitation frequency 2ω and the constant negative imaginary part of the out-of-phase temperature oscillations. Thermal conductivity of the substrate can be determined either from the real part or the imaginary part. But experimentally, it is more reliable to consider the data from the real part contribution [6]. To do so, Eq. 3.36 can be written in terms of measurable quantities by substituting Eq. 3.36 into Eq. 2.19. The third harmonic voltage $V_{3\omega}$ is given by

$$V_{3\omega} = -\frac{V_0^3\alpha}{4\pi L\kappa R_0}\left[\ln(2\omega) + \frac{1}{2}\ln(\frac{b^2}{D}) - 2\xi\right] - i\frac{V_0^3\alpha}{8\pi L\kappa R_0}. \tag{3.37}$$

The linear relation between the third harmonic voltage and the logarithm of the excitation frequency 2ω allows to calculate the slope, which is

$$slope = \frac{d(\Re(V_{3\omega}))}{d(\ln(2\omega))} = \frac{V_0^3\alpha}{4\pi L\kappa R_0}. \tag{3.38}$$

Hence, thermal conductivity of the substrate κ can be calculated through the equation:

$$\kappa = \frac{V_0^3\alpha}{4\pi L R_0} \times \frac{1}{slope}. \tag{3.39}$$

3.1.4. Dependence on width

To provide an idea of the effect of the wire width $2b$, the analytical expression of Eq. 3.36 is solved, under similar dissipation power conditions $P = 0.019$ W and a thermal diffusivity of Si $D = 8.8 \times 10^{-5}\mathrm{m}^2.\mathrm{s}^{-1}$, for values between 50 nm and 1 µm. The thermal conductivity of Si is 149 $\mathrm{W.m^{-1}.K^{-1}}$ and the circular frequency is $[0.01 - 10000]\,\mathrm{s}^{-1}$ (see Fig. 3.5). Fig. 3.5 shows that the temperature rise becomes higher as the heater width becomes narrower. The dependence is also logarithmic as shown by Eq. 3.36.

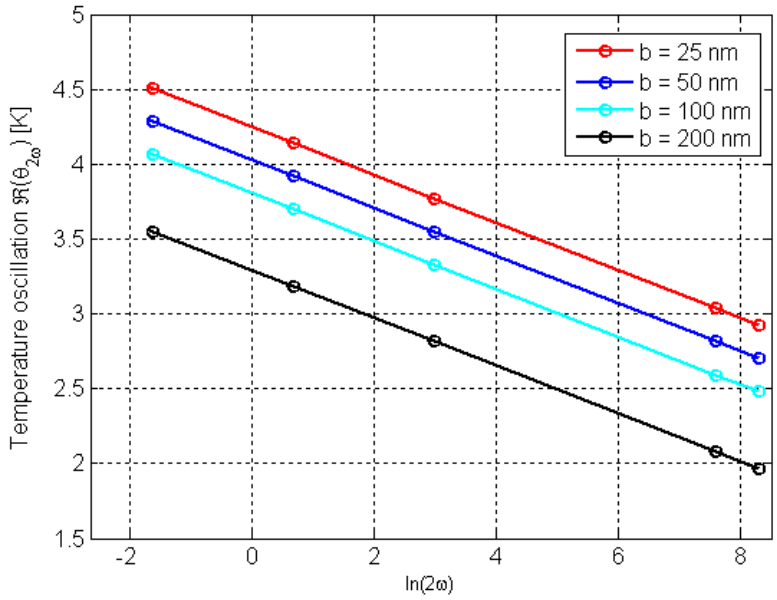

Figure 3.5. *Temperature rise $\Re(\theta_{2\omega})$ of different heater widths over a wide range of frequency*

3.1.5. Effect of an oxide layer on the temperature field

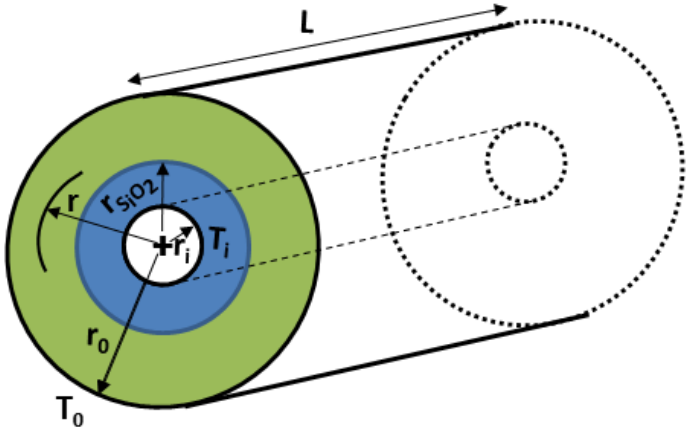

Figure 3.6. *Schematic configuration showing the oxide layer $r_{S_iO_2}$.*

Let us consider a thin film of thickness $d_F = 5$ nm and thermal conductivity $\kappa_F = 1.5\ \mathrm{W.m^{-1}.K^{-1}}$ deposited on the silicon substrate. A simple analytical study in the cylindrical geometry is made to provide a picture of the effect of the oxide layer on the

temperature rise (see Fig. 3.6). As a result

$$\theta = \frac{P}{2\pi L \kappa_F} \ln\left(\frac{r_0}{r_{S_iO_2}}\right) + \frac{P}{2\pi L \kappa_{Si}} \ln\left(\frac{r_0}{r_{S_iO_2}}\right). \tag{3.40}$$

From Eq. 3.35 we can infer that r_0 should be replaced by $1/q$ in Eq. 3.40 to analyze the behavior in the frequency regime, if the oxide layer is smaller than the thermal penetration depth. A simple constant may be added to provide the exact result. The results of such an analysis are presented in Fig. 3.7. It is seen that if the thickness of the oxide film increases the temperature rises. The temperature rise of the heater has a logarithmic proportionality to the thickness of the oxide layer. The thickness of the oxide film increases then the temperature rises. The results are presented in Fig. 3.7. It shows that when the wire becomes narrower, the oxide layer becomes as an insulating layer. The thermal measurements of the substrates will be affected especially at the nanoscale. The effect becomes particularly important for sources with radii smaller than 200 nm. While this analysis is very gross it tells us that this oxide layer can be an issue. Note that native oxide layers are usually smaller, on the order of 1–2 nm.

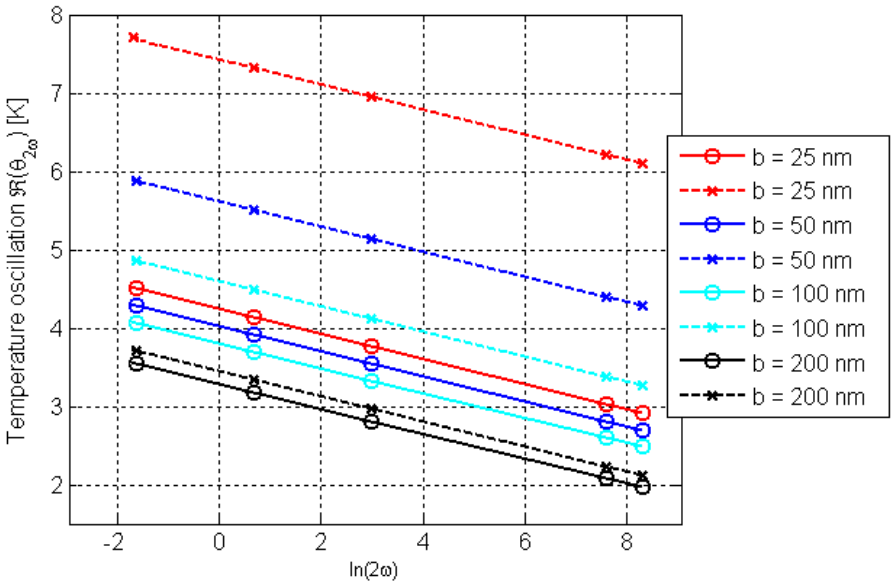

Figure 3.7. *Temperature rise $\Re(\theta_{2\omega})$ of different heater radii over a wide frequency range. Dashed lines presents the effect of the oxide layer on the temperature rise.*

3.2. General solution for 2D heat conduction across a multilayer structure

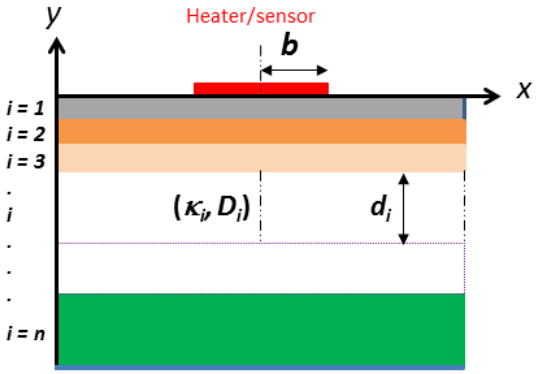

Figure 3.8. *Cross–sectional view of the heater/temperature sensor deposited on top of multilayer thin film.*

In the previous section we derived a formula for the AC temperature rise of a heater deposited on an infinite isotropic substrate. As we now turn to the real geometry, the expression for the heater temperature rise is derived in the general case across a multilayer system, that may possess anisotropic thermophysical properties. A general solution using integral Fourier transform [10, 11] has been developed by Borca–Tasciuc et al. to describe the 2D heat conduction across a multilayer system (see Fig. 3.8). In this model, the derivation is based on a two-dimensional heat conduction model across the system and a uniform heat flux boundary condition between the heater and the top film [12]. The complex temperature rise of the a heater is given by

$$\Delta T = -\frac{P}{\pi L \kappa_{y_1}} \int_0^\infty \frac{1}{A_1 B_1} \frac{\sin^2(b\lambda)}{b^2\lambda^2} d\lambda, \tag{3.41}$$

$$A_{i-1} = \frac{A_i - \frac{\kappa_{y_i} B_i}{\kappa_{y_{i-1}} B_{i-1}} - \tanh(\varphi_{i-1})}{1 - A_i \frac{\kappa_{y_i} B_i}{\kappa_{y_{i-1}} B_{i-1}} \tanh(\varphi_{i-1})}, \qquad i = 2...n, \tag{3.42}$$

$$B_i = \left(\kappa_{xy_i} \lambda^2 + \frac{i2\omega}{D_{y_i}} \right)^{1/2}, \tag{3.43}$$

$$\varphi_i = B_i d_i, \qquad \kappa_{xy} = \frac{\kappa_x}{\kappa_y}, \tag{3.44}$$

where n is the layer number (with n being the bottom layer and 1 the first layer), subscript i corresponds to ith layer, subscript y corresponds to the direction perpendicular to the film/substrate interface (cross–plane) and d_i is the layer thickness. κ_{xy_i} is the effect of the thermal conductivity anisotropy, and is defined as the ratio of the in–plane κ_x to the cross–plane κ_y thermal conductivity of the layer, often approximately equal to 1 as shown experimentally [6, 12, 13]. A is a multiplying that considers the effect of heat transfer through layers of different materials. B is equivalent to the term $\sqrt{\lambda^2 + q^2(\omega)}$ in Eq. 3.32. When $i = n$, A_n depends on the boundary condition at the bottom surface of the substrate. If the substrate is finite then $A_n = \frac{-1}{\tanh(B_n d_n)}$ if the bottom surface is considered isothermal, and $A_n = -\tanh(B_n d_n)$ for an adiabatic boundary condition. If the substrate is semi–infinite, A_n= -1. The contributions of the thermal mass of the heater is neglected. In first instance, thermal boundary resistances are neglected. If needed, they can be accounted for with layers of small thicknesses.

3.2.1. Finite thickness of the substrate

Thermal diffusion length as shown in Fig. 3.2 measures how deep the thermal wave penetrates into the substrate. Thus the substrate thickness and angular frequency allow us to determine different thermal transport diffusive regimes. As a result we used Eq. 3.41 to determine the evolution of the temperature rise with respect to frequency. In order to study the temperature oscillation, we consider two different configurations. In the first designed configuration, the heater line source is located on top of a silicon substrate without considering any film layer while in the second designed configuration we consider a thin film oxide layer of thickness d_F on top of a substrate of a finite thickness d_S. The thickness of the silicon substrate is d_S = 300 µm. In our calculation, we use the dissipated power through the heater P = 19 mW for a width $2b$ = 2 µm and a length L of 256 µm. Fig. 3.9 presents the temperature evolution of the first configuration. In the static regime or when $\omega \to 0$, the temperature rise is constant as the thermal diffusion is larger than the substrate thickness. This allows us to make experimental studies at low frequency similarly to the investigation in DC measurements. In this case, we can measure the thermal conductance and deduce the thermal conductivity.

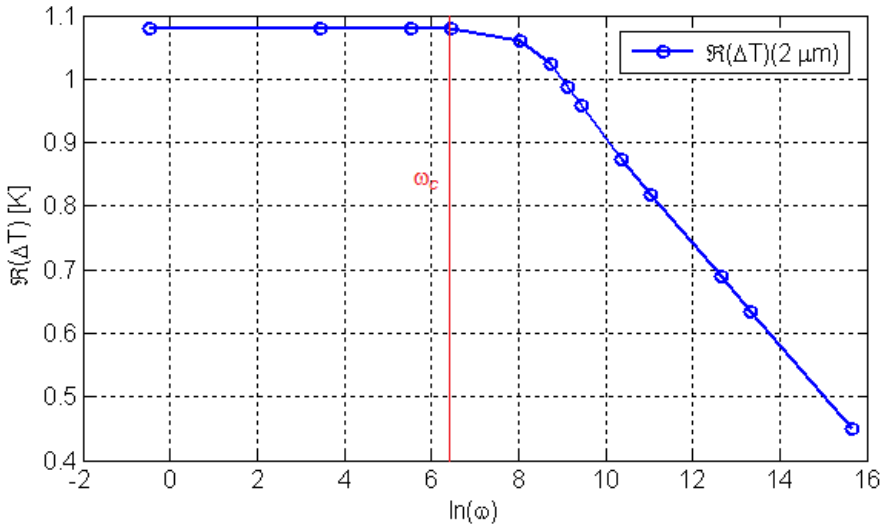

Figure 3.9. *Temperature rise as a function of angular frequency.*

1- Cut–off frequency

It can be defined as

$$d_S = \frac{1}{\Im(q)} \Longrightarrow f_c = \frac{D}{2\pi d_S^2}. \tag{3.45}$$

The value of the cut–off frequency for different materials at low frequency (5 Hz) is presented in Table 3.1. For a given low frequency (5 Hz), the thermal penetration depth is also given to provide an idea if the static temperature or the linear–regime one should be considered.

2 - Temperature level in the static regime

In the static regime, the temperature rise (see Eq. 3.41) of the heater on top of a finite substrate can be expressed as a function of the DC dissipation power (P_{DC}):

$$\Delta T = -\frac{P_{DC}}{\pi L \kappa}\left[\ln\left(\frac{d_S}{b}\right) + \beta\right], \tag{3.46}$$

where β is obtained semi–analytically and equals 1.0484. The temperature rise of the heater depends on the logarithm of the heater width and the substrate thickness. We take the first designed configuration with $\Delta T = 0$ at the bottom of the substrate and

Material	Frequency [Hz]	Thermal penetration depth [mm]	Wafer thickness [µm]	Cut-off frequency [Hz]
Silicon (Si)	5	1.69	300	77
Germanium (Ge)	5	1.06	300	31
Sapphire (Al_2O_3)	5	0.57	300	9
Alumina (Al_2O_3)	5	0.56	500	3
Crystal quartz (SiO_2)	5	0.43	300	5
Fused quartz (SiO_2)	5	0.15	300	1

Table 3.1. *Thermal penetration depths and cut–off frequencies.*

use the same dissipated electrical power per unit length for different wire widths. The temperature rise with respect to the heater size (width) is presented in Fig. 3.10. When the heater width becomes narrower, the temperature amplitude becomes higher for the same electrical power.

3.2.2. Layer–on–substrate geometry

In the second configuration, we add a thin film of oxide layer of thickness d_{SiO_2} = 15 nm on top of a finite Si substrate. The temperature drop across the film is given by the difference in the temperature rise of the same heater under the same power dissipation conditions. The film maybe described as a 1D thermal resistance in cross–plane direction when the heater width is much larger. The thermal conductivity of the oxide layer is smaller than the substrate thermal conductivity (i.e. $\kappa_F << \kappa_S$) and the thickness stays small in comparison to all other sizes, so the oxide layer can be considered as an added thermal resistance R_F:

$$R_F = \frac{d_F}{2bL\kappa_F} \qquad and \qquad \Delta T_F = \frac{P}{R_F} = \frac{P}{2bL}\frac{d_F}{\kappa_F}, \tag{3.47}$$

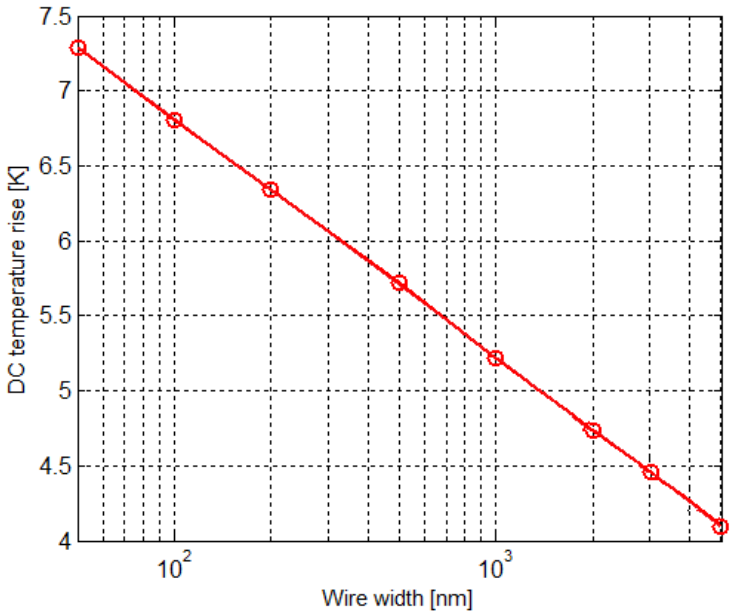

Figure 3.10. *Temperature rise as a function of heater width in the DC regime.*

which is a real value independent of frequency. As a result, the temperature rise across the thin film and the studied substrate can be expressed as [9]

$$T_{H+F} \approx \Delta T_H + \Delta T_F \tag{3.48}$$

where T_H is the heater temperature and calculated based on Eqs. 3.46 and 3.47.

Thin layer

This analysis is confirmed by the results of the full calculation as shown by Fig. 3.11, the temperature rise including the 15 nm of the oxide layer is shifted by a constant value when compared to the case without film layer. This means that adding a film increases the temperature rise of the heater without changing the behavior as a function of frequency. It is interesting to note that it is the case both in the linear regime and in the static regime.

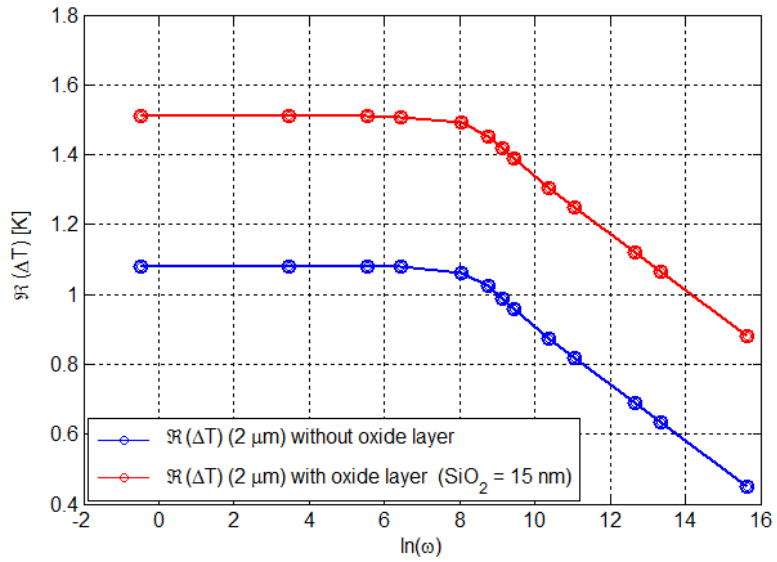

Figure 3.11. *Temperature rise as a function of angular frequency for a heater of width 2* µm.

It is interesting to analyse the thermal conductance $G_{th} = \dfrac{P}{\Delta T}$. The result obtained is shown in Fig. 3.12.

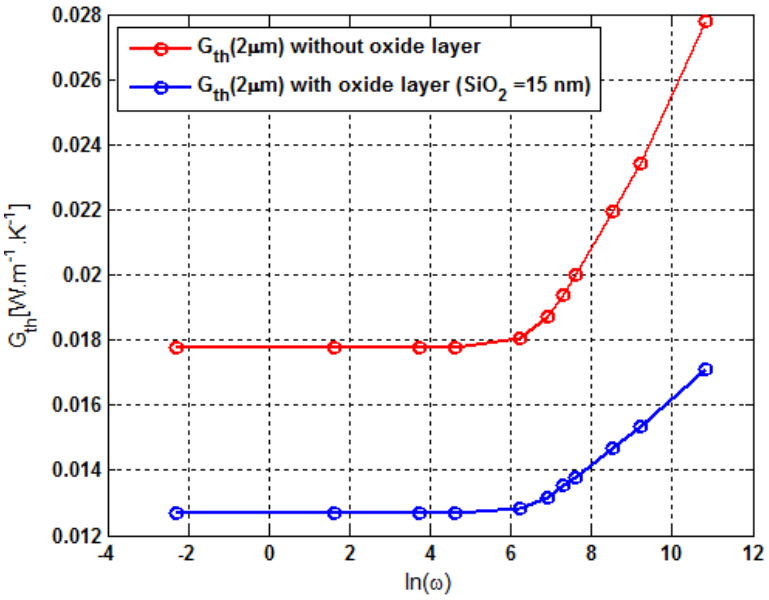

Figure 3.12. *Effect of 15 nm SiO_2 thickness on G_{th}. The heater width and length are 2* µm *and 256* µm*, respectively.*

Oxide layers affect the temperature rise of the heater. This can also be observed for the

conductance (see Fig. 3.12), but the variation is of course different from a simple shift in this case.

Thick layer

There have been many trials in the literature to analyse the heat dissipation in bilayers directly with the slope method. In Fig. 3.11, the thickness of the oxide can be neglected and the oxide only shifts the curve. Another extreme case is when the layer is very large. In Fig. 3.13, we consider a layer of 15 µm of oxide. Three regimes can be observed. Region 3 is the one where heat dissipates only in the oxide, while in Region 2 the wire temperature depends on the oxide layer and the substrate. We can observe different regimes depending on the substrate thickness and the angular frequency (see also Table 3.2). While it can be seen (here hardly due to the resistance strength of the thick oxide) that the slope changes, it is difficult to provide a value to the silicon from this analysis. We suggest to fit directly the experimental data with Eq. 3.41 in this case.

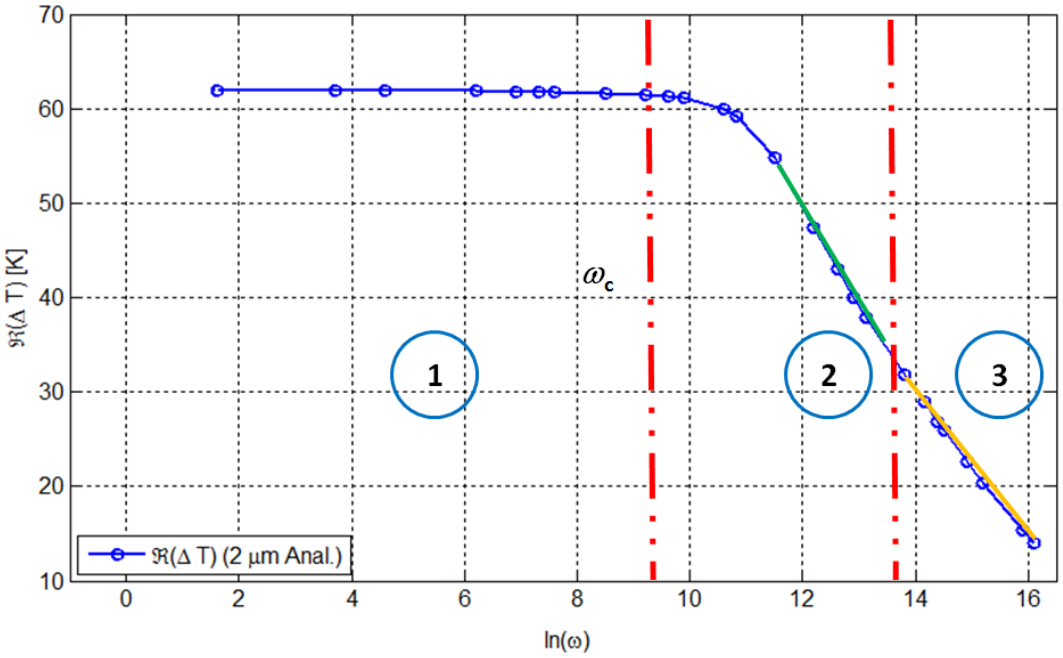

Figure 3.13. *Various regimes of heat conduction for a bilayer material.*

Regime number	Thermal spreading	Frequency range [Hz]	Regime
1	Bottom of Si substrate	[0.1 – 1066]	Static regime [12, 3]
2	Inside the Si substrate and the SiO_2 layer	[1066 – 2×10^5]	Mixed regime [6, 9]
3	Inside the SiO_2 layer	[2×10^5 – 2×10^6]	Linear regime (slope method)

Table 3.2. *Thermal spreading in the different regimes as a function of the angular frequency.*

3.2.3. Impact of wire width

The effect of two different film thicknesses with respect to different wire widths is presented in Fig. 3.14. Temperature rise is calculated in the static regime based on Eqs. 3.46 and 3.47.

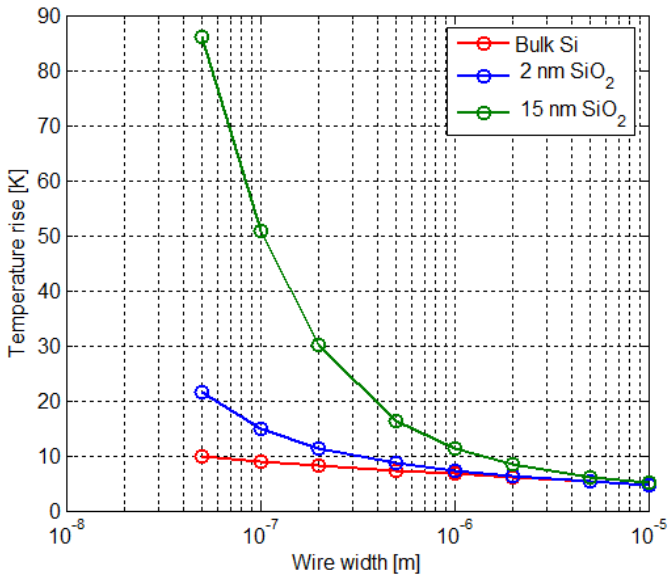

Figure 3.14. *Effect of 2 nm (blue) and 15 nm (black) of SiO_2 on temperature rise of the heater. The films are located on top of Si substrate of 300 µm thickness. The electrical heat source power is 85 mW.*

As was shown already by Figs. 3.7 and 3.11, oxide layers affect strongly the temperature rise of the heater. In Fig. 3.11, the temperature rise is increased by 50 % for a layer of 15 nm. Fig. 3.14 indicates that nanowires are affected even more strongly. Such an oxide layer would multiply the temperature rise by a factor of 5 for a wire width of 100 nm. For usual native oxide layers in the order of 2 nm, the increase for a wire of 100 nm width remains in the order of 40 %.

3.3. Numerical simulations based on finite element method

In the previous section, the results are based on several assumptions such as an infinite substrate lateral size, a metallic line heater source with negligible thickness, an insignificant coefficient of thermal exchange with air and transverse infinite size allowing to use a 2D configuration. In order to study the effect of these assumptions, we perform numerical simulations based on Finite Element Method (FEM) with a commercial package (COMSOL). It is a pure numerical method which estimates the temperature profile on the sample surface. This is done through creating a geometry, mesh and applying the boundary conditions on the substrate to be studied. Heat transfer can be approximated as two–dimensional (2D) in the plane perpendicular to the axis of the metallic heater when the length is much larger than the thermal diffusion length through the substrate. Fig. 3.15 presents a heater of finite width 2 µm over a silicon substrate of 300 µm thickness. The numerical simulation is performed in the time domain.

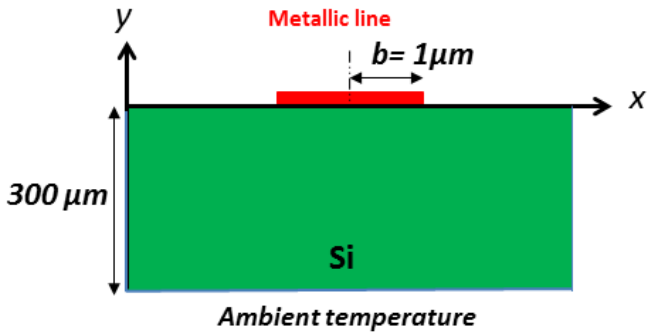

Figure 3.15. *A schematic of a 2 µm width metallic line over a 300 µm thick silicon substrate.*

We set up the parameters of the studied material silicon and the heat capacity of the heater C_P = 710 J.Kg^{-1}.K^{-1} and its density ρ = 2330 kg.m^{-3}. Heat equation in time can be expressed as

$$\rho C_P \frac{\partial T}{\partial t} = \nabla \cdot (\kappa \nabla T) + \Upsilon. \tag{3.49}$$

In 2D, it becomes

$$\rho C_P \frac{\partial T}{\partial t} = -\kappa \left(\frac{\partial^2 T}{\partial x^2} + \frac{\partial^2 T}{\partial y^2} \right) + \frac{\rho}{S^2} I^2, \tag{3.50}$$

where the last term Υ represents a volumetric electrical power that is inserted into the metallic line through Joule heating. We assume that the thermal contact between the heater and the substrate is perfect. Fig. 3.16 presents our numerical results compared to the analytical one. We can notice that there is no difference in the static and slope regimes and thus the FEM is validated by the analytical solution. We can also note some differences in the transition regime due to numerical error.

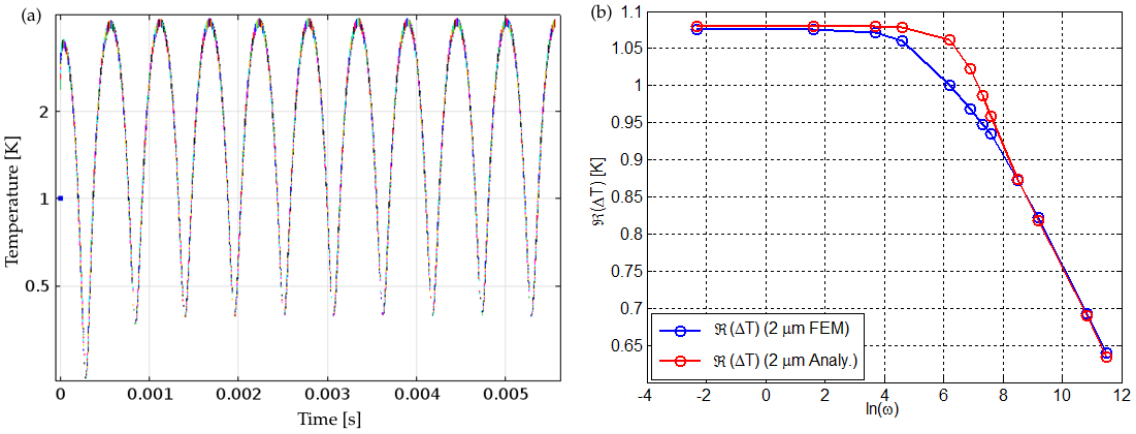

Figure 3.16. *(a) Time evolution of the wire maximal temperature. (b) Comparison of the temperature profiles between 2D numerical and analytical calculation.*

It is important to mention that we can use both studies in order to calculate the value of the thermal conductance in the static regime or to extract the thermal conductivity in the transient regime by using the slope method.

3.3.1. 2D vs 3D in the diffusive regime

To have a better understanding of our experimental results, a 3D FEM simulation was performed in addition to the 2D FEM simulation. To do so, we study numerically

the ratio of the thermal conductance G_{2D}/G_{3D} as a function of the heater length over width $L/2b$. In order to compare the 2D and 3D FEM simulations, the same boundary conditions are applied. The thermal properties and the thickness of the materials are given in Table 3.3.

Material	C [J.Kg^{-1}.K^{-1}]	κ [W.m^{-1}.K^{-1}]	D [$\times 10^{-5}$m^2.s^{-1}]	d [mm]
Silicon	710	149	8.80	0.3
Gold	129	318	12.77	1.8
Acrylic plastic	1470	0.18	0.01	3

Table 3.3. *Thermal properties and thickness of different materials at room temperature.*

When performing simulations, meshing is simply applied for 2D and 3D FEM. The number of the mesh elements is important, especially for the smallest dimension of the studied object in order to avoid numerical error. Fig. 3.17 shows the tetrahedral mesh characteristic for 2D and 3D geometries.

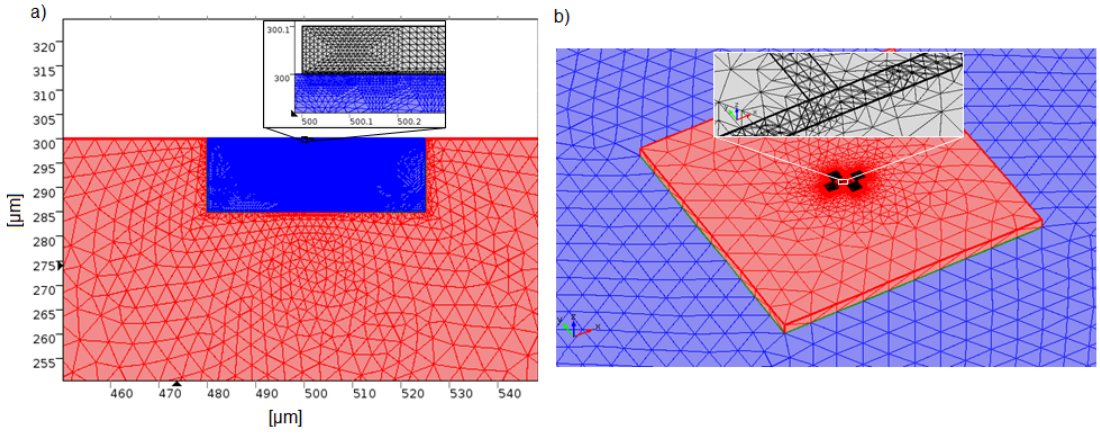

Mesh	2D FEM	3D FEM
Total number of elements	48047	1534850
Minimum element size	0.3 µm	0.1 µm

Figure 3.17. *Mesh characteristics for 2D and 3D geometry.*

Fig. 3.18 presents the temperature profile in the two FEM configurations (2D and 3D). In 2D FEM, there is only the heater of width $2b$ on top of the substrate while in 3D FEM there are the conducting pads and the volumic heater of length L, width $2b$ and thickness e.

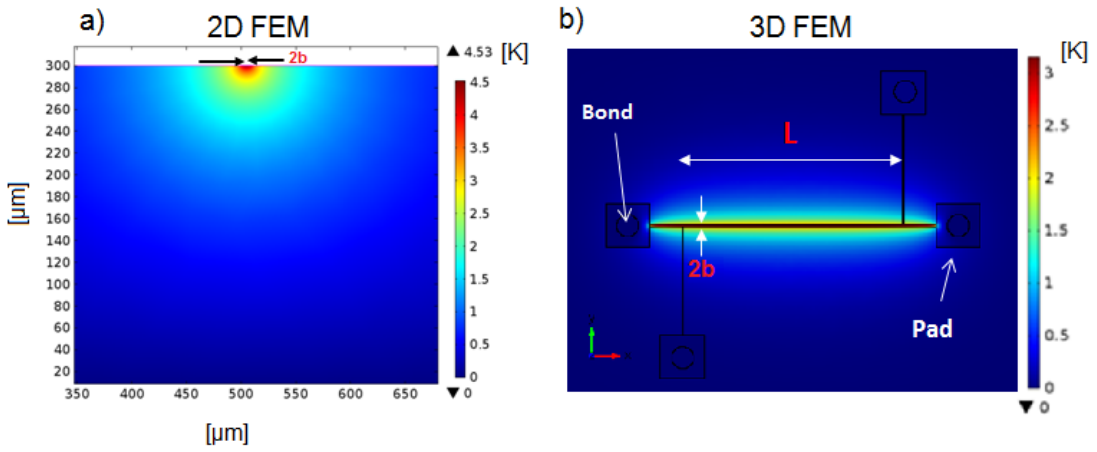

Figure 3.18. *(a) 2D and (b) top view 3D FEM–simulated profile around a Joule–heated metallic wire on top of the substrate.*

We observe that when the length of the wire is small, the temperature rise through the heater will be affected by the device pads and characteristic sizes. Therefore, long wires are required. For that, we perform a study based on two different configurations with the same boundary conditions. Fig. 3.19 compares between the two configurations. The red curve correspond to the case where, the pads are connected to the wire, but they are thermally insulating. Thus the effect that can be observed is mostly the heat dissipation in 3D in the substrate. As can be seen, when the aspect ratio is smaller than 150, the thermal conductances of the 2D and 3D geometries do not have the same value. Thus, a real experiment would be considered as 2D only when the aspect ratio is larger than 150. However to perform the measurement with such devices, the pads are required to be connected to bonding wires to perform the electrical measurements (or to probe tips that would act in the same way). Thus the impact of these bonding wires should be taken into account in 3D FEM simulations. As for the blue curve, the impact of the bonding wire on thermal conductance is represented by a boundary condition on the top of each pad involving a thermal conductance $G_{th} = \frac{\kappa S}{L}$ (with κ_{gold}) on a disc $S = \pi R^2$, with R = 50 µm and L = 1.5 cm (length of the bonding wire that conducts heat). The bonding wires are supposed to be made of gold, with thermal conductivity κ_{gold} = 318 $\mathrm{W.m^{-1}.K^{-1}}$. It is clear that the wire bonding induces a second effect, which requires further length to satisfy the 2D condition. A length to width ratio about 600 is required with the considered parameters.

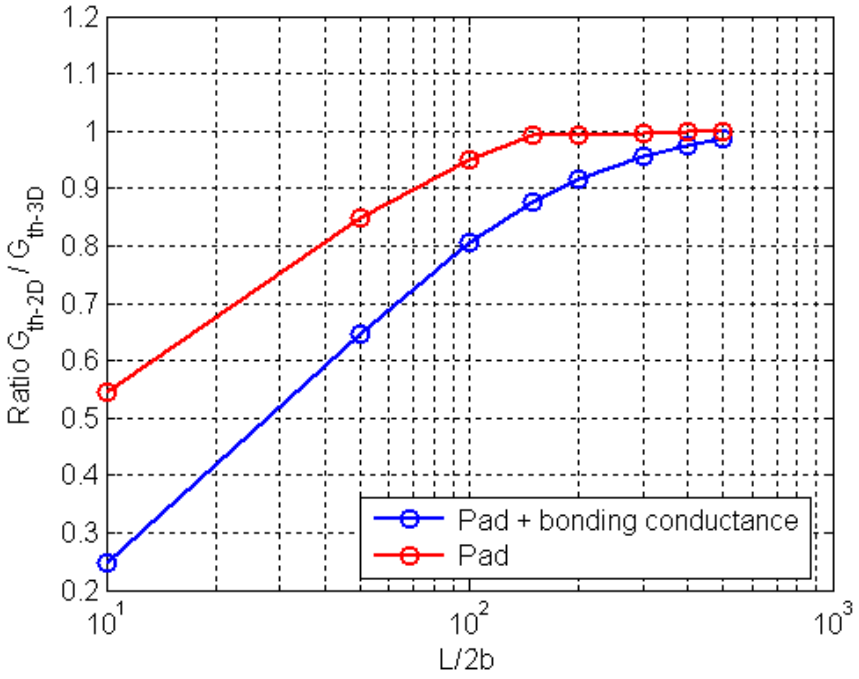

Figure 3.19. *Comparison between 2D and 3D FEM simulations. Impact of the wire parameters on the thermal conductance.*

The highlighted ratios can be difficult to meet experimentally. For instance, various devices considered in this thesis have a length of 256 microns and a width of 2 microns. In this case, full 3D simulations are required to analyze the experiments.

3.3.2. Effect of the packaging

Thermal penetration depth at low frequencies can exceed our silicon substrate thickness. For instance, at 5 Hz, heat diffusion in silicon takes place over a distance of the order of 1.69 mm (see Fig. 3.2) which is greater than the substrate thickness. As a result, interfaces and additional layers of our system can affect the evolution of the temperature oscillation. Fig. 3.20 presents the full geometry of our experimental system. The substrate of thickness 300 µm (layer 1) is placed over a printed circuit board PCB (thermal conductivity similar to acrylic plastic) of thickness 1.8 mm (layer 2) over a gold finger of thickness 3 mm (layer 3) similar to that used in our experiment (see Chapter 4).

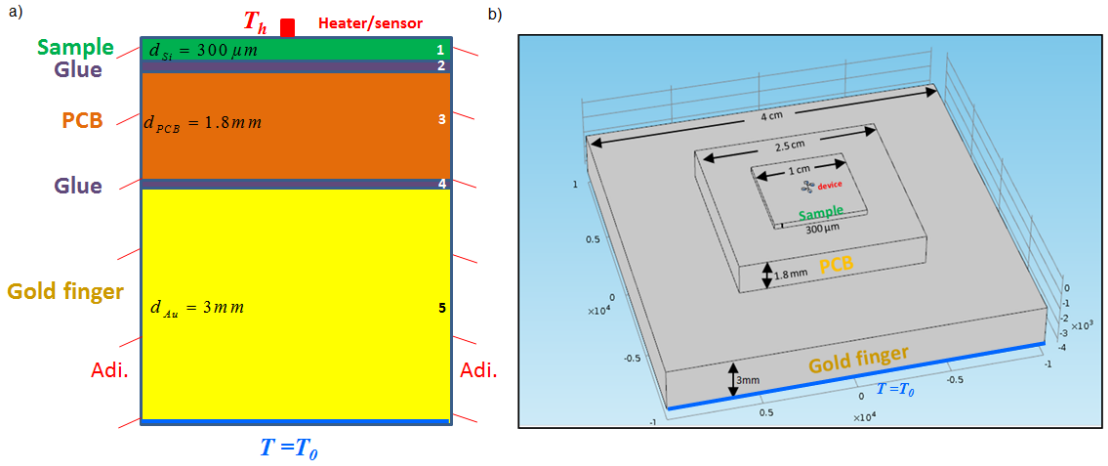

Figure 3.20. *Accounting for total geometry. (a) Schematic illustration of the multilayers of our system with the boundary conditions. (b) 3D FEM for full geometry with boundary conditions.*

In DC 2D FEM calculations, we find that the thermal conductance is 7.4 $\times 10^{-3}$W.K^{-1} while in DC 3D FEM its value is 4.6 $\times 10^{-3}$W.K^{-1}. Fig. 3.21 shows the temperature profile in the static regime with the bonding area on the pads highlighted. We find that the DC 3D thermal conductance value decreases due to the effect of bonding and becomes 3.85 $\times 10^{-3}$W.K^{-1}. This is still larger than the experimental value of 2.40 $\times 10^{-3}$W.K^{-1} obtained in AC at 5 Hz. We will see in Chapter 5 that such difference is reasonable.

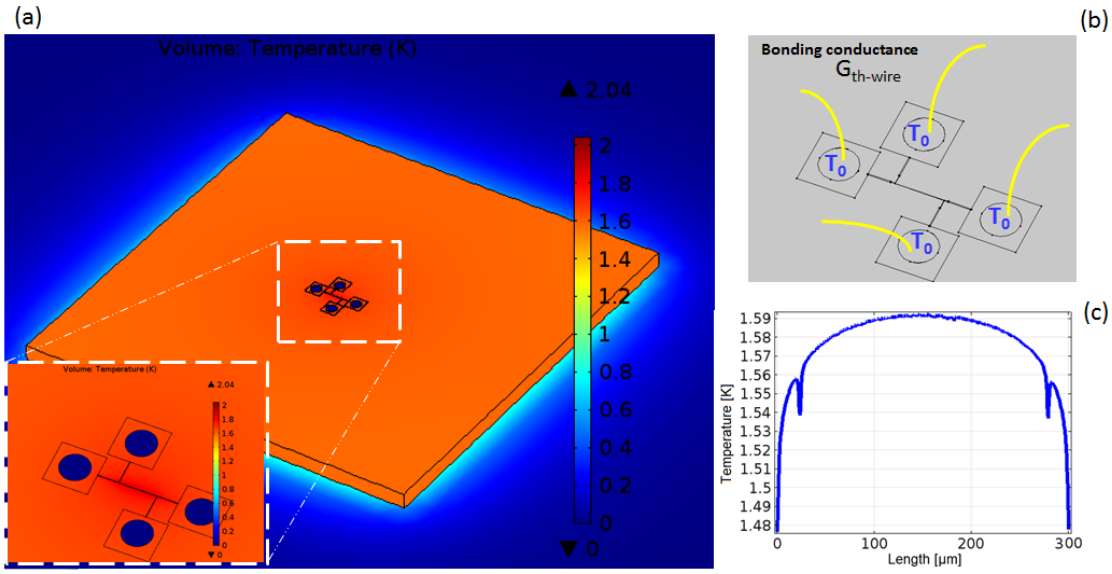

Figure 3.21. *Bonding wire and pad effect on the temperature. (a) Global view of the temperature distribution. (b) Boundary conditions (c) Temperature in the wire.*

3.3.3. 3D FEM: Impact of thermal boundary resistance

3D calculations are performed to study the effect of TBR on the thermal conductance. We consider that the TBR exists at the interface between the heat source (heater) and the studied substrate [14, 15, 16, 17, 18, 19, 20, 21, 22]. Some thermal boundary resistances at metal–metal and metal–Si interfaces are introduced in Table 3.4 [22]. In our case, TBR is considered at the interface of chromium and silicon.

Contact layer	Mixed layer thickness [nm]	TBR [$\mathrm{MW^{-1}.m^2.K}$]
Al/Cu	1	2.22×10^{-4}
Al/Si	115	2.63×10^{-3}
Cr/Si	8	3.33×10^{-3}

Table 3.4. *Thermal boundary resistance at metal–metal interfaces and metal-semiconductor interfaces.*

Fig. 3.22 shows the effect of TBR on the total thermal conductance of the studied substrate.

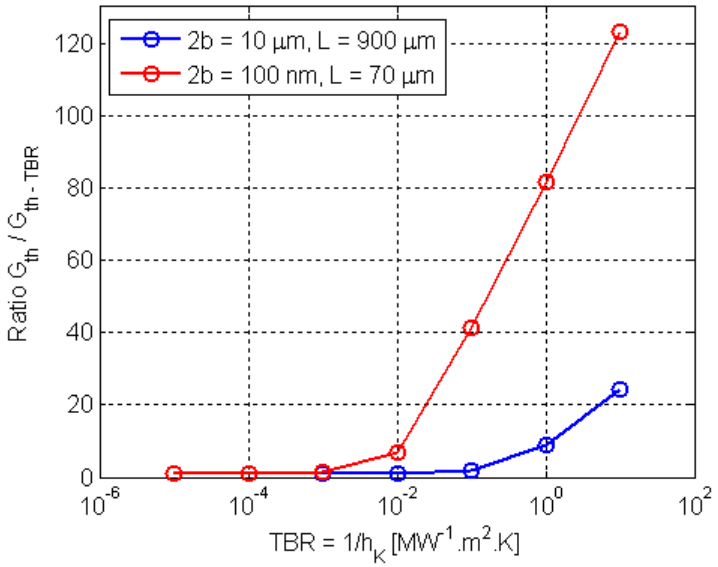

Figure 3.22. *Impact of thermal boundary resistance on thermal conductance G_{th} for a heater of widths 100 nm and 10 µm.*

For TBR < 10^{-3} $\mathrm{m^2.K.MW^{-1}}$, the ratio of thermal conductance equals one for a wire width of 100 nm. In this case, the impact of interfacial boundary resistance on thermal transport is negligible. For values larger than 10^{-3} $\mathrm{m^2.K.MW^{-1}}$, the ratio can increase

to 125 for a TBR equal to 10 $\mathrm{m}^2.\mathrm{K.MW}^{-1}$. In this case, transmissivity is very weak and interfacial boundary resistance can impact strongly the thermal transport at the interface. For a wire width of 10 µm, the effect of TBR is smaller. For TBR < 0.01 $\mathrm{m}^2.\mathrm{K.MW}^{-1}$, the ratio of thermal conductance still equals one. For values larger than 0.01 $\mathrm{m}^2.\mathrm{K.MW}^{-1}$, the ratio can increase by three orders of magnitude and thus interfacial boundary resistance can impact strongly the thermal transport at interface. The values provided by Table 3.4 discard an effect of TBR for the widths considered in Fig. 3.22 (10 µm and 100 nm). For narrower sources, the effect is stronger. The effect is parallel to the one of thin oxide layers.

3.3.4. 2D FEM: Impact of the heater thickness

DC 2D FEM was performed to study the impact of the heater thickness on the temperature at the surface of the substrate. A heater of 2 µm width and of different thicknesses (see Fig. 3.23) is created on top of the silicon substrate of the thickness of 300 µm.

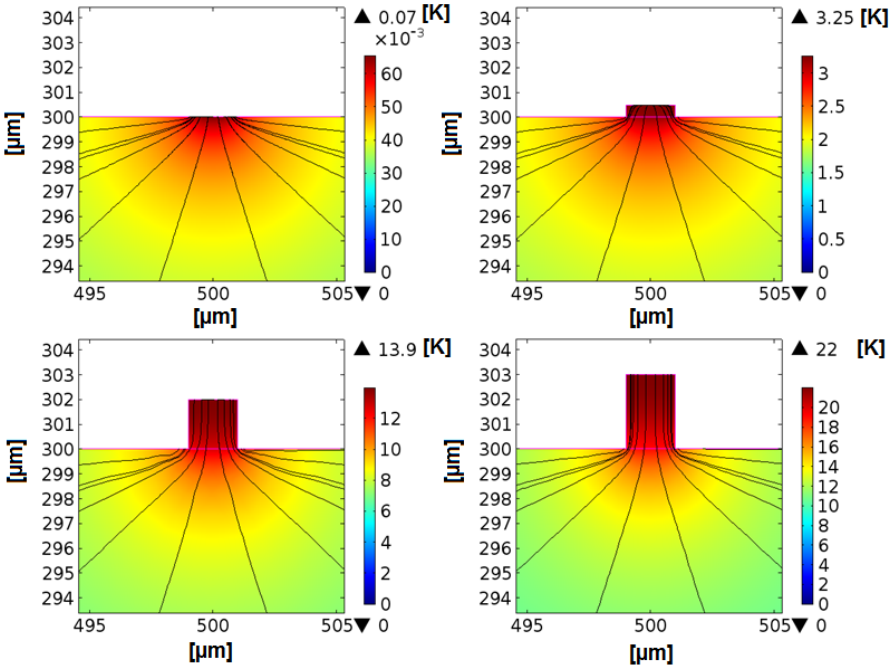

Figure 3.23. *Different heater thicknesses.*

We study the impact of the heater thickness on the thermal conductance by considering the maximum and averaging temperatures in the wire. The results are presented in Fig.

3.24.

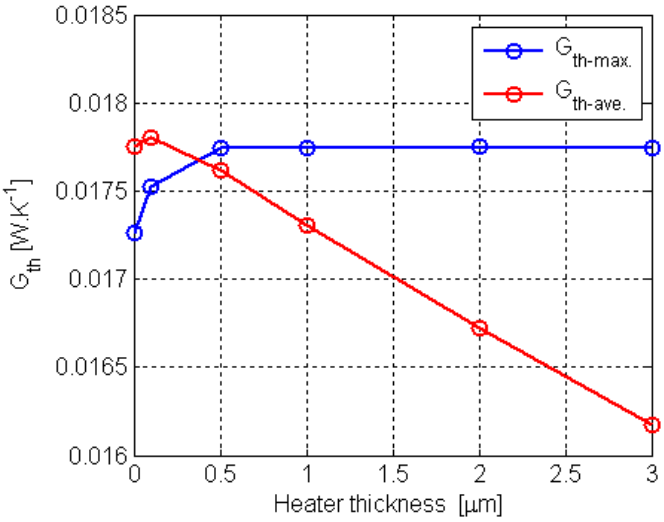

Figure 3.24. *Impact of heater thickness on thermal conductance.* G_{th} *is computed with average (red) and maximum (blue) temperatures.*

We find that heater thickness affects the maximum and average temperatures. This impact should be taken into consideration: an aspect ratio of 20 seems required for the width over the thickness. Indeed, Fig. 3.24 shows that 100 nm thickness is the maximum for a wire of 2 µm width.

3.4. Summary

In conclusion, this chapter presented analytical and numerical studies on diffusive 2D heat conduction and illustrated the difference between 2D and 3D FEM calculations. With these studies, we showed that the effect of the oxide layer on the heat dissipation becomes larger as the heat source becomes narrower. Indeed, the wire width is key to the determination of heat dissipation. We also highlighted that at low frequencies, the thermal penetration depth can be larger than the substrate thickness, and a full simulation of the geometry is then required. Heat conduction across a substrate and multilayers were studied. We detected various temperature regimes based on the substrate thickness and frequency. At high frequencies, thermal diffusion length is smaller than the substrate thickness and then the well–known linear regime can be investigated. In order to take into account the exact geometry of the heater (metallic line)

and the material under the heater, 2D vs 3D FEM calculations in diffusive regime were performed. It was found that the 3D problem can be reduced to 2D in the case where the aspect ratio of the heater ($L/2b$) is greater than 150 if the connection to the pads is not felt strongly. This value can be much larger under strong influence, for instance close to 600. Requirements on the wire were found: for instance, the ratio width over thickness should be smaller than 20 if one wants to keep it isothermal. We have seen that interfacial boundary resistance can impact thermal transport especially at nanoscale. While many points raised induce strong requirements, it may not necessarily be possible experimentally to satisfy all of them. In this case, these results can provide clues about the deviation to ideality.

References

[1] M. Beaudhuin and L. Van der Tempel, *Thermal conductivity measurement of thin layers by the 3 omega method*, (2006).

[2] D. De Koninck, *Thermal Conductivity Measurements Using the 3-Omega Technique: Application to Power Harvesting Microsystems (Thesis)*, McGill University (2008).

[3] J.-Y. Duquesne, D. Fournier and C. Frétigny, *Analytical solutions of the heat diffusion equation for 3ω method geometry*, Journal of Applied Physics **108**, 086104 (2010).

[4] N. Al-Khudary, *Material thermal conductivity measurement by the 3-omega method: application to polymers characterization using inkjet printing technology*, (2014).

[5] H. S. Carslaw and J. C. Jaeger, *Conduction of heat in solids*, Oxford: Clarendon Press, 1959, 2nd ed. (1959).

[6] D. G. Cahill, *Thermal conductivity measurement from 30 to 750 K: the 3ω method*, Review of Scientific Instruments **61**, 802 (1990).

[7] B. M. Project, A. Erdélyi and H. Bateman, *Tables of Integral Transforms: Based in Part on Notes Left by Harry Bateman and Compiled by the Staff of the Bateman Manuscript Project*, (1954).

[8] I. Moon, Y. H. Jeong and S. Kwun, *The 3ω technique for measuring dynamic specific heat and thermal conductivity of a liquid or solid*, Review of Scientific Instruments **67**, 29 (1996).

[9] S. M. Lee and D. G. Cahill, *Heat transport in thin dielectric films*, Journal of Applied Physics **81**, 2590 (1997).

[10] J. H. Kim, A. Feldman and D. Novotny, *Application of the three omega thermal conductivity measurement method to a film on a substrate of finite thickness*, Journal of Applied Physics **86**, 3959 (1999).

[11] A. Feldman, *Algorithm for solutions of the thermal diffusion equation in a stratified medium with a modulated heating source*, High Temperatures. High Pressures **31**, 293 (1999).

[12] T. Borca-Tasciuc, A. Kumar and G. Chen, *Data reduction in 3ω method for thin-film thermal conductivity determination*, Review of Scientific Instruments **72**, 2139 (2001).

[13] B. Rubinsky and M. Ikeda, *Microscale heat transfer in biological systems at low temperatures, Microscale energy transport, Ed. By Chang-Lin Tien, Arunava Majumdar, Frank M. Gerner*, (1998).

[14] K. Termentzidis, J. Parasuraman, C. A. Da Cruz, S. Merabia, D. Angelescu, F. Marty, T. Bourouina, X. Kleber, P. Chantrenne and P. Basset, *Thermal conductivity and thermal boundary resistance of nanostructures*, Nanoscale Research Letters **6**, 1 (2011).

[15] E. T. Swartz and R. O. Pohl, *Thermal boundary resistance*, Reviews of Modern Physics **61**, 605 (1989).

[16] O. Käding, H. Skurk and K. Goodson, *Thermal conduction in metallized silicon-dioxide layers on silicon*, Applied Physics Letters **65**, 1629 (1994).

[17] K. Goodson, O. Käding, M. Rösler and R. Zachai, *Experimental investigation of thermal conduction normal to diamond-silicon boundaries*, Journal of Applied Physics **77**, 1385 (1995).

[18] A. N. Smith, J. L. Hostetler and P. M. Norris, *Thermal boundary resistance measurements using a transient thermoreflectance technique*, Microscale Thermophysical Engineering **4**, 51 (2000).

[19] D. G. Cahill, K. Goodson and A. Majumdar, *Thermometry and thermal transport in micro/nanoscale solid-state devices and structures*, Journal of Heat Transfer **124**, 223 (2002).

[20] R. J. Stevens, A. N. Smith and P. M. Norris, *Measurement of thermal boundary conductance of a series of metal-dielectric interfaces by the transient thermoreflectance technique*, Journal of Heat Transfer **127**, 315 (2005).

[21] C. Cardenas, D. Fabris, S. Tokairin, F. Madriz and C. Y. Yang, *Thermoreflectance measurement of temperature and thermal resistance of thin film gold*, Journal of Heat Transfer **134**, 111401 (2012).

[22] P. E. Hopkins, *Thermal transport across solid interfaces with nanoscale imperfections: effects of roughness, disorder, dislocations, and bonding on thermal boundary conductance*, ISRN Mechanical Engineering **2013**, (2013).

CHAPTER 4

Design, fabrication and structural characterization of devices

Previous chapters are mainly devoted to the description of the basics of heat transfer and the different methods available for measuring the thermal conductivity of the materials. In this chapter, we provide a description of the fabrication process for obtaining the heater on the studied substrate. For the 3ω method, the heater must be made of a material possessing a high temperature coefficient of resistance in order to produce measurable third harmonic voltage. In general, gold (Au) is the material of choice for the heater, due to the linearity of its TCR over a wide range of temperatures, its stability and its classical deposition process. Micro-heaters are prepared either by laser lithography which requires a designed pattern or photolithography processes which requires the use of an optical mask. In addition, electrical properties of the probed materials are extremely important to perform the measurements, thus highly–resistive materials are required in order to avoid electrical leakage through the probed materials when measuring it.

In Section 4.1, materials of high MFP with their electrical properties are introduced. The design of different microdevices for the 3ω measurements is presented in Section 4.2. In Section 4.3, we present the fabrication process of the microlines based on photolithography process and laser lithography. The structural characterization of the microlines with

optical microscopy, atomic force microscpy (AFM) and scanning electron microscopy (SEM) is described in Section 4.4. The design of the nanolines is presented in Section 4.5. Finally, we perform a structural characterization of the nanolines (Section 4.6).

4.1. Probed materials and requirements

Different substrates are prepared with metallic line resistance on their surfaces. They include materials exhibiting large mean free path and high electrical resistivity. To validate the 3ω–based experimental setup, measurements are performed on these samples.

4.1.1. Selection of materials based on mean free path and type of electrothermal device

As mentioned before, wire width is key to the determination of heat dissipation. The transfer of heat through the studied substrate is involved in the use of heat sink to dissipate heat from the wire heat source. Ideally, the transfer of heat by conduction requires material of high thermal conductivity and low coefficient of thermal expansion [1]. The rate of heat dissipation from a heat source allows us to understand the thermal transport based on the phonon MFP of the studied substrate. In addition, recent studies have shown that it is possible to experimentally measure the MFP dependent contributions of phonons to thermal conductivity (phonon MFP distribution) [2, 3, 4, 5]. We have chosen different materials of high MFP (see Table 1.1). Based on the MFP and the characteristic dimension of heat source, we study the thermal transport in two different regimes. Experimentally, our measurements are performed at room temperature and then as a function of temperature. First, for microscale heat sources which are greater than the MFP of the chosen material, thermal conductivity is measured using the 3ω method. However, when the MFP is smaller than the dimension of the heater, phonons travel ballistically far from the heat source before scattering, with an effective thermal resistivity far larger than the diffusive prediction. In this case, thermal conductance is measured at room and low temperatures, but we most rely on the conductance at low frequency. In principle, this could be used to experimentally characterize the phonon MFP distribution of materials (see Fig. 1.2), similarly to what is done in optics.

4.1.2. Electrical properties of selected materials

4.1.2.1. Electrical resistivity of the substrate

In order to perform our measurements we should take into account many requirements on the electrical properties of the selected material. For instance, a low electrical resistivity of silicon substrate leads to a leakage of current through the substrate and in this case, the resistance setup on top of the substrate fails to measure the exact value of the thermal conductance of the deposited heater. Understanding the electrical resistance behaviour of the selected substrate is important for our measurement. To do so, we first study with FEM the effect of the electrical resistivity of silicon substrate on the electrical current through the heater at room temperature. We then extend the study to the temperature dependence of electrical resistivity of silicon.

3D FEM simulation is performed as follows (see Fig. 4.1). The metallic line heater is considered on top of the silicon substrate and simulated with its real volume. Applying a voltage difference between the sections S_1 and S_2 of the wire (as a model to that applied to the pads connected to these surfaces) and changing the electrical resistivity of the Si substrate, an electrical resistance can be calculated as $R = \frac{\Delta V}{I}$ where I is the electric current flowing into the boundaries of the wire and expressed as

$$I = \iint_{S_1} [\vec{J} \cdot \vec{n}] \cdot dA. \tag{4.1}$$

J is the current density in $\mathrm{A.cm^{-2}}$. Fig. 4.2 presents the impact of the substrate resistivity on the applied current for a wire length of 900 µm, a thickness of 200 nm and a width of 10 µm.

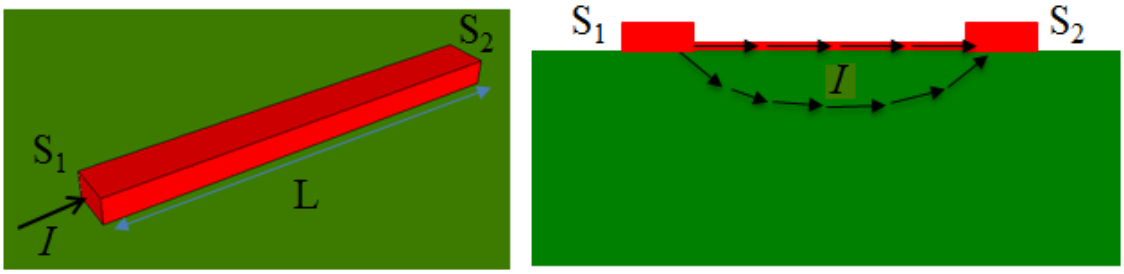

Figure 4.1. *Schematic of the cross section of a wire of sections S_1 and S_2.*

For a given applied voltage, the resistance determined will be different depending on the substrate resistance. In the case of a low electrical resistivity of Si substrate, the current calculated across section is larger. This means that an electrical leakage through the silicon substrate takes place. As we increase the electrical resistivity value of Si, the electrical leakage from the wire through the substrate becomes null. This means that a high electrical resistivity for the desired substrates is required. In the considered case (thickness e = 200 nm, width $2b$ = 10 µm, length L = 900 µm), the threshold is 2.5 $\mathrm{m\Omega.cm}$. This value depends of course of the exact shape of the wire.

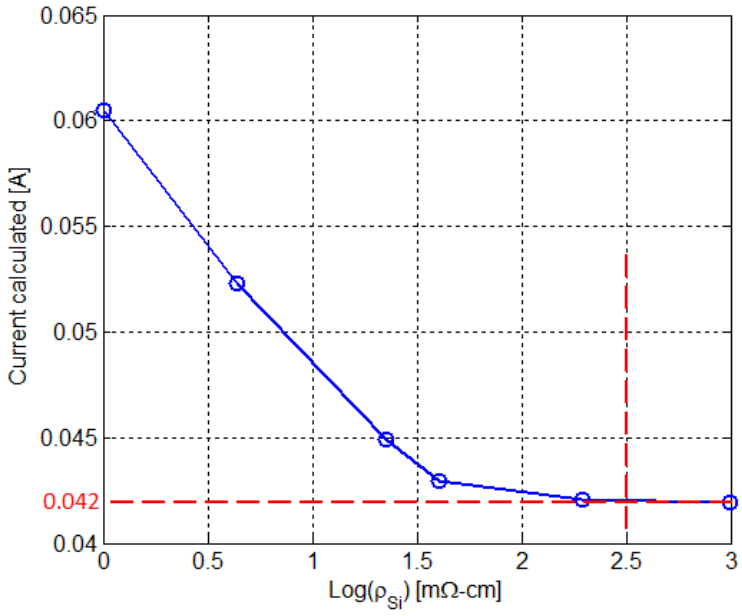

Figure 4.2. *3D FEM calculation: effect of the electrical resistivity of the Si substrate on the current density through the heater.*

4.1.2.2. Experimental determination of electrical resistivity

a) Room temperature

Various methods have been suggested to measure the electrical resistance of the silicon substrate [6, 7]. Among these methods one finds a two-probe technique for high resistive samples and four-probe techniques for single–crystal and low resistivity materials. In our case, the silicon substrate is p-type and we have chosen a four probe method as presented in Fig. 4.3. The measurement are performed at INL.

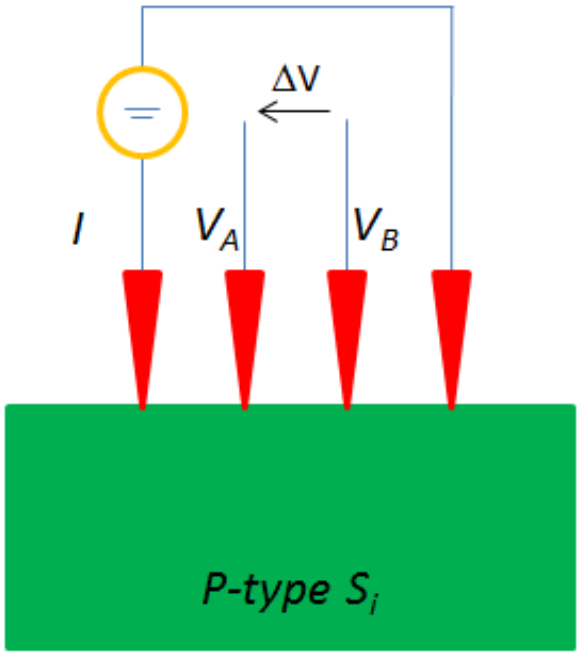

Figure 4.3. *Schematics of a four-probe method.*

Here, ΔV is the voltage drop between the two inner probes. When the sample has a finite thickness, the bulk resistivity can be replaced by the so–called sheet resistance

$$R_s = \frac{\rho_{Si}}{d_{Si}}, \tag{4.2}$$

where d_{Si} is the substrate thickness. The resistivity at room temperature is found to be ρ_{Si} = 652 Ω.cm This value is safely larger than the threshold observed in Fig. 4.2.

b) As a function of temperature

Whatever the electron path in the substrate, the electrical resistivity is proportional to the measured resistance if part of the electrons flow takes place in the substrate and that the other resistances are much smaller. We take benefit of our electrothermal measurements system to measure the resistance of the substrate as a function of temperature. Devices without lines (or with broken lines) can be therefore be used. The values are extrapolated from the measured one at room temperature. The temperature dependence of resistivity is presented in Fig. 4.4 (see also Appendix B). The resistivity increases, so the electrical

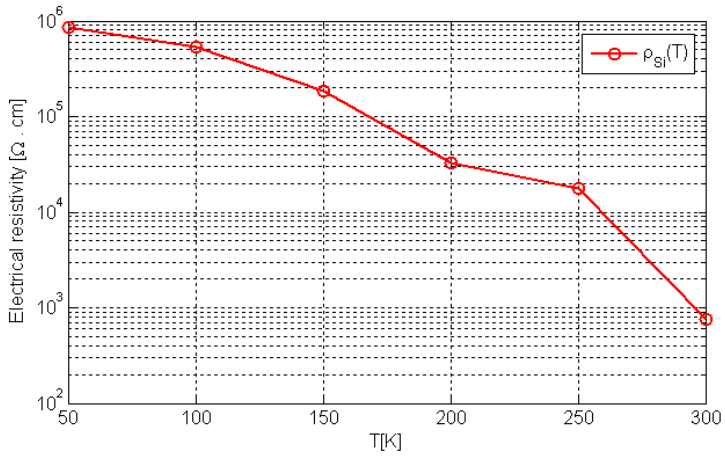

Figure 4.4. *Electrical resistivity of silicon as a function of temperature.*

leakage may be discarded even more at low temperature.

4.1.2.3. Electrical properties of the wire

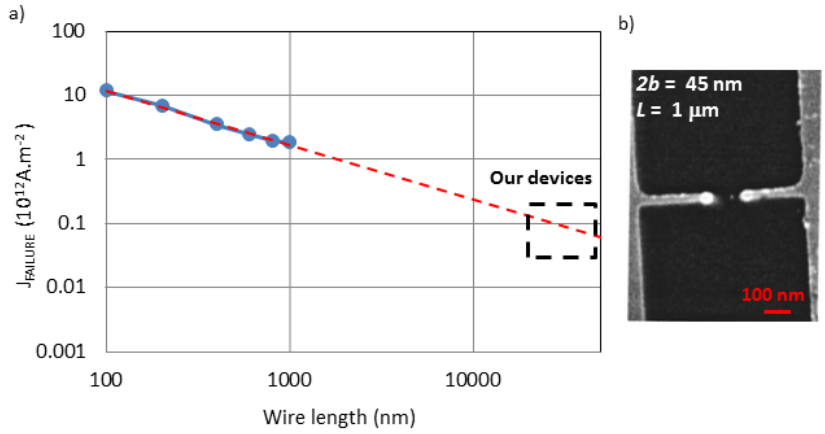

Figure 4.5. *(a) Failure current density of a nanowire. (b) Nanowire destruction [8].*

Nanowires are sensitive for the electrical measurements. Applying large current density through the wire can lead to the destruction of the wire (see Fig. 4.5 (b)). we have destroyed many nanowires, possibly due to ElectroStatic Discharges (ESD) or due to too–high current densities flowing into the wire. The authors of [8] have provided a curve which shows the threshold of failure as a function of the wire length for a given

cross-section (see Fig. 4.5(a)). The results can be used for different cross–sections by reminding that the current density is simply $J = \frac{I}{S}$. While the widths of our nanowires are in–between 20 to 200 nm, their lengths are 50 and 20 microns. The curve of [8] has been extrapolated to these lengths to determine the thresholds of failure. Note that these thresholds are maybe underestimated (see the trend close to the experimental point of the largest length), in order to be cautious. To perform success measurements, we find that the current density should be smaller than $10^{11}\mathrm{A.m}^{-2}$ in order to avoid the wire destruction.

4.2. Design of microdevices

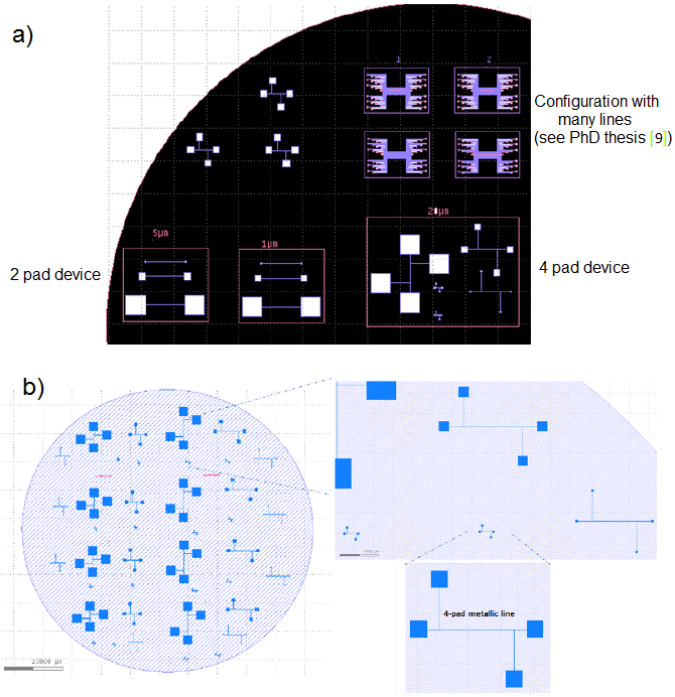

Figure 4.6. *Mask designs of different geometries. (a) A 4–inch mask of 4 pads [9] and 2 pads metallic lines. (b) 4 pad metallic lines.*

To perform our measurements, metallic lines of width $2b$ and length L are first deposited on the sample under test. The metallic lines are designed to have four contact pads. The outer pads serve in passing the current through the metallic line and at the same time the inner pads measure the voltage across them. Masks are designed with the KLayout

software with 2D sketching in units of micron and it consists of different metallic line patterns. Fig. 4.6 represents a 4–inch mask with the metallic line patterns.

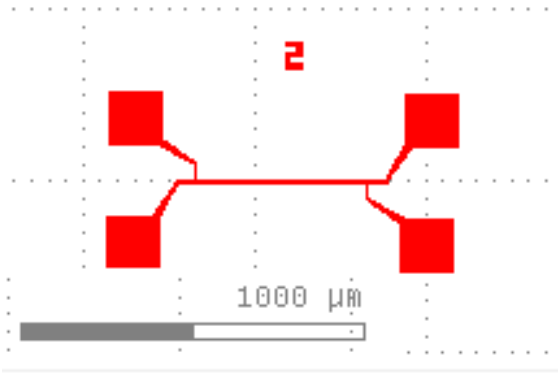

Figure 4.7. *Mask designs used with µlaser lithography.*

We have many devices on each mask but experimentally our measurements are performed on only some of them. The characteristic sizes of the devices of the designed mask in Fig. 4.6 (b) are presented in Table 4.2.

Device	Material	Length [µm]	width [µm]
1	Gold	900	1
2		1100	2
3		1500	5
4		1600	10
5		3000	20

Table 4.1. *Device parameters of Fig. 4.7 (a).*

4.3. Lithography to pattern micro and nanolines

The aim of our lithography is to deposit a microwire on top of the probed substrates. The wire widths are ranging between 10 µm and 1 µm and the length ranges from 256 µm to 3000 µm. The lithography process consists of various steps in order to fabricate the samples. To do so, a quartz mask is first designed with different patterns (see Fig. 4.6).

Substrates are prepared at Nanolyon clean room platform in INL. The thickness of each substrate is presented in Table 4.4 and metal deposition is done by evaporation.

Device	Material	Length [μm]	Width [μm]		
1	Gold	1300	2	5	10
2		500	2	5	10
3		256	2	5	10

Table 4.2. *Devices parameters of mask design in Fig. 4.7.*

4.3.1. Mask–based lithography

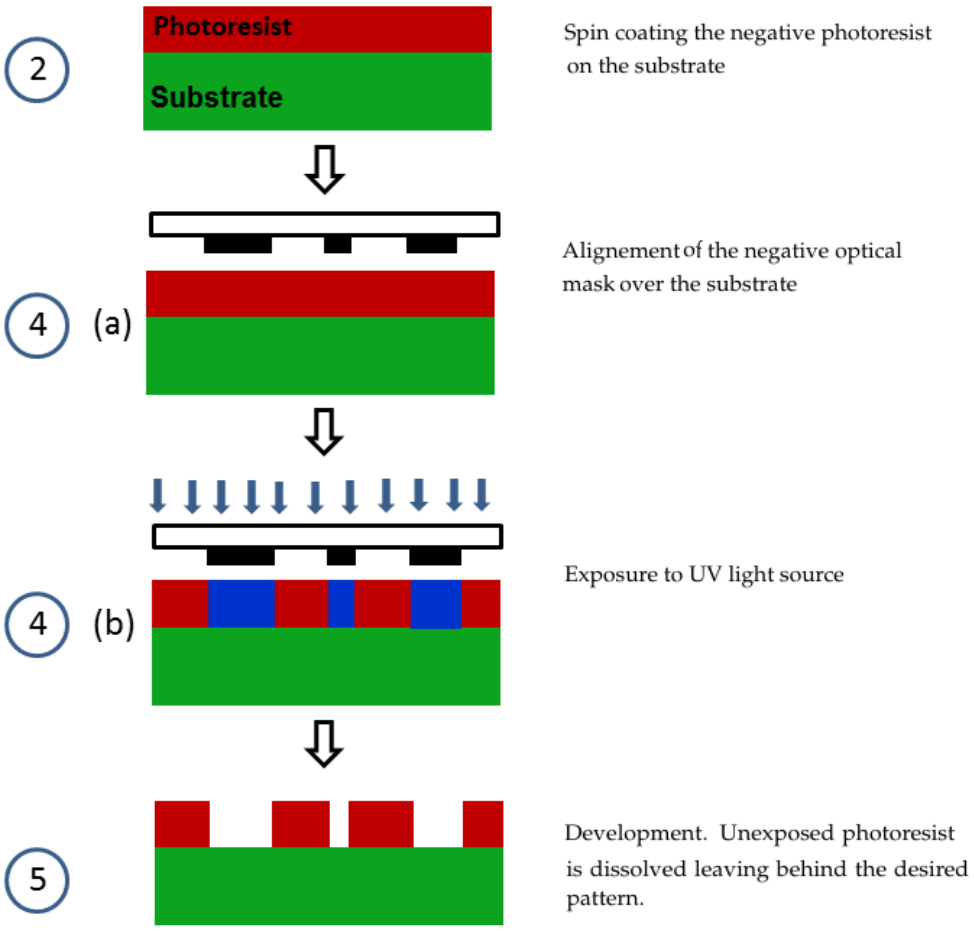

Figure 4.8. *Photolithography procedure.*

Our lithography consists of the following basic steps: wafer preparation, photoresist spin coating, baking, exposing to UltraViolet (UV) light and developing.

1. *Wafer cleaning*: This procedure is essential in order to remove the contaminants from the wafer surface. This will ensure a good adhesion of the metallic wire on top of the substrate. First, the equipments (wafer holders, tweezers, etc.) are cleaned with acetone in order to avoid the wafer contamination. The wafer is then immersed in acetone for few minutes. Thoroughly scrub the surface of the wafer with a swab, then we rinse the wafer well with ethanol. After that, a blow dry of the wafer is performed with N2 gun.

2. *Spin coating*: The process and the required film thickness determine the optimum choice of the resist. We put the wafer on the spinner and then apply suction via a vacuum pump. A negative photoresist AZ 5214 is used on the substrate, then it is placed on the spinner that rotates with 3000 rpm for 30 s. The thickness of the photoresist on the substrate is around 1.4 μm in this case.

3. *Bake*: we determine the bake temperature from the process parameters tables [90 s at about 120°C for baking]. Then, the wafer is placed on a hot plate/oven for 90 s. Finally, we let the wafer cool down during 10 to 15 minutes.

4. *Mask alignment (a) and exposure (b)*: we turn on a UV source and let it warm up for 10 minutes. First the mask is cleaned and placed in the mask cleaning holder. We rinse the quartz mask with ethanol and dry it. We place the wafer on the mask aligner and apply suction through vacuum. The mask is placed on top of the wafer and aligned in the desired direction using the assistance of an optical microscope. Then we slide the mask aligner setup to the UV source for exposure. The resist thickness that is exposed to the UV light determines how the depth profile of the absorbed light dose changes with the exposure time. The thin film is exposed for 7.8 seconds with a light intensity of the UV source of ∽15 mW/s at 440 nm wavelength. The patterns are therefore transferred into the surface of the wafer. This process is called an insulation.

5. *Development*: After exposing the resist to UV light, the sample is put in the developer AZ 726 MIF for 30 s. We use the tweezers to hang on the wafer from the developer. After that, we immerse it in water for the 1 to 3 minutes. Finally, we obtain the desired patterns on top of the substrate. The development time process is not the same for all materials. For instance, transparent materials as fused silica require 1 min instead of 30 s for silicon.
   The profilometry image (see Fig. 4.9) presents the unexposed photoresist which is dissolved while the thickness of the exposed photoresist is around 1.4 μm. The use

of profilometry helps to determine the deposition thickness and the width of the lines. Knowing of the line geometry (width and thickness of the deposited layer of photoresist) is essential for the characterization of the heater resistance.

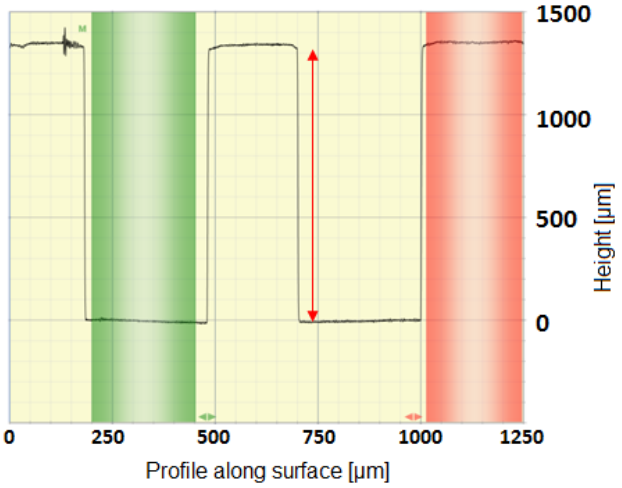

Figure 4.9. *Profilometry image after development step.*

4.3.2. Maskless lithography techniques

- **Microlaser technique**

  Microlaser technique allows to create patterns at the microscale. This is a direct writing method that does not require the use of a photomask as in the case of UV photolithography. The fabrication process is applied on different types of materials (see Table 3.1). The manufacturing process is detailed as follows:

  – Sample covering with AZ 5214 photoresist at 3000 rpm for 30 s.

  – Bake at 120°C for 90 s.

  – Sample exposure to laser beam. We note that the power of the used beam is different from one sample to another (see Table 4.3). It depends on how much the beam can penetrate through the substrate material. The filter is used to reduce the light. In addition, the time writing changes depending on the area of the pattern.

– AZ 326 MIF developer for 10 s with the silicon substrates. It needs from 20 to 30 s with transparent substrates.

Material	Filter	Laser power	Power %
Silicon (Si)	on	7 mW	60
Germanium (Ge)	on		60
Sapphire (Al_2O_3)	off		12
Alumina (Al_2O_3)	off		10
Fused quartz (SiO_2)	off		10

Table 4.3. *Laser power for different materials*

- **Electron beam lithography**

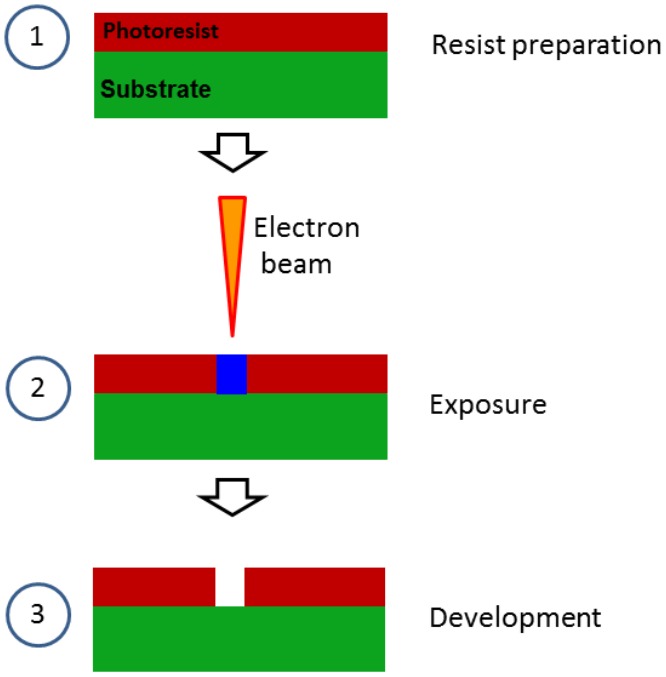

Figure 4.10. *Illustration of the steps involved in the EBL process.*

Electron beam lithography (EBL) is a technique that allows us to create patterns at the nanoscale. EBL allows to write submicronic features by the scanning of a focused energetic beam of electrons (e–beam) on a photoresist. The technique has the same process as laser lithography but the exposure is done using e-beam instead of light beam (see Fig. 4.10). The e–beam interacts with the photoresist depending on wether

the photoresist is negative or positive. In our case, the chosen photoresist is negative. The devices were manufactured in the frame of LN2 laboratory by Dr Céline Chevalier (now at INL) and then within the Nanolyon platform by Pierre Cremillieu. The negative photoresist preserves the areas of the photoresist traced by the e–beam source and dissolves all surrounding area that are not in contact with the e-beam during the pattern–writing process.

4.3.3. Metal deposition and lift-off

Metals are deposited by metal evaporation technique in high vacuum (see Fig. 4.11). Deposition of metal layers in the case of the microwires was performed in an Edwards FL400 electron-beam evaporator.

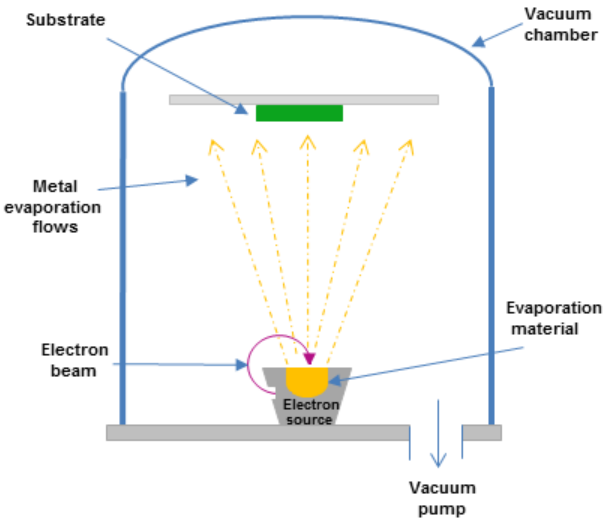

Figure 4.11. *Metal evaporation principle.*

The parameters considered during the deposition are presented in Table 4.4.

Metal	Cr	Au
Intensity [mA]	92	160
Evaporation rate [nm.s^{-1}]	0.1	0.2
Vacuum level [mbar]	8×10^{-7}	6×10^{-7}
Target thickness [nm]	5	100

Table 4.4. *Thin film deposition parameters*

We deposit two types of metallic materials with different thicknesses.

1. A layer of 5 nm of chromium (Cr) to promote the adhesion of the gold microline on the substrate.

2. A layer of 100 nm of gold that serves as the heater and thermometer.

   In lift-off processes, the photoresist is first deposited and patterned on the substrate. The material of interest is then deposited on top and the photoresist is subsequently removed, leaving behind only the material deposited directly on the substrate (see Fig. 4.12 (a)). These processes are useful for patterning materials that cannot be etched without affecting underlying materials on the substrate. The samples immersed in acetone with the help of an ultrasonic bath, then the four pads device is ready for the measurements as presented in Fig. 4.12 (b).

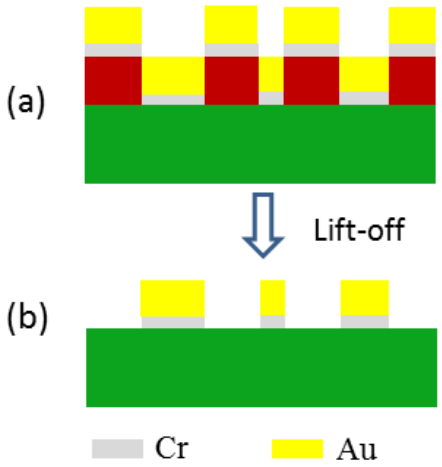

Figure 4.12. *(a) Gold and chromium deposition by evaporation after lithography process, (b) metallic patterns deposited on the surface of the substrate.*

An important aspect of metal evaporation is the slow deposition rate (typically less than 1000 nm per hour), which allows the films to grow optimally. Fig. 4.13 represents a top view of a device on top of the substrate after the lift–off process. In the case of the nanolines, the metal evaporation process may have been slightly different. In particular, the deposited thicknesses were smaller as there is a minimum aspect ratio of thickness over width that should be respected.

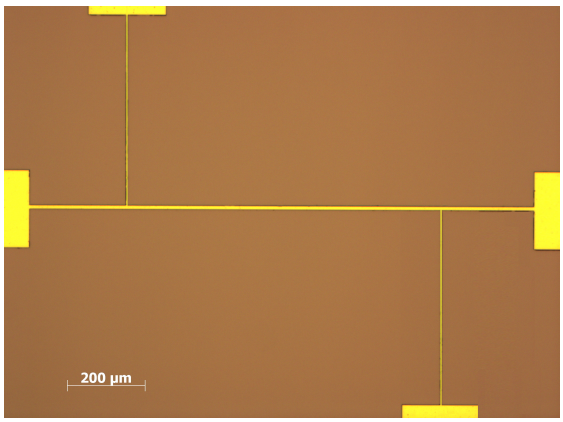

Figure 4.13. *Deposited metallic wires.*

4.4. Caracterization of the microlines

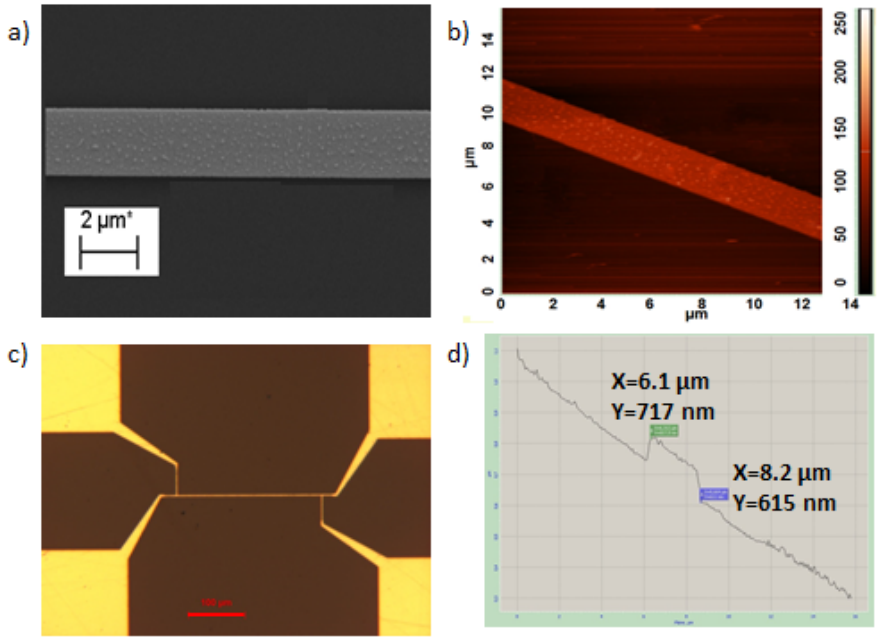

Figure 4.14. *Microline characterization: (a) SEM image of the wire, (b) AFM image of a gold wire, (c) optical microscopy image of the wire, (d) thickness and width profile of the wire obtained by profilometry.*

To determinate the temperature of the heater resistor deposited one requires a knowledge of the resistor's characteristics, i.e. of the gold thin film such as the structure grains,

thickness of the heater, etc. The characterization is achieved by scanning electron microscopy (SEM), atomic force microscopy (AFM) and optical microscopy.

1. *Characterization with SEM*

   The surface of the gold wires was observed with SEM as shown in Fig. 4.14 (a). It showed small grains on the top of the wire attributed to the polycrystalline state of the wire.

2. *Characterization with AFM*

   Our microdevices can range between 10 µm and 2 µm, we chose the device of 2 µm width to highlight the characterization results. Fig. 4.14 (b) represents the 2D AFM image and some grains can also be seen on top of the wire.

3. *Observation with optical microscopy*

   Fig. 4.14 (c) shows an optical microscopy image of our device. We use optical image to check if there are problems on the central wire of the device or on the four–pad connections: a single problem with the wire shape can lead to large measurement error.

4.5. Design of nanolines

As mentioned in the first chapter, the MFP of silicon is 300 nm. In order to study the thermal transport in the ballistic regime, wire widths smaller than 300 nm are required. A four probe electrical technique similar to the 3ω method is used to measure the thermal conductance of the material in the ballistic regime. To do so, various nanodevices designs of different lengths and widths have been prepared with the KLayout software as presented in Fig. 4.15.

The parameters of these nanodevices are presented in Table 4.5.

Length [µm]	Width [nm]				Thickness [nm]			
20	20	50	100	200	40	40	60	100
50								

Table 4.5. *Characteristic sizes of the nanolines.*

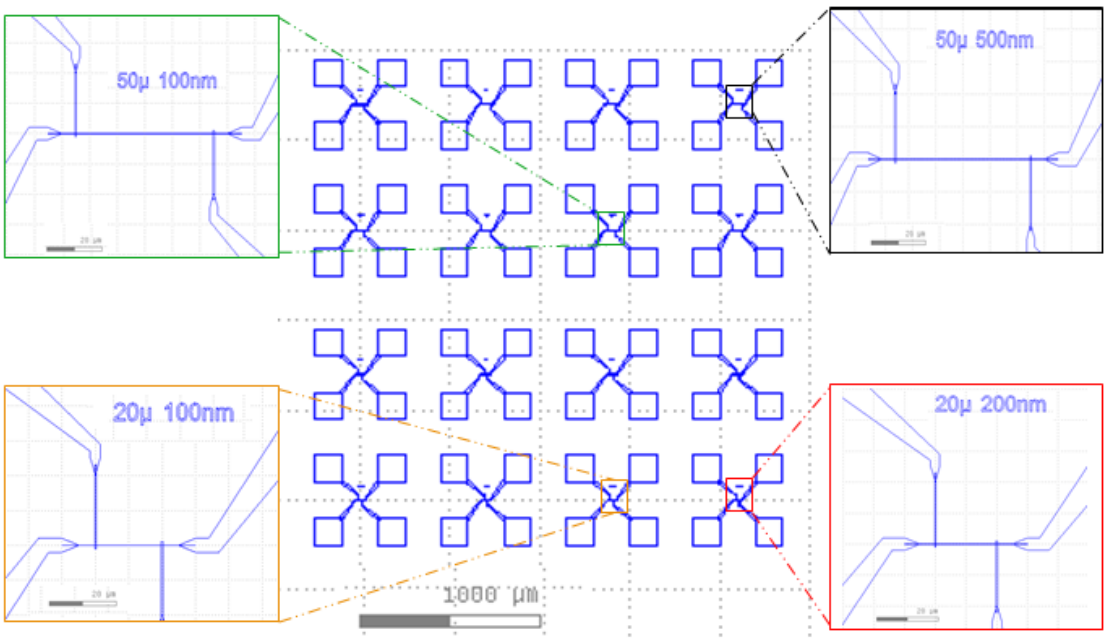

Figure 4.15. *Nanoline designs.*

4.6. Structural characterization of nanolines

As the device size decreases, grain size, thickness of the heater and its structure become extremely important. Devices are characterized by SEM and AFM. Fig. 4.16 (a) presents SEM images of different nanowires of different lengths and widths.

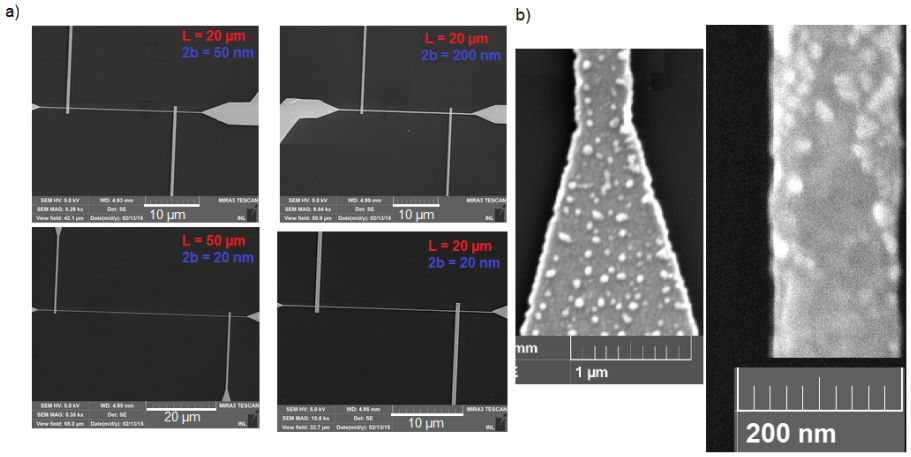

Figure 4.16. *SEM images: (a) different wire widths and lengths. (b) Silicon grains in the heater*

In order to determine the characteristic sizes of the wire (width and thickness), AFM is implemented (see Fig. 4.17). It can be seen that the thickness of the wire is 60 nm as specified and the width is about 100 nm while the borders of the wire are sharp in the peak and wide in the bottom. In this example, it is a bit difficult to disentangle the effect of the AFM tip from the one of the metallic wire. However, if the surface of the wire in contact with the substrate is broader than expected, this should be taken into account in the data treatment once the thermal conductance is determined. Note that the shape of the wires is also checked experimentally by a simple analysis of their electrical resistance, which is $\rho L/S$ (see Chapter 5) in principle.

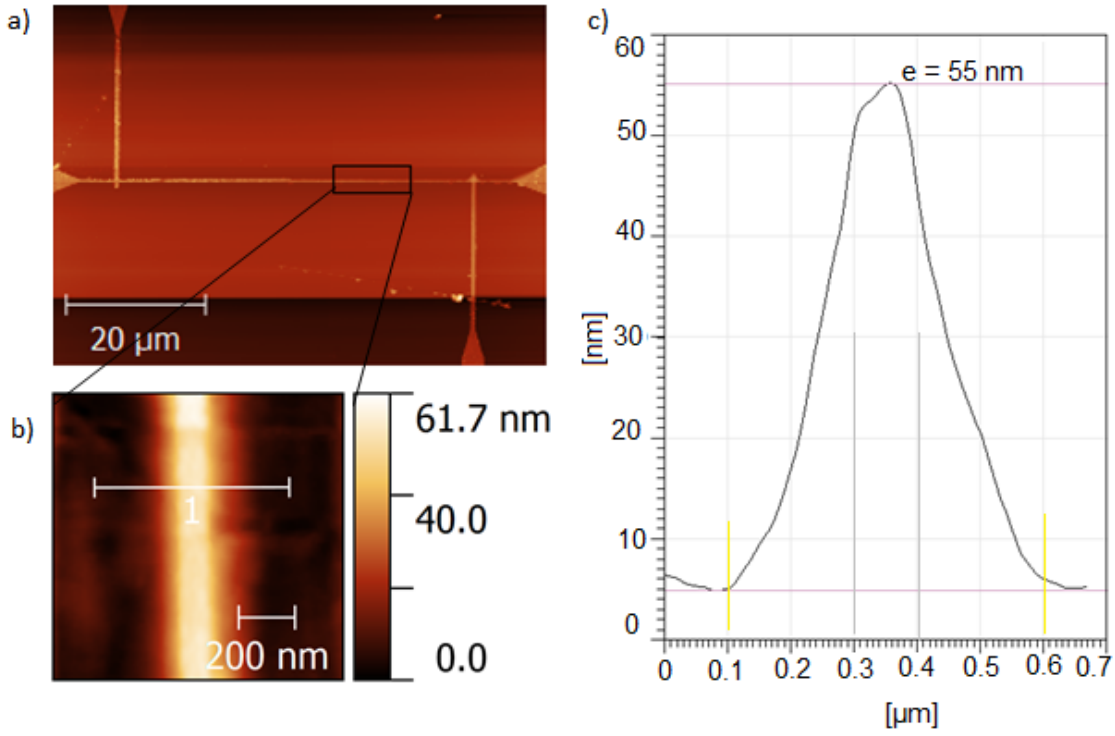

Figure 4.17. *(a) AFM images of a device of length 50 µm and width 100 nm, (b) zoom on the central part of the nanowire, (c) thickness, width and shape of the wire are determined.*

Fig. 4.18 shows AFM images of a device of length 20 µm and width 500 nm. The thickness of the heater is 100 nm (see Fig. 4.18 (c)) while see Fig. 4.18 (b) shows grain sizes on the heater.

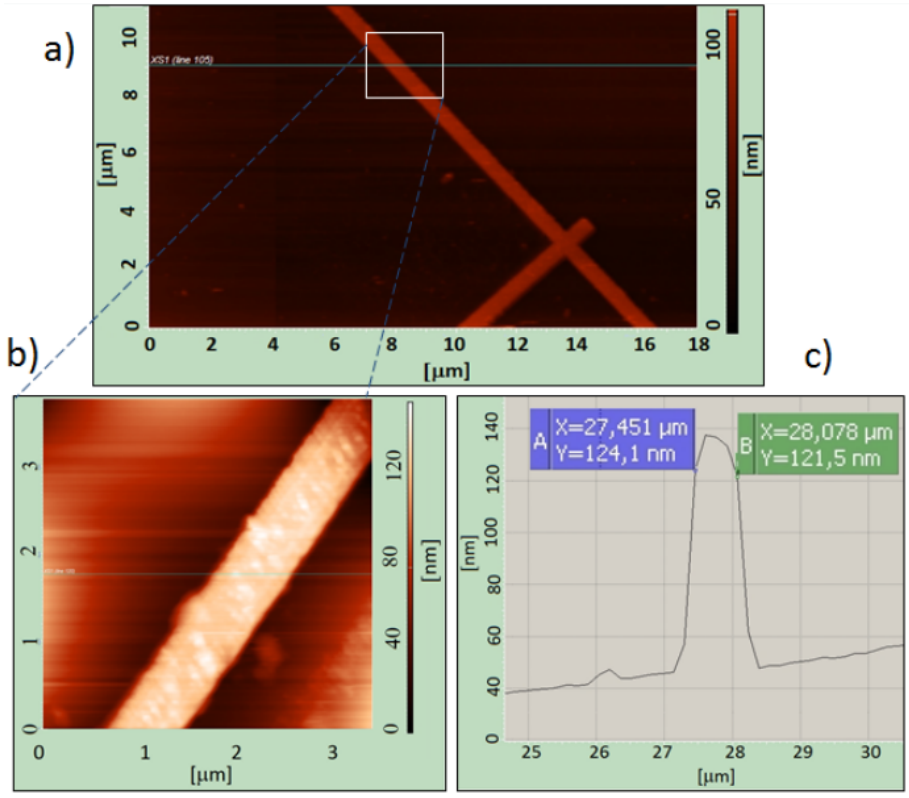

Figure 4.18. *(a) AFM images of a device of length 20 µm and width 500 nm, (b) zoom on the central part of the nanowire, (c) thickness, width and shape of the wire are determined.*

4.7. Summary

This chapter presented the design, fabrication and characterization of the micro/nanolines. Metallic microlines of different widths and lengths and about 100 nm thick were prepared by photolithography and µlaser lithography. Patterns of the required devices were prepared. Nanolines were prepared by electron beam lithography (EBL). Materials are required to have high electrical resistivity to avoid electrical leakage through the material. The temperature dependence of silicon resistivity is analyzed. Experimentally, we found that the electrical resistivity of silicon increases as the temperature is decreased. The results obtained allow performing the measurements on our substrates. Finally, devices are structurally characterized by AFM, SEM and optical microscopy. All these steps will facilitate performing the thermal measurements in the selected devices.

References

[1] D. Chung, *Materials for thermal conduction*, Applied Thermal Engineering **21**, 1593 (2001).

[2] K. T. Regner, D. P. Sellan, Z. Su, C. H. Amon, A. J. McGaughey and J. A. Malen, *Broadband phonon mean free path contributions to thermal conductivity measured using frequency domain thermoreflectance*, Nature communications **4**, 1640 (2013).

[3] A. J. Minnich, J. Johnson, A. Schmidt, K. Esfarjani, M. Dresselhaus, K. A. Nelson and G. Chen, *Thermal conductivity spectroscopy technique to measure phonon mean free paths*, Physical Review Letters **107**, 095901 (2011).

[4] J. A. Johnson, A. Maznev, J. Cuffe, J. K. Eliason, A. J. Minnich, T. Kehoe, C. M. S. Torres, G. Chen and K. A. Nelson, *Direct measurement of room-temperature nondiffusive thermal transport over micron distances in a silicon membrane*, Physical Review Letters **110**, 025901 (2013).

[5] A. Minnich, *Determining phonon mean free paths from observations of quasiballistic thermal transport*, Physical Review Letters **109**, 205901 (2012).

[6] L. B. Valdes, *Resistivity measurements on germanium for transistors*, Proceedings of the IRE **42**, 420 (1954).

[7] I. Miccoli, F. Edler, H. Pfnür and C. Tegenkamp, *The 100th anniversary of the four-point probe technique: the role of probe geometries in isotropic and anisotropic systems*, Journal of Physics: Condensed Matter **27**, 223201 (2015).

[8] C. Durkan and M. Welland, *Analysis of failure mechanisms in electrically stressed gold nanowires*, Ultramicroscopy **82**, 125 (2000).

[9] A. Assy, *Development of two techniques for thermal characterization of materials: Scanning Thermal Microscopy (SThM) and 2ω method*, (2015).

CHAPTER 5

Experimental results with microlines

This chapter is dedicated to the experimental setup and the measurement implementation at our laboratory. In Section 5.1, the experimental setup that includes the connection from the chip to device and the electrical setup with the cryostat–based measurement are introduced. The metallic line must be made of a material possessing a high temperature coefficient of resistance in order to produce measurable third harmonic voltages, thus Section 5.2 introduces the TCR measurements while the experimental results are compared to the theory. Thermal conductivities of different materials and the impact of the oxide layer on the temperature rise are introduced in Section 5.3.

5.1. Experimental setup

In this section, we describe the details of the experimental procedure used to perform the measurements. Fig. 5.1 shows our experimental room.

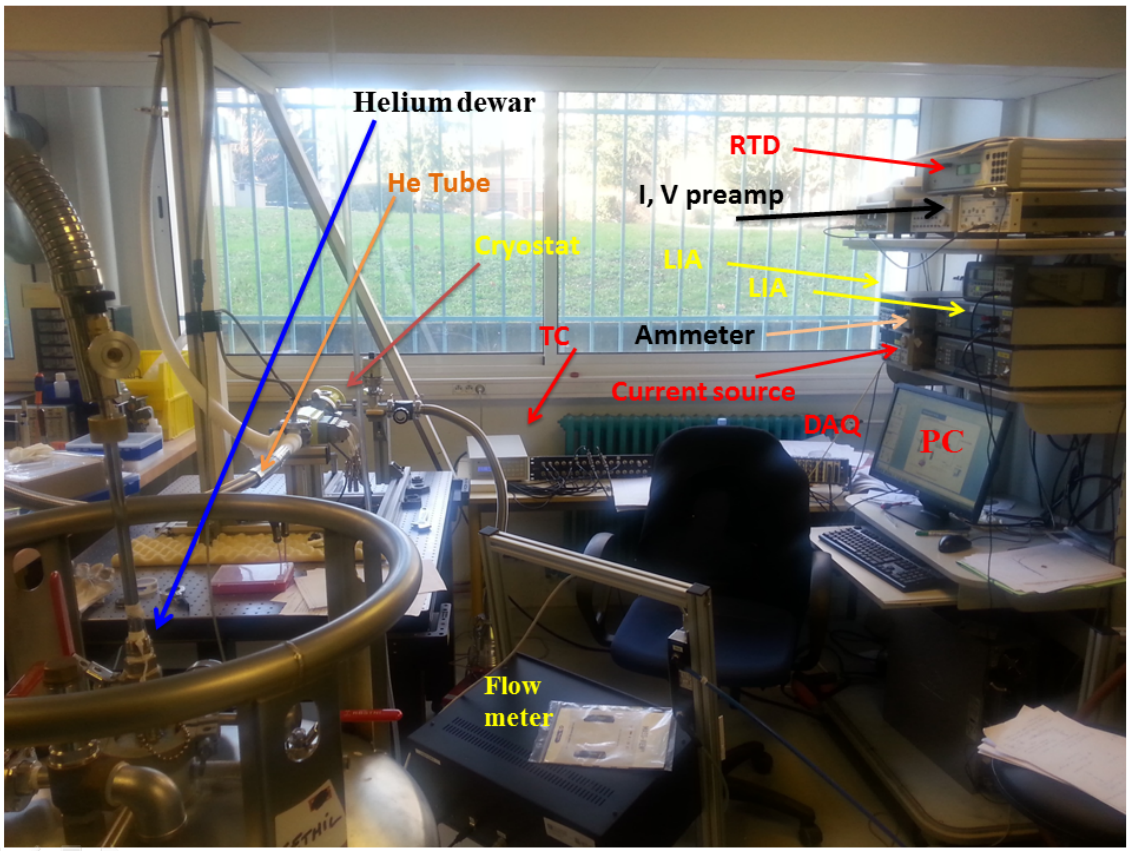

Figure 5.1. *General view of the experimental setup developed.*

5.1.1. Connection from the chip to device (bonding)

Ball bonding is a type of wire bonding [1, 2, 3], required to connect the electrical interconnections between a chip carrier and our fabricated device. The diameter of the bonding wire is 65 µm for micron devices and 25 µm for the nanodevices. The pad size of the microdevices is 200 µm × 200 µm while for the nanodevices it is 100 µm × 100 µm. Our chip carrier is a printed circuit board (PCB) surrounded by a number of contact pads linked to metal pins. Devices are bonded to chip carrier and then wires are bonded between the contact pads linked to PCB and the device pads (see Fig. 5.2).

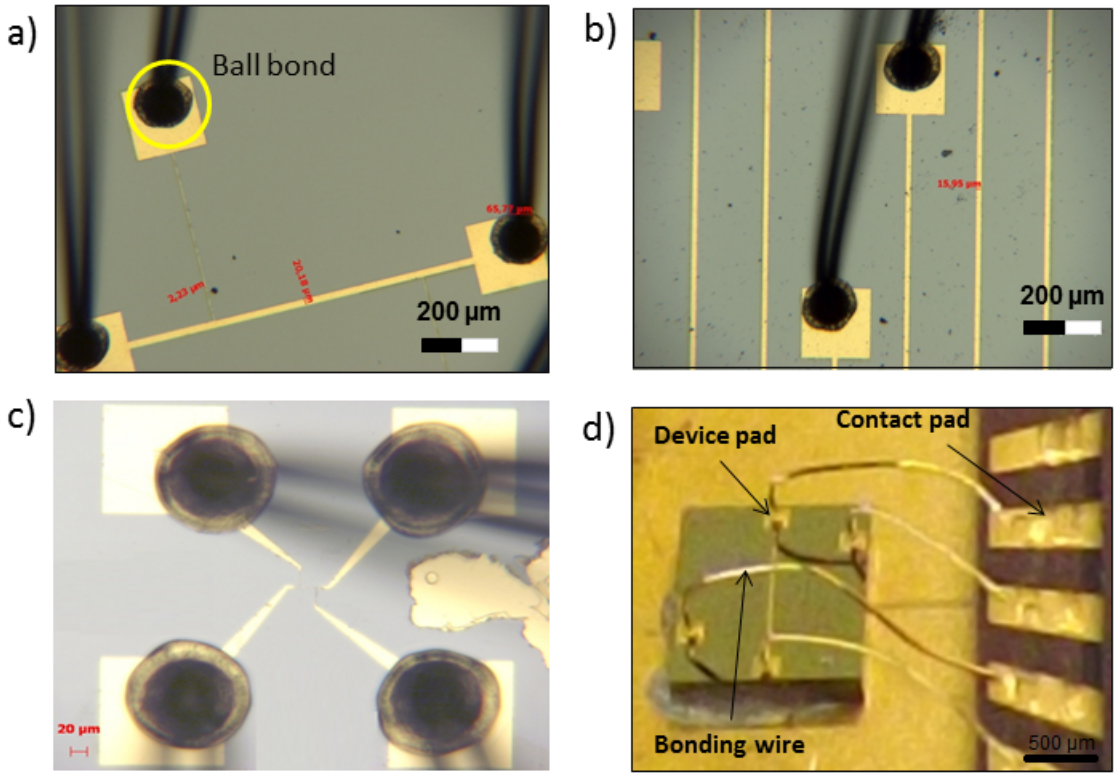

Figure 5.2. *Optical images illustrating the connection and wire bonding process. (a) and (b) Ball bonding on the pads of the microdevices, (c) Ball bonding on the pads of nanodevices. (d) Bonding wires achieve the contact between the device pad and the contact pads of the chip carrier.*

These operations have been performed by Pascal Bevilacqua at AMPERE laboratory and by Irène Peck from CIME in Grenoble.

5.1.2. Cryostat-based measurement

After the micro-bonding, the sample is connected to the holder which is mounted inside a cryostat, closed, pumped and connected, ready to measurements. Cryostats ensure operation within a large range of temperatures, from liquid helium one to 400 K in our case. In practice the cooling process in the cryostat is presented in Fig. 5.3.

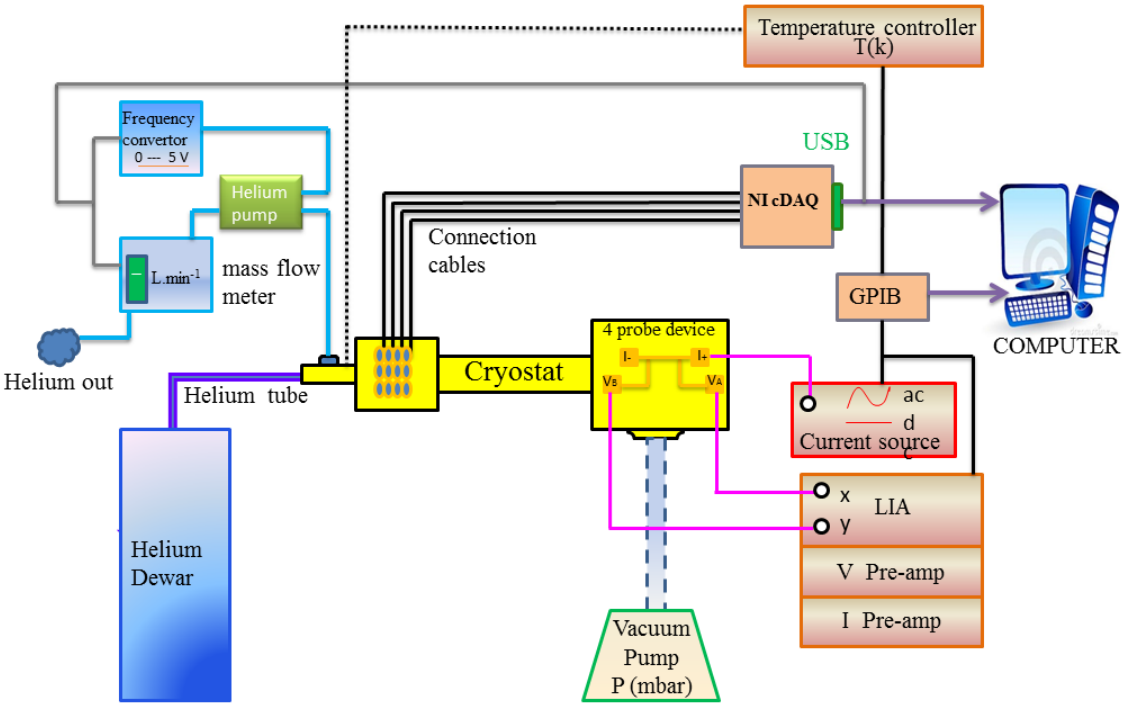

Figure 5.3. *Cryostat-based measurement setup.*

Our cryostat "Cryoscan" is designed especially for our measurements. It is composed of 20 electrical connections allowing us to probe many samples located on the gold finger (see Fig. 5.4 for the two types of device holder that we used) in the same time.

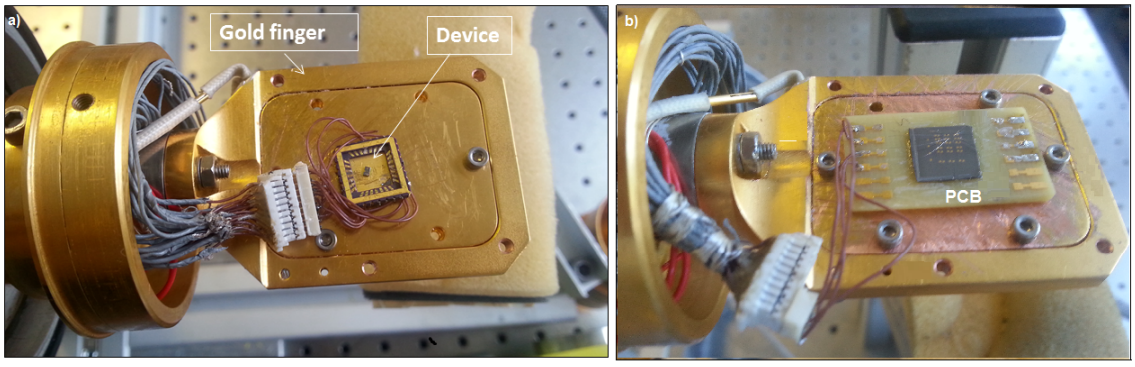

Figure 5.4. *Device glued on: (a) a chip carrier, (b) a PCB set on the gold finger.*

Our measurement starts from room temperature and is managed through a temperature controller connected to a diode sensor. The temperature step is set usually 20 K. The time between two measurements is set to 90 min, following thermalization waiting time

that is usually observed (see Fig. 5.5). To control the temperature inside the cryostat, we use a mass flowmeter and the temperature controller with the help of PID feedback loops allowing stabilizing faster the temperature of the diode sensor.

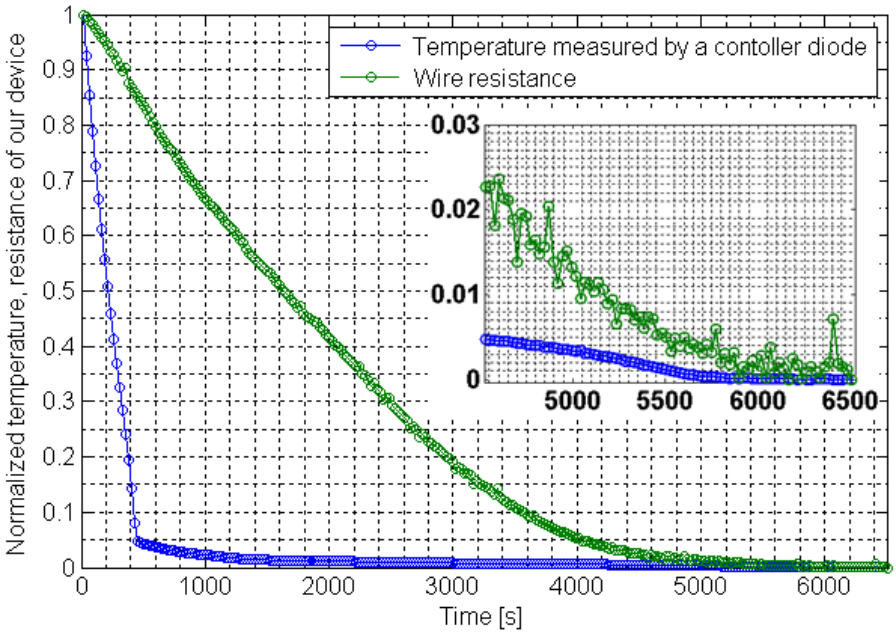

Figure 5.5. *Measurement of the thermalization time: diode sensor temperature and normalized wire resistance as a function of time.*

We can use different PID values depending the the flow rate value set by the flowmeter. In our experiments we used two PID loops (values [500, 250, 0], [500, 150, 0]), while the flow rate values are in the range of [0–5] L/min. Fig. 5.5 shows that the thermalization time of the actual device (green curve) is much longer than that of the diode close to the heater on which the feedback loop is applied (blue curve). We apply a criterion of 1% error. As a result, an experiment as a function of temperature can result in a duration of a full day or more. The relation between the flow rate and the thermalization time is given in Fig. 5.6. It can be noticed that a high flow rate allows the thermalization time to become smaller. The pressure inside the cryostat is controlled by a vacuum pump. At low temperatures the pressure value is equal to 10^{-7} mbar while at room temperature it is equal to 10^{-4} mbar.

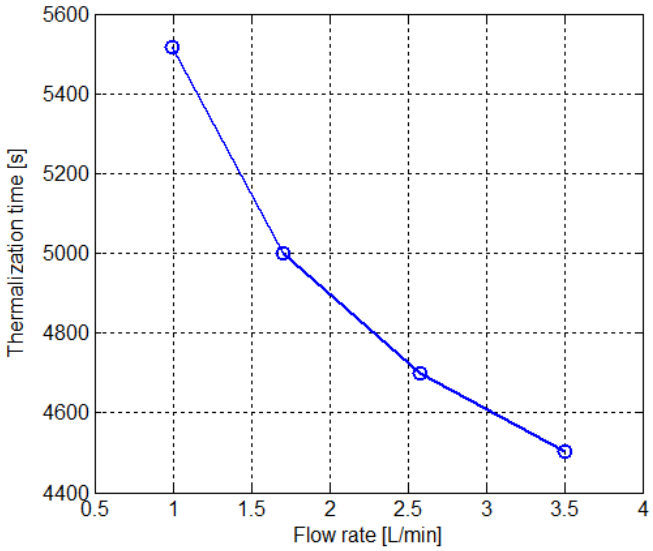

Figure 5.6. *Thermalization time as a function of the flow rate.*

5.1.3. Electrical setup

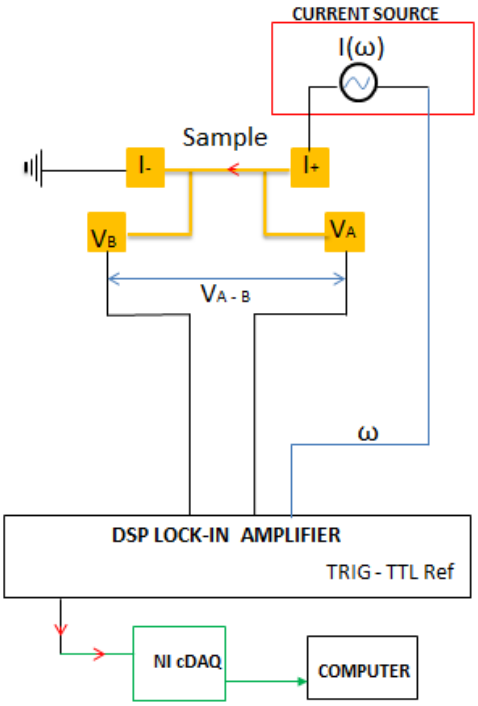

Figure 5.7. *Simplify schematic diagram of electrical circuit.*

An AC or DC current is delivered by a current source model (Keithley 6221) through the metallic line and undergoes Joule heating. Voltage drop across the heater is measured differentially with in the lock-in amplifier (LIA), both the 1ω and 3ω voltages are measured simultaneously by using the separate channel of the LIA to read the different harmonics. The schematic of the measurement setup is shown in Fig. 5.7. The objective is to measure the first harmonic voltage and the in-phase and out-of-phase third harmonic voltage through which the thermal conductance at low frequencies and thermal conductivity with 3ω measurements can be deduced.

5.2. Temperature coefficient of resistance

5.2.1. Theory of electrical resistivity

Following Eq. 2.1, the electrical resistance of the metallic heater depends linearly on its temperature as

$$R = R(T_0) + R(T_0)\alpha\Delta T \tag{5.1}$$

where

$$R(T_0) = \rho(T_0)\frac{L}{S}, \tag{5.2}$$

is the original electrical resistance of the heater of length L and cross section $S = 2b \times d_h$, the temperature coefficient of resistance (TCR denoted α) is defined as the relative change of resistance when the temperature is changed by one kelvin (see Eq. 2.2) and $\Delta T = T - T_0$ is the temperature change of the heater. The electrical resistivity of a metal depends on a variety of scattering mechanisms such as electron–phonon scattering, electron–defect scattering, or the electrons–impurity scattering. If these scattering mechanisms are independent from each other, Matthiessen's rule states that electrical resistivity is the sum of all contributions due to the various scattering mechanisms and it can be divided into two components:

$$\rho(T) = \underbrace{\rho_{defect} + \rho_{impurity} + \rho_{boundary}(2b, e)}_{\rho_{res}} + \underbrace{\rho_{el-ph}}_{\rho_{el-ph}(T)}, \tag{5.3}$$

where ρ_{defect} the resistivity due to electron–defect scattering, $\rho_{impurity}$ the electron–impurity scattering, $\rho_{boundary}$ the resistivity due to electron scattering at the boundaries, ρ_{res} is the residual resistivity at T= 0 K, which is temperature independent, $\rho_{el-ph}(T)$ the resistivity caused by the scattering of charges (electron or holes) by quantized vibrations of the lattice (i.e., phonons) and their collisions with each others [4]. The alternative formulation of Matthiessen's rule in terms of respective scattering rates has the form

$$\frac{1}{\tau} = \frac{1}{\tau_{el-ph}} + \frac{1}{\tau_{res}}. \tag{5.4}$$

The boundary scattering can be analyzed with a Fuchs–Sondheimer model involving some specular coefficient [4]. However, this is mostly valid for monocrystalline selection while deposited metal is shown to be polycrystalline. Grain boundary scattering may then be predominant. Useful references can be found in [5, 6, 7, 8, 9, 10, 11, 12].

The temperature dependence of the electrical resistivity over entire temperature range can be explained using the Bloch–Grüneisen formula

$$\rho_{el-ph}(T) = \alpha_{el-ph}(\frac{T}{\theta_D})^n \int_0^{\theta_D/T} \frac{x^n}{(e^x-1)(1-e^{-x})}dx, \tag{5.5}$$

where α_{el-ph} is a constant proportional to $\lambda_{tr}\frac{\omega_D}{\omega_p^2}$ with λ_{tr} the electron–phonon coupling constant, ω_p is the plasmon frequency [13] and ω_D the Debye temperature of the chosen metal. For acoustic phonons the value of α_{el-ph} is 4.225 [14]. The constant n generally takes the value 2, 3 or 5 depending on the nature of interaction. In a non–magnetic crystalline metallic solid like Cu, Ag, or Au, n=5. Phonon–scattering resistivity can be written as

$$\rho_{el-ph}(T) = \alpha_{el-ph}\left(\frac{T}{\theta_D}\right)^5 \int_0^{\theta_D/T} \frac{x^5}{(e^x-1)(1-e^{-x})}dx, \tag{5.6}$$

where $\theta_D(Au)$ = 165 K. Fig. 5.8 presents the typical temperature dependence of the resistivity of gold. Temperature dependence of the resistivity can be studied in two different regimes. At low temperatures ($T << \theta_D$), the resistivity can be written in the form [15]

$$\rho_{el-ph}(T) = 124.431\alpha_{el-ph}\left(\frac{T}{\theta_D}\right)^5, \qquad T \to 0. \tag{5.7}$$

This behavior is explained by the fact that the number of phonons increases proportionally to T^3 and an additional weighting factor for the angle dependence of scattering process proportional to T^2. On the other hand for higher temperatures, the scattering rate τ^{-1} for electron–phonon increases proportionally to the number of occupied phonon states which increases linearly with temperature. Hence the resistivity can be approximated as

$$\rho_{el-ph}(T) \rightarrow \frac{1}{4}\alpha_{el-ph}\left(\frac{T}{\theta_D}\right), \qquad T > \theta_D. \tag{5.8}$$

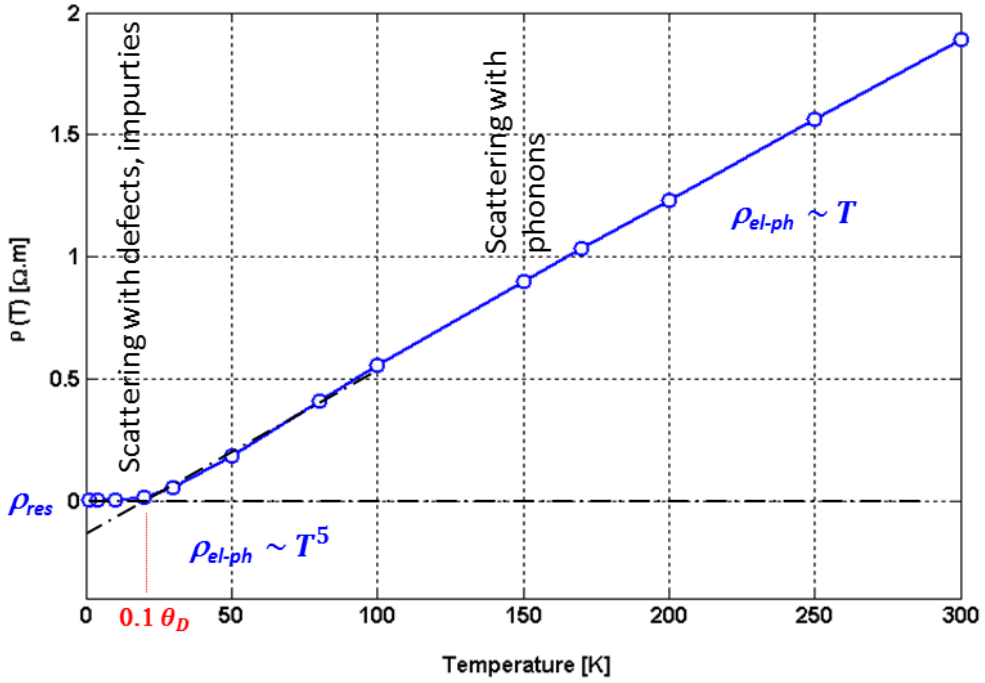

Figure 5.8. *Temperature dependence of the electrical resistivity of gold.*

The resulting evolution of the temperature coefficient of resistance in the entire temperature range is presented in Fig. 5.9. We notice that the TCR of gold is dependent on temperature.

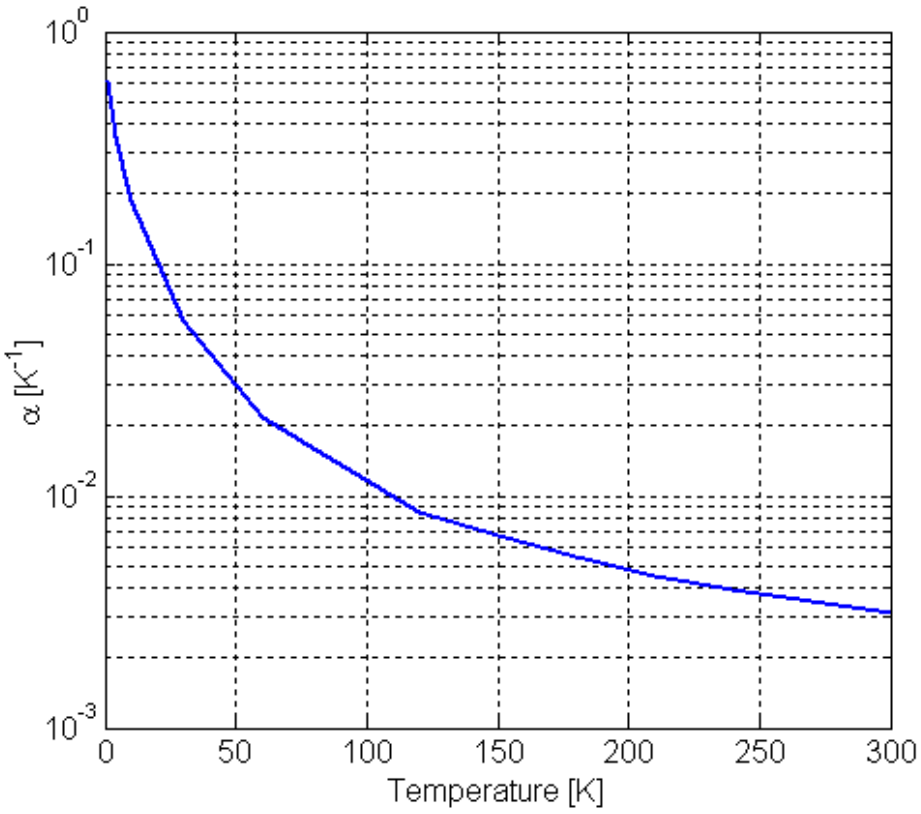

Figure 5.9. *Temperature coefficient of resistance of gold as a function of temperature range.*

5.2.2. Experimental determination of the temperature coefficient of resistance

The TCR is measured using the cold finger inside the cryostat. Five different devices of widths 109 nm, 200 nm, 2 μm, 5 μm and 10 μm on silicon substrates have been chosen for our experimental measurements. First, we introduce the measurements on the device of 200 nm width. The same experimental measurements steps are done on each device. At certain temperature, we measure the voltage drop across the inner pads of the probed device as a function of current as presented in Fig. 5.10 (a). While the resistance can in principle be determined by the slope of the curve in Fig. 5.10 (a), we prefer to plot the resistance as a function of power as shown in Fig. 5.10 (b) and fit the curve to find the value at origin R_0. This method is found more reliable. Remember that we are looking for tiny variation of $\frac{dR}{R}$ and that the resistance should be determined accurately. It is verified that the resistance varies linearly with power. Reproducing this procedure at

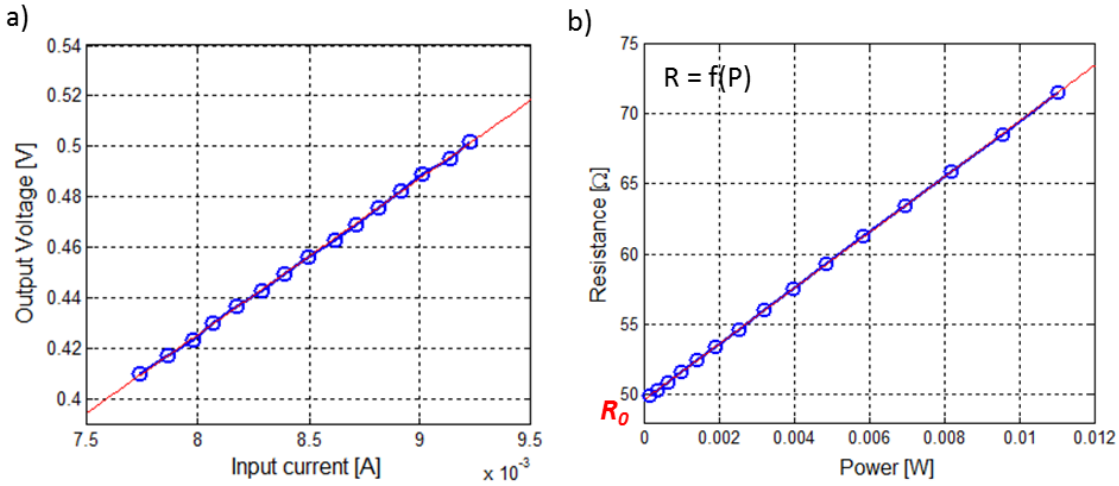

Figure 5.10. *(a) I-V curve to measure the resistance value at certain temperature, (b) resistance-power curve to obtain R_0 at base temperature.*

each temperature, we are able to plot the resistance R_0 as a function of temperature. Fig. 5.11 shows the expected linear behavior. From two different temperatures T_1 and T_2, the TCR is computed as

$$\alpha = \frac{d\rho}{dT} = \frac{\rho(T_2) - \rho(T_1)}{T_2 - T_1} \times \frac{2}{\rho(T_f) + \rho(T_1)}. \tag{5.9}$$

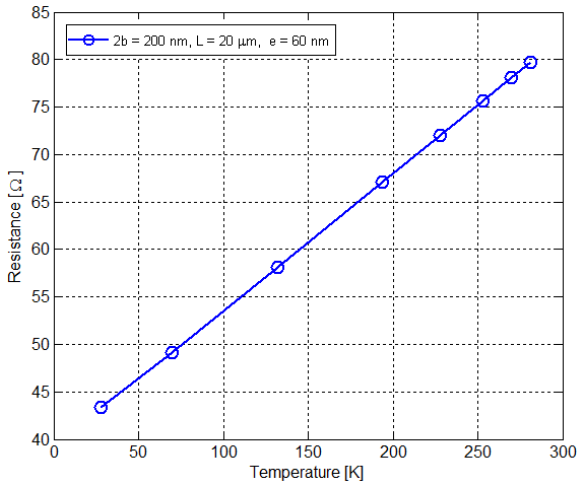

Figure 5.11. *Base resistance R_0 as a function of temperature.*

Hence, the TCR is determined as presented in Fig. 5.12.

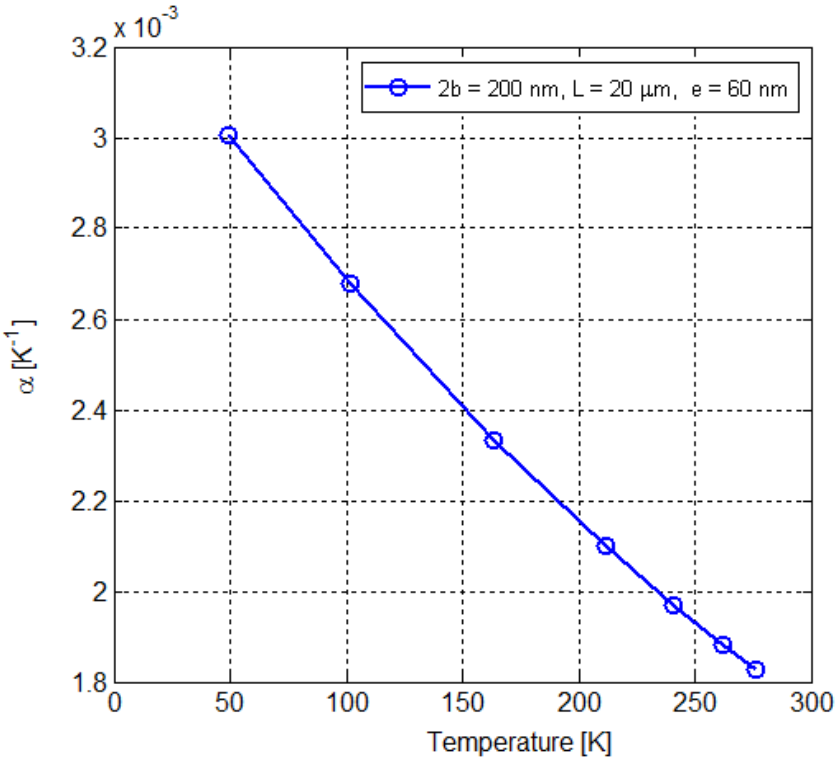

Figure 5.12. *Temperature coefficient of the resistance as a function of temperatures.*

Recent studies showed that the electrical resistivity can be influenced by the surface roughness and grain boundary scattering. When the thin film decreases, electrical resistivity increases [11]. At first sight, this was attributed to scattering of electrons with the surface of thin films [5, 6]. But Maydas and Shatzkes [16] showed a significant resistivity increase due to the grain boundary in thin films. We study experimentally the impact of the wire width on the electrical resistivity at room temperature as presented in Fig. 5.13. The results obtained are in agreement with these studies. However, we observe little dispersion in the measured resistivities of the microwires. The evolution in temperature is represented in Fig. 5.14 (a): it is seen that the slopes become less steep when the width decreases.

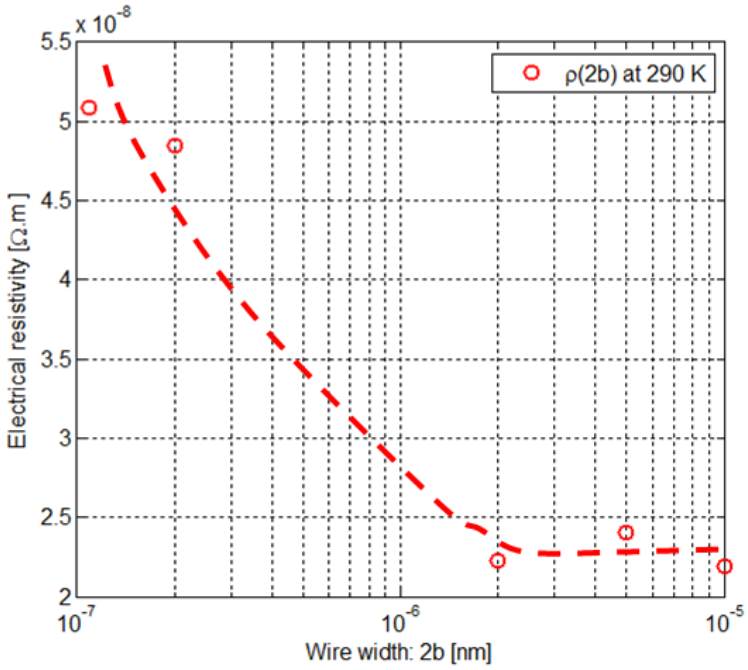

Figure 5.13. *Resistivity of gold wire as a function of wire width. The dashed line represents an extrapolation of the resistivity.*

Fig. 5.14(b) shows the TCR of different devices. It can be seen that TCR is dependent on temperature and it increases as the temperature decreases.

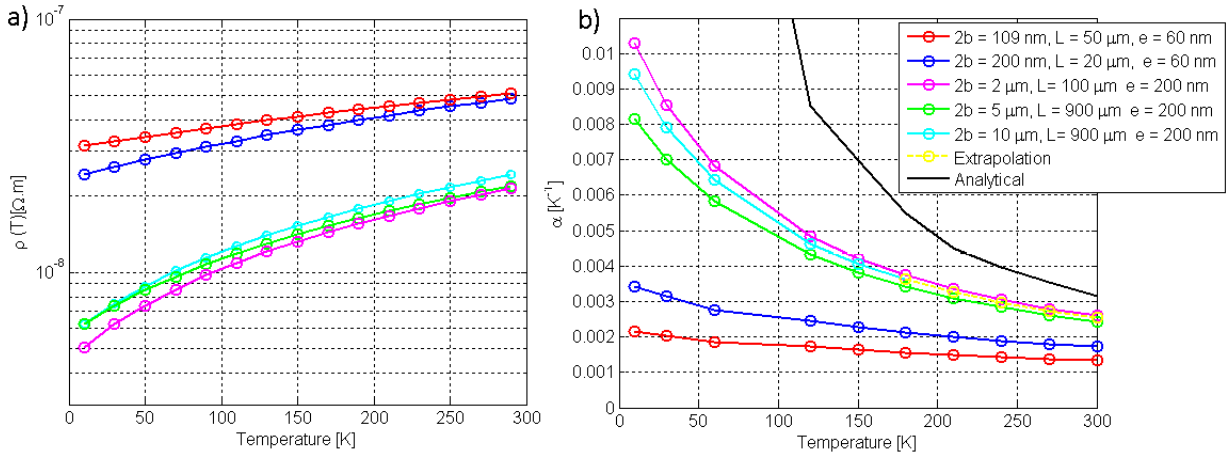

Figure 5.14. *(a) Electrical resistivity as a function of temperature of different wires. (b) Temperature coefficient of the resistance as a function of temperature.*

5.2.3. Comparison with theory

Fig. 5.14 shows a comparison between theory and experimental measurements of TCR as a function of temperature. We notice the same behavior with respect to temperature. However, the experimental measurements are always lower than the theoretical value. An experimental reason could be that the waiting time between two points was too small and that thermalization would not have been reached at each temperature, despite the care we took with the thermalization time. This is particularly possible for the large microlines, where small differences (up to 20%) can be observed. However, this argument cannot explain the difference with the nanolines. Several reasons may lead to this shift. In the following, we suppose that there is no electron leakage through the substrate. The increase of the electron collisions with the wire boundaries should also be discarded, because the sizes stay larger than the electron mean free path. However, we notice that the analytically–studied material is monocrystalline while experimentally it is polycrystalline. Thus, the silicon grains in the whole heater may depend on the width and thickness of the wire (see in particular Fig. 4.16 (b), where grain features can be observed). This would also explain why the thinnest wire has the smallest TCR and why the temperature dependence softens with size: the main electron scattering mechanism takes place at grain boundaries, which is less temperature dependent than electron-phonon scattering. Finally, note that in the experiment we use 5 nm of Cr as an adhesion layer between the gold and the silicon substrate, and this additional layer of Cr could also affect the total resistance of the device, and therefore the TCR.

5.3. Heat diffusion from microlines

Measurements using the 1ω and 3ω method were done on different metallic lines on different substrates. Table 5.1 (see p. 132) summarizes the properties of five of the metallic lines. First we made 1ω measurements at very low frequency and then we made 3ω measurements to deduce the thermal conductivity value of the probed materials.

5.3.1. Thermal conductivity for different materials

1. Measurement process and data treatment

a) 3ω method

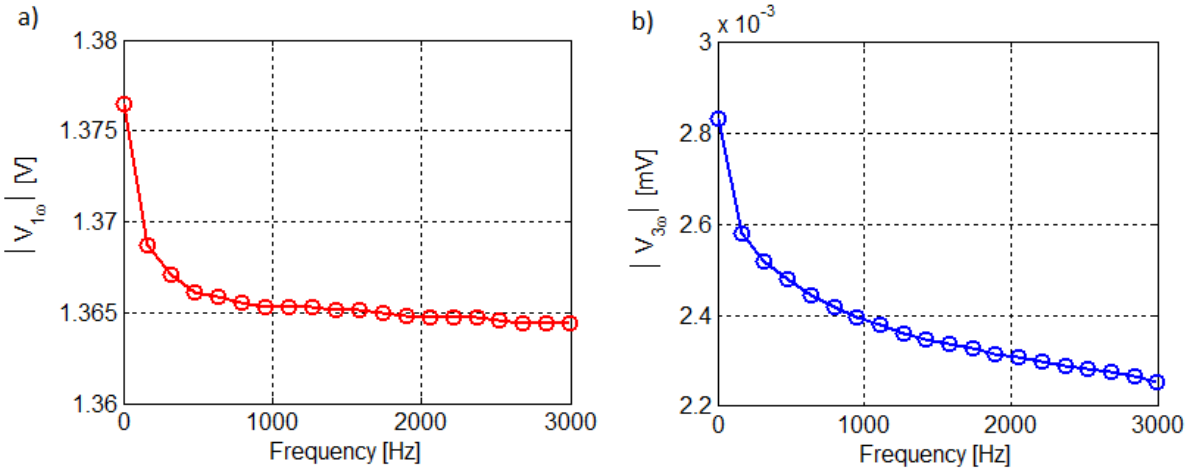

Figure 5.15. *(a) First harmonic voltage and (b) third harmonic voltage as a function of frequency in the case of heat dissipation on a silicon wafer.*

Measurements are done on several metallic lines of different dimensions and are performed in the linear regime frequency range at room temperature T_0. Since many materials were measured, we choose to present in this section one of our measurements in silicon substrate where the metallic line length is 256 µm and of width 2 µm. The same experimental steps were done on the other materials. The results are presented in Fig. 5.15. They show a relative stability of the signal at 1ω and a decay of the 3ω signal as a function of frequency. The ratio between the first and the third harmonic signals $|V_{3\omega}/V_{1\omega}|$ is presented in Fig. 5.16.

The ratio is linear with respect to the logarithm of the frequency on a part of the plot. Our useful frequencies range up to 2500 Hz ($\ln(\omega) \simeq 9.7$). At lowest frequencies, the penetration depth is too large to exploit the slope regime and at the highest frequencies distortion due to the electronics may be present. In order to deduce the thermal conductivity, temperature oscillation as a function of logarithm of the frequency is plot (see Fig. 5.17). The data are obtained by means of Eq. 2.17.

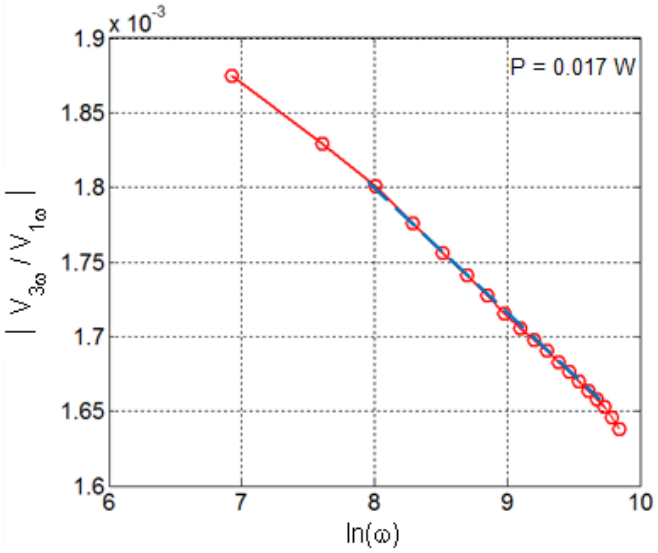

Figure 5.16. *Ratio between the first and the third harmonic voltage amplitudes.*

Fig. 5.17 represents the in-phase temperature oscillation measured in the linear regime versus the natural logarithm of the thermal excitation frequency ω for silicon.

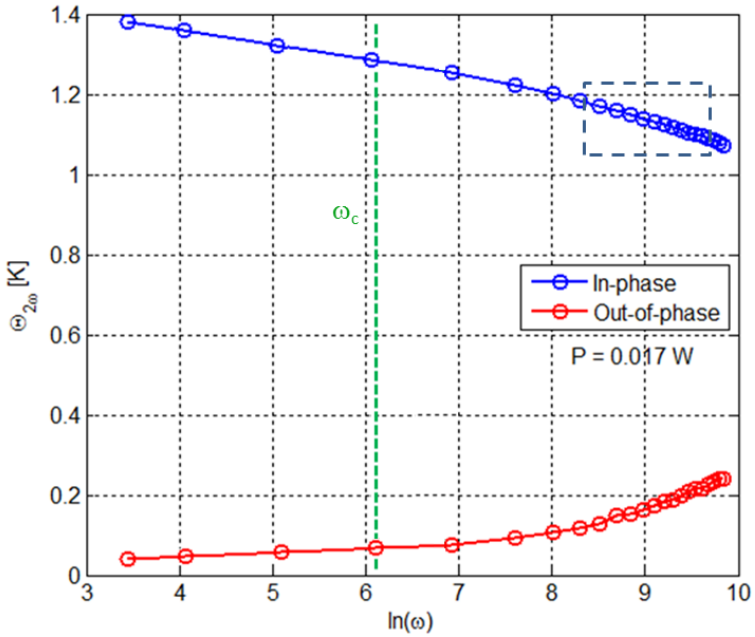

Figure 5.17. *In-phase (blue) and out-of-phase (red) third harmonic voltages measured on silicon substrate.*

It shows unsaturated in-phase temperature oscillation at low frequencies in contrast to 2D analytical calculations. This is due to the influence of substrate and due to the 3D nature of the heated dissipation in our devices that do not verify the $L/2b$ condition at low frequencies (see Section 3.2).

Using the basic fitting, the slope value in the linear regime is calculated while the power per unit length is known. Following Eq. 3.38, thermal conductivity value yields 149 ± 0.3 $\mathrm{W.m^{-1}.K^{-1}}$ in agreement with the expected value 148 $\mathrm{W.m^{-1}.K^{-1}}$. Table 5.1 provides the result obtained for set of materials. The obtained values are close to the predicted ones. We can observe that the value of fused quartz determined is higher than that of silica (1.3 $\mathrm{W.m^{-1}.K^{-1}}$), which is in principle unexpected.

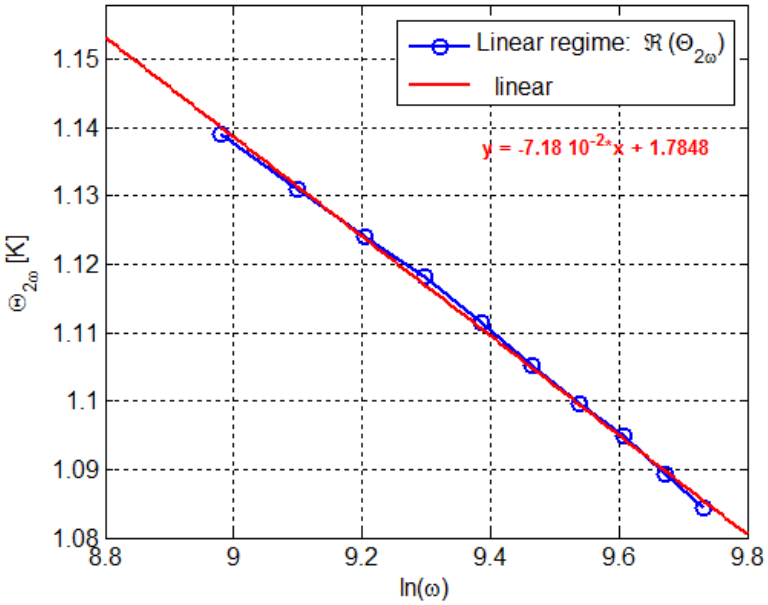

Figure 5.18. *In-phase third harmonic voltage in the linear regime as a function of circular frequency.*

b) Low–frequency behavior

At low frequency, if the plateau regime (see Fig. 3.13) is achieved, the ratio of measured thermal conductance to thermal conductivity should be constant for a given geometry. It is given by Eq. 3.46.

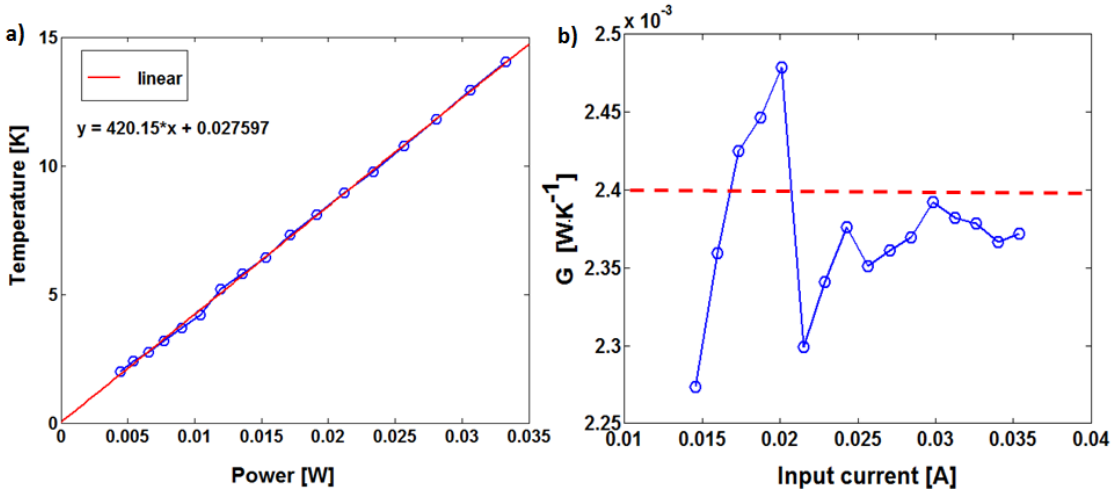

Figure 5.19. *(a) Temperature rise as the function of electrical power. (b) Thermal conductance as a function of input current. The average value is shown by the dashed red line.*

By knowing the TCR and plotting the electrical resistance as a function of input power (see Fig. 5.10 (b)), the temperature rise can be found as a function of power (Fig. 5.19 (a)). The linear relation between the temperature rise and the electric power allows to calculate the slope value, and to deduce the thermal conductance of 2.4 $\times 10^{-3}$ W.K^{-1} from the slope. Note that this is more precise than deducing it from single dots (Fig. 5.19 (b)). Similar measurements are done for the other materials. 3D DC FEM calculations are performed for different materials to find the expected ratio at law frequency. Results are presented in Table 5.1.

Substrate	Length [µm]	Width [µm]	Measured thermal conductivity κ [W.m^{-1}.K^{-1}]	Expected thermal conductivity (literature) κ [W.m^{-1}.K^{-1}]	Thermal conductance G_{th} [W.K^{-1}]	Experimental ratio: $\frac{G_{th}}{\kappa}$ [m]	Expected ratio: $\frac{G_{th-3D}}{\kappa}$ [m]
Silicon (Si)	256	2	149.3	149	2.4×10^{-3}	1.60×10^{-5}	1.60×10^{-5}
Sapphire (Al_2O_3)	256	5	37.5	37	1.7 ×10^{-3}	4.53×10^{-5}	7.10×10^{-5}
Alumina (Al_2O_3)	256	2	32	33.6	1.8 ×10^{-3}	5.35×10^{-5}	5.60×10^{-5}
Crystal quartz (SiO_2)	500	5	8.6	10.5	8.5 ×10^{-4}	9.59×10^{-5}	8.39×10^{-5}
Fused quartz (SiO_2)	1300	10	2	1.3	6.88 ×10^{-4}	34.40 ×10^{-5}	22.16 ×10^{-5}

Table 5.1. *Values of thermal conductivity for each material. The ratio of the thermal conductance over conductivity is deduced.*

The ratio of $\frac{G_{th}}{\kappa}$ has the same order of magnitude and it decreases as the thermal

conductivity of the studied substrate increases. It is found that the ratio is not constant and does not agree with the theoretical values. This is another proof that we do not reach the plateau regime typical of 2D at low frequency.

5.3.2. Thin films

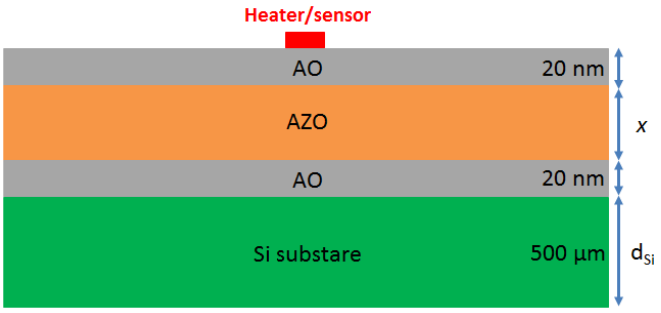

Figure 5.20. *A schematic of different layers grown on Si-substrate.*

New multilayer samples were provided by a company for developing a new coating technology. The technique is applied to multilayer samples. The objective is to characterize the effect of layering on the thermal conductance. These samples are conformally coated with Atomic Layer Deposition (ALD). The layers are made of oxides, such as aluminum oxide (AO) or aluminum zinc oxide (AZO). Thin films of different thicknesses d_F and thermal conductivity κ_f were deposited on the surface of the silicon substrates of thickness d_{Si} = 500 µm and thermal conductivity κ_{Si} (see Fig. 5.20). As shown in Eq. 3.47, a frequency–independent temperature rise ΔT_F due to the thin film adds to the in–phase temperature oscillations across the metallic line. Temperature rise due to thin film is a real value consequently increasing the temperature oscillation ΔT_S. The result is the complex (in–phase and out–of–phase) temperature oscillation ΔT_{AC}. Our experimental measurements were performed on different thicknesses d_F of AO (20 nm) - AZO (x) - AO (20 nm), where x is varying between 5 nm and 50 nm in order to observe the change in the value of the temperature rise. Temperature rise due to thin film thickness is given in Eq. 3.48. Our experimental results are shown in Fig. 5.21.

The obtained results show a non-monotonic behavior, so that there is no expected order in temperature rise due to the AZO layer thickness. While this can appear surprising at first sight, it happens that our measurements have the same trend than that obtained by SThM performed at two different laboratories. The issue may be due to material

fabrication stability. It is worth noting that the thickest layer seems to depart from the trend observed for the two other curves at high frequency. The other curves provide thermal conductivity of the substrate, obtained by analysis the high frequency behavior with the 3ω method, close to that of silicon. The temperature rise could be due to both material volume or boundary resistance. Note that the heater measures only the temperature rise on the top surface of the sample which includes the temperature drop across the film and substrate. As a result, it is not easy to disentangle the effects of all layers.

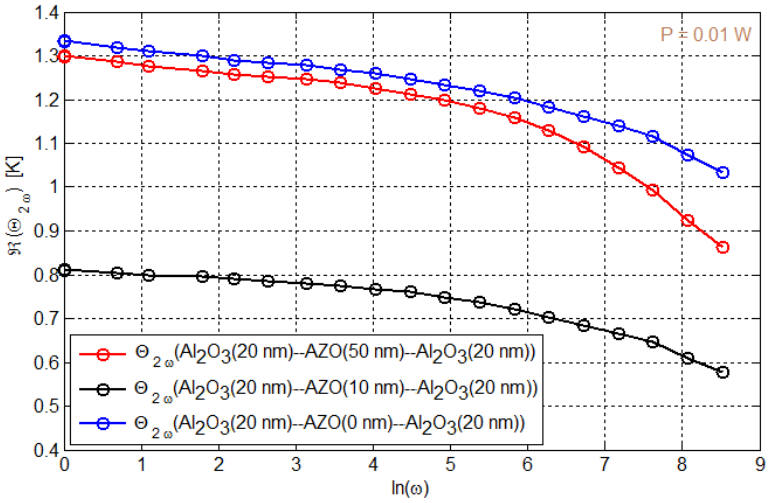

Figure 5.21. *Temperature response obtained due to the thin film deposited on substrate for metallic line of width 2 µm and length 256 µm.*

5.4. Main conclusions

We have shown that a full electro–thermal setup has been developed, which can be used for 3ω measurements or alternative methods. Among the main results obtained, we showed that the temperature coefficient of resistance depends on the size of the metallic wire: it is therefore always crucial to measure it. Its temperature behavior softens where the size decreases. The hypothesis is that this is due to grain size reduction. It was then shown that the 3ω method can be applied in the highest part of our measured frequency range. In contrast, the plateau particularly observed at low frequency is not seen due to low length/width ratio. The technique was applied to multilayer materials. Devices for measuring the thermal conductivity of silicon nitride layers have also been realized in

collaboration with some colleagues in Switzerland, and are to be measured in the very near future. Their designs can be found in Appendix C. All the works presented in this chapter are a first step toward experiments with metallic lines of submicronic widths. This is the object of the next chapter.

References

[1] F. Farassat and W. Birgel, *Ball bonding method and apparatus for performing the method*, (1990), uS Patent 4,925,083.

[2] W. Moden, *BGA package and method of fabrication*, (2001), uS Patent 6,310,390.

[3] S. Murali, N. Srikanth and C. J. Vath, *An analysis of intermetallics formation of gold and copper ball bonding on thermal aging*, Materials Research Bulletin **38**, 637 (2003).

[4] J. M. Ziman, *Electrons and phonons: the theory of transport phenomena in solids*, (1960).

[5] K. L. Chopra, *Thin film phenomena*, (1969).

[6] E. H. Sondheimer, *The mean free path of electrons in metals*, Advances in Physics **50**, 499 (2001).

[7] A. Bid, A. Bora and A. Raychaudhuri, *Temperature dependence of the resistance of metallic nanowires of diameter 15nm: applicability of Bloch-Grüneisen theorem*, Physical Review B: Condensed Matter and Materials Physics **74**, 035426_1 (2006).

[8] C. Durkan and M. Welland, *Size effects in the electrical resistivity of polycrystalline nanowires*, Physical Review B **61**, 14215 (2000).

[9] W. Steinhögl, G. Schindler, G. Steinlesberger and M. Engelhardt, *Size-dependent resistivity of metallic wires in the mesoscopic range*, Physical Review B **66**, 075414 (2002).

[10] D. Josell, C. Burkhard, Y. Li, Y.-W. Cheng, R. Keller, C. Witt, D. Kelley, J. Bonevich, B. Baker and T. Moffat, *Electrical properties of superfilled sub-micrometer silver metallizations*, Journal of Applied Physics **96**, 759 (2004).

[11] W. Wu, S. Brongersma, M. Van Hove and K. Maex, *Influence of surface and grain-boundary scattering on the resistivity of copper in reduced dimensions*, Applied Physics Letters **84**, 2838 (2004).

[12] R. Henriquez, S. Cancino, A. Espinosa, M. Flores, T. Hoffmann, G. Kremer, J. G. Lisoni, L. Moraga, R. Morales, S. Oyarzun *et al.*, *Electron grain boundary scattering and the resistivity of nanometric metallic structures*, Physical Review B **82**, 113409 (2010).

[13] P. B. Allen, J. Chelikowsky and S. Louie, *Quantum Theory of Real Materials*, (1996).

[14] P. Rossiter and J. Bass, *Materials Science and Technology vol 3A, ed RW Cahn, P Haasen and EJ Kramer*, (1991).

[15] F. J. Blatt, *Physics of electronic conduction in solids*, (1968).

[16] A. Mayadas and M. Shatzkes, *Electrical-resistivity model for polycrystalline films: the case of arbitrary reflection at external surfaces*, Physical Review B **1**, 1382 (1970).

CHAPTER 6

Deposited nanowires as ballistic heat sources

In this chapter, the phonon average mean free path is of the order of or larger than the width of the deposited line. In this case, Fourier's law is no longer applicable while phonon transport can be analyzed with the Boltzmann transport equation. In particular, the BTE can be integrated in a form similar to radiative transport equation, known as the equation of phonon radiative transfer (EPRT) [1]. In Section 6.1, we introduce the results obtained based on submicron sources at room temperature. Temperature-dependent conductance measurements on submicron heat sources are presented in Section 6.2. All the results are compared with finite-element method based simulations, which account only for the diffusive regime. Previous results investigating the effect of phonon confinement in ridges on the thermal conductance are then reminded. A comparison between our experimental results with the ridge ones [2] is performed in Section 6.3. In both cases, the results are analyzed in light of the Knudsen number. In Sections 6.4 theoretical results obtained with the BTE and the equation of phonon radiative transfer are presented. Finally, the experimental results with the deposited lines and the ridges are compared in Section 6.5.

6.1. Sources size effect at room temperature

In this section, we provide our experimental results based on submicron sources at room temperature. The measurements are performed in the standard 4-point geometry at room temperature under vacuum pressure and at low frequency (5 Hz). Similar experimental measurements to those of the microlines are performed with widths of 200 nm and 109 nm. Fig. 6.1 highlights the experimental results based on the device of width 109 nm and of length 50 µm.

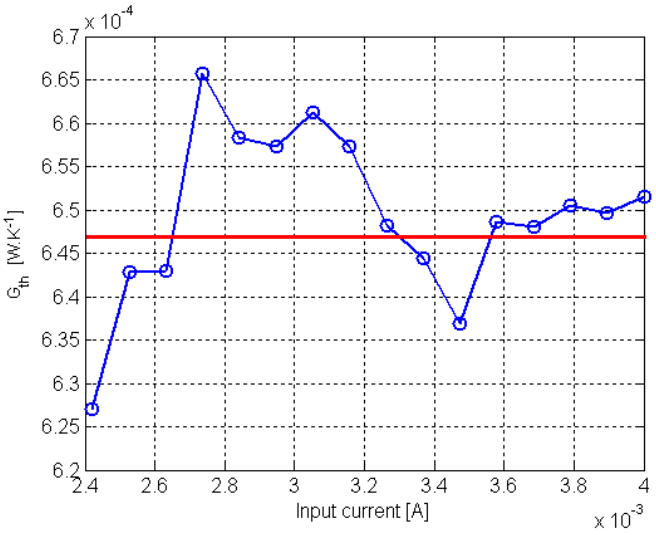

Figure 6.1. *Thermal conductance as a function of current. The dispersion of the dots provides clues about the random error.*

The average value of the thermal conductance is $6.46\times10^{-4}\mathrm{W.K^{-1}}$. Results on nanodevices are also given in Table 6.1.

The characteristic sizes of the heaters, i.e. their widths $2b$ and lengths L, allow us to investigate thermal transport at micro and nanoscale. The aspect ratio $L/2b$ and the surface area $2b \times L$ of the heater can provide more details about thermal transport at different scales. Table 6.1 provides the thermal conductance values with the heater aspect ratios and surface areas. It can be noticed that while the aspect ratio is greater than 200 in case of the nanodevices, the length may not be large enough for the 3ω measurements since the heater length is also on the order of the diffusion length. As a result all the data reported here were not found with the 3ω slope method. We first analyze as a function of the central part of the wire where we are sure to know the

Frequency [Hz]	Width [µm]	Total length [µm]	Central length [µm]	Aspect ratio of the full part $L/2b$	Aspect ratio of the probed part $L/2b$	Surface of the full part $L\times 2b$ [µm^2]	Surface of the probed part $L\times 2b$ [µm^2]	Thermal conductance G_{th} [W.K^{-1}]
5	0.109	70	50	642	459	7.63	5.45	6.46×10^{-4}
	0.2	70	50	350	250	14	10	1.39×10^{-3}
	0.2	70	50	350	250	14	10	1.34×10^{-3}
	0.2	40	20	200	100	8	4	4.01×10^{-4}
	2	300	256	150	128	600	512	2.36×10^{-3}
	5	1600	1300	320	260	8000	6500	5.59×10^{-3}

Table 6.1. *Thermal conductances as a function of the devices width, length, area and aspect ratio.*

temperature. In Fig. 6.2 (a), (b), we can observe that as the surface area of the device decreases, the thermal conductance decreases. An approximate logarithmic trend can be observed when including the largest area. If we do not account for the largest area, the trend may appear as softer.

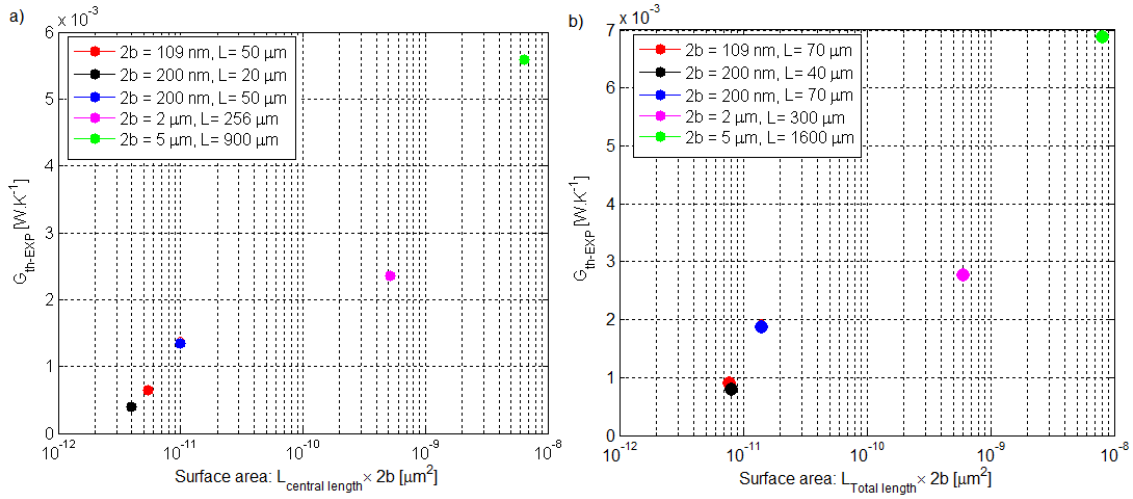

Figure 6.2. *Thermal conductance versus surface heat sources (a) central length and (b) total length at room temperature.*

We compare these results with 3D FEM simulation in the DC regime. Fig. 6.3 reports on the FEM thermal conductance results which are larger than the ones measured. The

trend is similar, apart from a point associated to a nanoline.

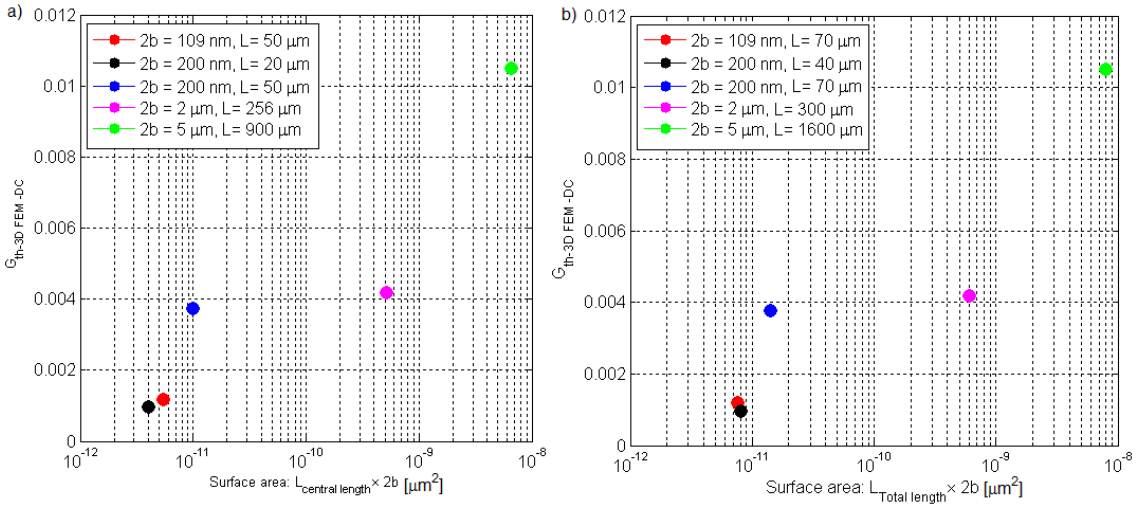

Figure 6.3. *3D FEM: Thermal conductance on surface heat sources (a) central length and (b) total length at room temperature.*

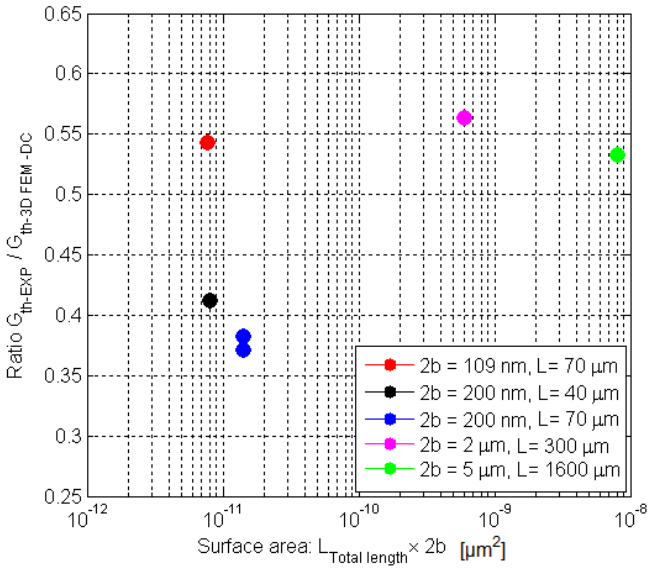

Figure 6.4. *Ratio of experimental and DC FEM thermal conductance at room temperature.*

Fig. 6.5 shows the ratio of the experimental conductance by the 3D DC FEM simulated one in the case of the central part of the wire. The obtained ratio is between 0.3 and 0.56 for all devices. Two different devices of length 50 µm and width 200 nm are measured.

The obtained result are very close to each other (see Table 6.1).

We now turn to the aspect ratio $L/2b$. It is difficult to find an order here. The simulations also reproduce approximately the observed behavior, being off by a factor close to 2.

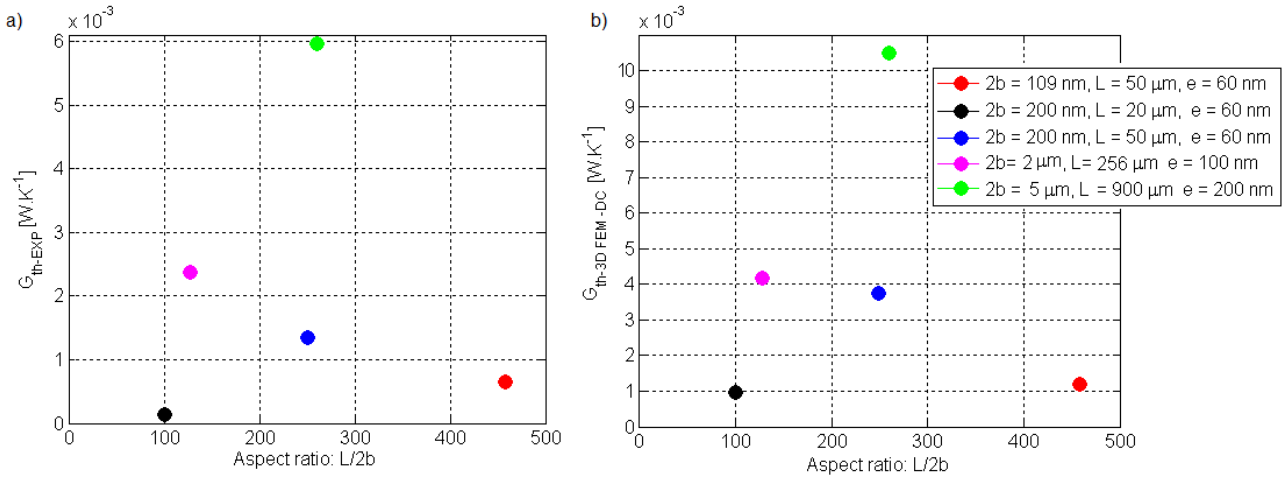

Figure 6.5. *(a) Thermal conductance versus aspect ratio $L/2b$ at room temperature. (b) 3D FEM DC simulation of the same devices.*

We have also performed the analysis as a function of the total wire. If the wire is isothermal, it is indeed the whole wire which needs to be considered. As a result, we find that the conductance scales with the area and not with the aspect ratio. The diffusive simulations mostly reproduce the trends, but are not exact quantitatively. This can be due to the fact DC simulations are performed while the experiment have been made in the low-frequency regime. In addition, the pads may play a role.

6.2. Thermal conductance as a function of temperature

The heat transport measurements are performed in the open-cycle helium filled cryostat. The substrate temperature is measured by the calibrated diode thermometer located on the sample holder. Temperature steps of 5 K, 10 K, or 20 K are considered. Analyses with both decreasing and increasing temperature steps can be applied. Thermal conductance of different devices of widths 10 µm, 200 nm and 109 nm for a range of temperatures are measured. Fig. 6.6 (a) presents the thermal conductance measurement of a microdevice of 10 µm width as a function of temperature.

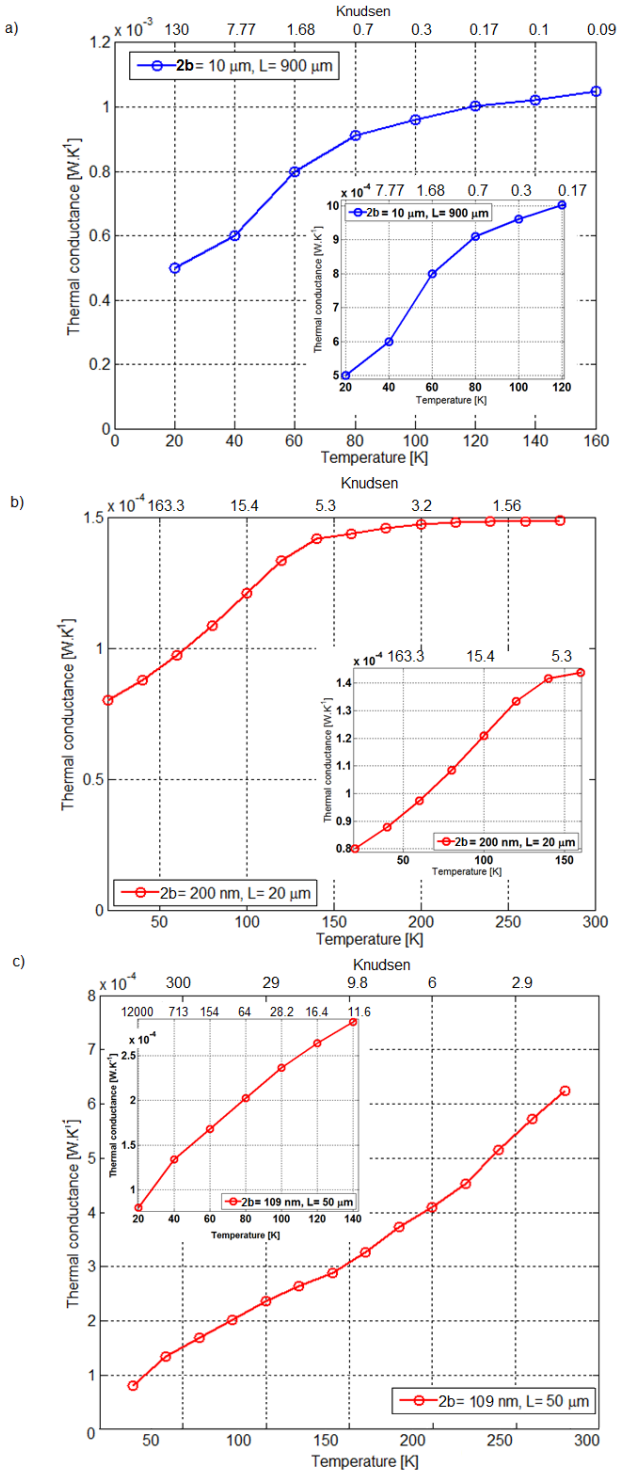

Figure 6.6. *Thermal conductance as a function of temperature for a heater (a) width of 10 µm and length of 900 µm, (b) width of 200 nm and length of 20 µm, (c) width of 109 nm and length of 50 µm.*

It can be noticed that the thermal conductance decreases as the temperature decreases. The measurements performed on the nanodevices with a heater width of 200 nm and 109 nm are presented in Fig. 6.6 (b) and Fig. 6.6 (c) respectively. The same behavior is observed for the widest wires, and the shape is a little bit different for the case of the narrowest one. Approximation Knudsen number associated with the devices are obtained, based on the average mean free path provided on Fig. 1.2. Very large values are reached. In the one–dimensional configuration, it is usually considered that the ballistic limit is reached when Kn = 100. It will be interesting to investigate the same value in more complex geometries. The thermal conductance as a function of temperature is very different from the diffusive one based on heater widths of 10 µm, 200 nm and 109 nm, respectively. In Fig. 6.7 (a) we represent the 2D behavior that one would observe if the transport was diffusive. The trend follows that of the thermal conductivity (see Fig. 1.5). We have already mentioned that our geometry may not be 2D, so we investigate the case of the 3D regime in DC (see Fig. 6.7 (b)). The same behavior is observed in all cases, the thermal conductance is proportional to the thermal conductivity. We therefore conclude that the behavior observed is very different in each case. In addition, the orders of magnitude are different.

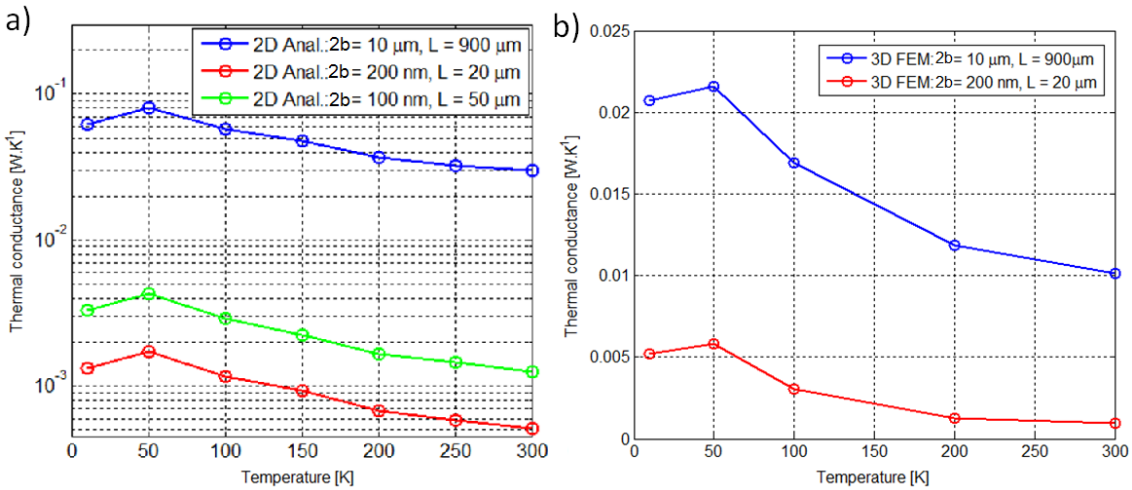

Figure 6.7. *Diffusive regime simulated with (a) 2D FEM and (b) 3D FEM.*

6.3. Effect of phonon confinement in ridges

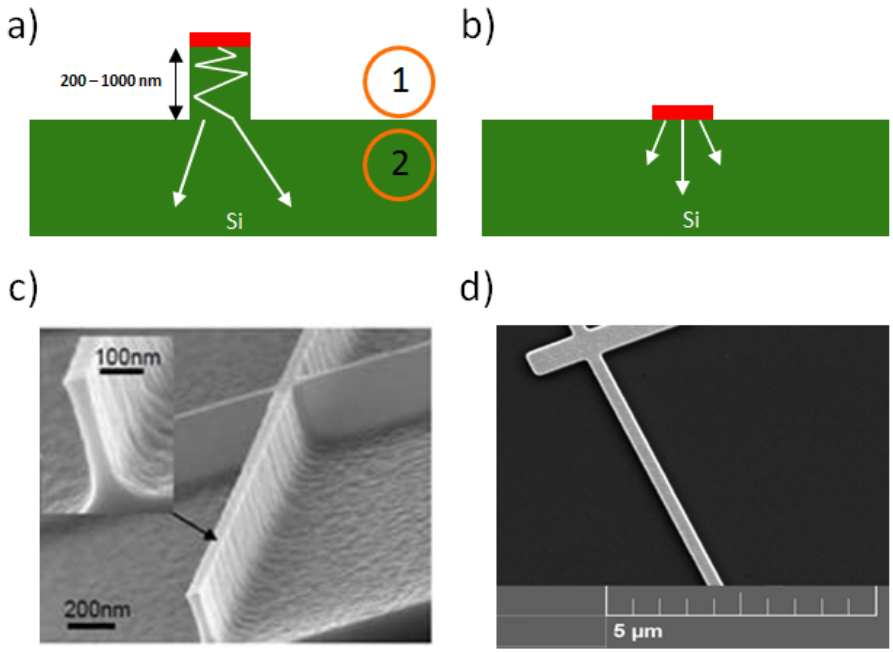

Figure 6.8. *(a) Geometry of the probed devices: a heater stands on top of a high ohmic Si ridge which lays on a planar substrate (region 2), (b) heater lays on top of a planar substrate, (c) SEM images of the ridges on top of the samples [2], (d) SEM image of the heater without ridge on top of the samples.*

Earlier studies also investigated experimentally the effect of the lateral confinement of acoustic phonons in ridges as a function of temperature. Similarly a large range of Knudsen numbers by using the temperature as a varying parameter [2]. The ridges stand on a planar Si wafer (see Fig. 6.8 (a), (c)) and the heater (in red) was deposited on top of silicon ridge. Heat flux can be generated in the conductor through means of Joule dissipation and has a one–dimensional flow in region (1) followed by the expansion of the heat flux lines in region (2). In our case (see Fig. 6.8 (b), (d)), the expansion of heat flux takes place directly in the probed substrate. The results obtained with the ridges are shown in Fig. 6.9. The order of magnitude of the determined thermal conductances is close to that of our devices. Our experimental results based on a device of 200 nm width are compared to those of a ridge with the same width. The comparison between the experimental measurements of both cases is presented in Fig. 6.10.

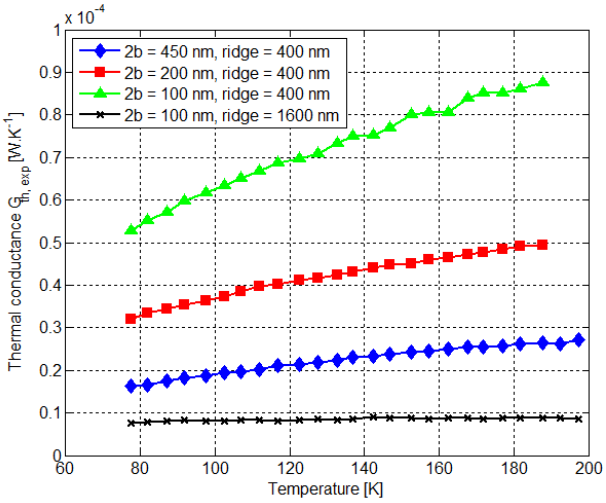

Figure 6.9. *Measured thermal conductances G_{th} as a function of the temperature [2].*

Note that the heaters are not the same. Those of the ridges were made of epitaxially doped silicon to avoid thermal boundary resistance with the highly–resistive silicon substrate. Fig. 6.10 shows that the ratio between the ridge and the wire–on–substrate is almost constant, with a value of 0.3. The area of the wire is different, so the exact effect of the ridge is different to assess. The fact that the results with two different heaters are similar suggests that boundary resistance is not strong, also in our case.

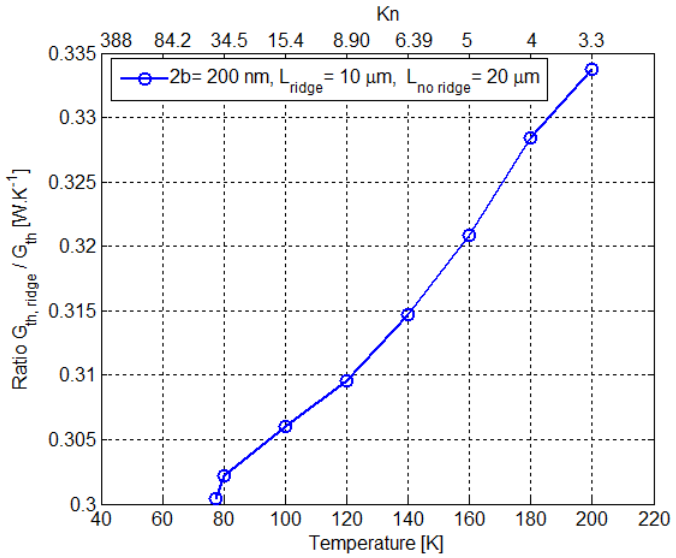

Figure 6.10. *Impact of ridges on the thermal conductance.*

6.4. Theoretical aspects and other experiments

6.4.1. Ballistic cylindrical and spherical geometries

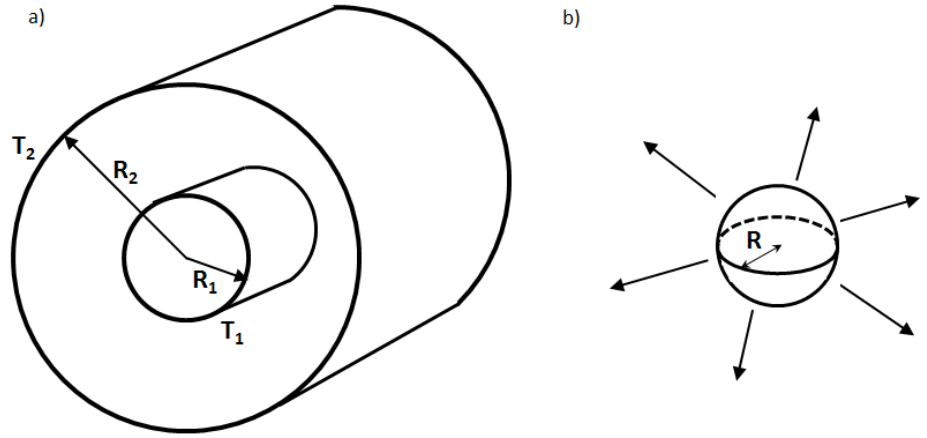

Figure 6.11. *(a) 2D ballistic configuration in cylindrical geometry. (b) Nanoparticle embedded in a material. R can be smaller than* Λ.

Similar to the 1D Cartesian case, it is possible to estimate the values of ballistic thermal conductances in cylindrical geometry (see Fig. 6.11 (a)), which possesses a physics close to the case of the infinite line (see Chapter 3 for this way of analysis), and to the spherical case (see Fig. 6.11 (b)), which possesses a physics close to that of a finite area on top of a surface. While the exact configuration to be investigated on top of the surface (which requires a 3D ballistic simulation) is not easy to deal with, approximate behaviors can be found with the following analyses.

a) Cylindrical geometry

For the cylindrical case, Lees and Liu [3] reports that for the case of air molecules that the reduction factor for the flux in comparison to the Fourier flux q_F is given by:

$$\frac{q}{q_F} = \frac{1}{1 + \dfrac{1}{\dfrac{4}{15}\dfrac{R_1}{\Lambda}\ln\left(\dfrac{R_2}{R_1}\right)}}. \tag{6.1}$$

The asymptotic behaviors for this formula, knowing that $q_F = \dfrac{2\pi L\lambda}{\ln\left(\dfrac{R_2}{R_1}\right)}\Delta T$, are as follows:

$$\begin{cases} \Lambda \to 0 \quad q \to q_F \quad \text{(Diffusion)} \\ \Lambda \to \infty \quad q \to \frac{8\pi}{15} L R_1 \dfrac{\lambda}{\Lambda}\Delta T \sim \frac{8\pi}{15} C\upsilon R_1 L\Delta T = \frac{8\pi}{45} C\upsilon S\Delta T \quad \text{(Ballistic)}. \end{cases} \tag{6.2}$$

It is interesting to observe that the ballistic limit in cylindrical geometry does not anymore depend on R_2. The shape of the surrounding medium does not play any role in the ballistic limit. The dependence on R_1 is linear. Note that the geometrical factor $\dfrac{8\pi}{45}$ may depend on the distribution function and therefore change for phonons. We point out that the geometry by Majumdar [1] is close to ours. However, heat flux level reduction is not provided.

Another choice instead of the formula of Eq. 6.1 is to apply the Wexler approximation [4, 5] . Thermal resistance can be predicted as a sum of a diffusion and ballistic term and expressed as

$$R = \frac{45}{8\pi}\frac{1}{C\upsilon 2bL} + \frac{\left[\ln\left(\dfrac{d_S}{2b}\right) + \beta\right]}{\pi\kappa L}, \tag{6.3}$$

where d_S is the substrate thickness and L = 50 µm and β was defined in Eq. 3.46. In the following it is neglected. The inverse of the thermal conductance per unit surface can be expressed as

$$r = RS = \frac{45}{8\pi}\frac{1}{C\upsilon} + 2b\frac{\ln\left(\dfrac{d_S}{2b}\right)}{\pi\kappa}. \tag{6.4}$$

Fig. 6.12 (a) represents the thermal resistance as a function of the wire width. It can be noticed that when the wire width is much larger than the phonon mean free path, the Fourier component (green) is largest. When the wire width is smaller than the phonon mean free path, the ballistic component is dominant (blue). Fig. 6.12 (b) represents r as a function of wire width.

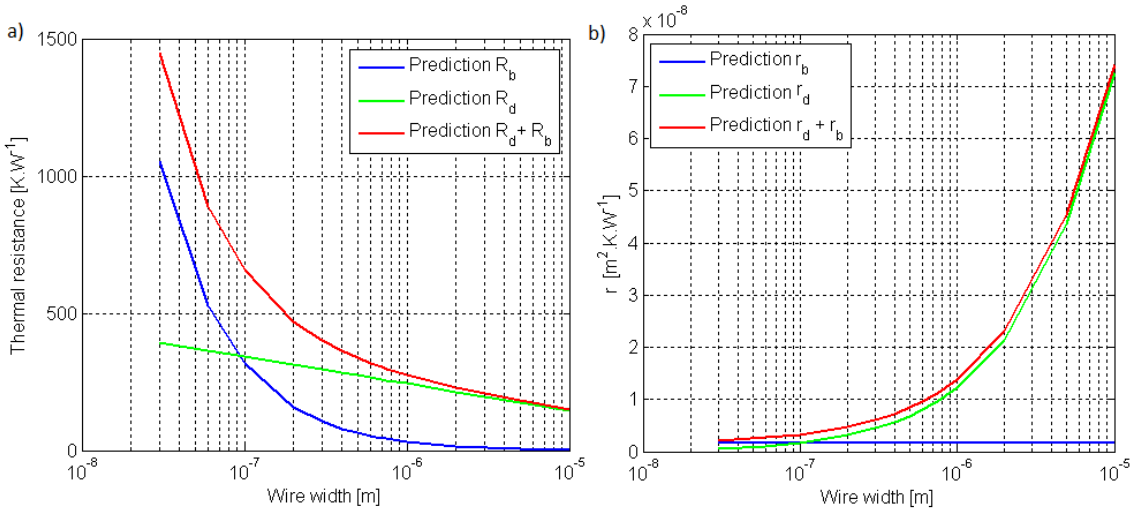

Figure 6.12. *Analytical prediction of the ballistic and diffusive components of (a) a thermal resistance and of (b) a thermal resistivity for thermal transport with a single wire.*

The deviation to the Fourier law is given by $r_{ballistic}/r_{Fourier}$, as presented in Fig. 6.13. It is concluded that the linewidth at small–scale leads to large values while the ratio is close to 2 at $2b$ = 100 nm.

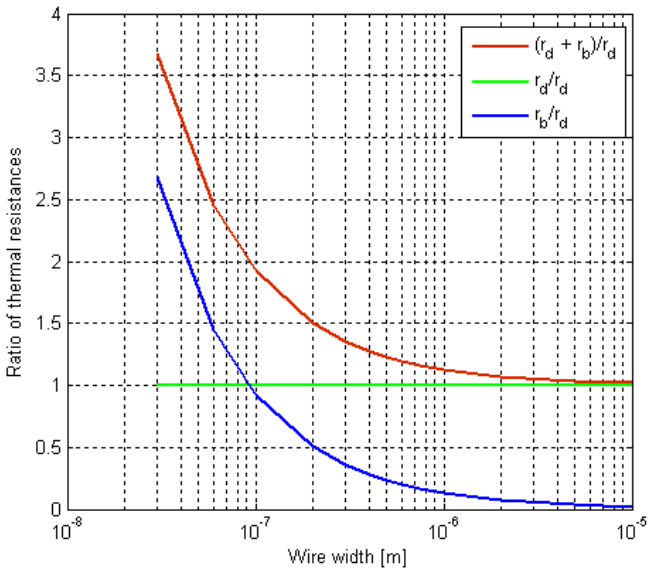

Figure 6.13. *Ratio of thermal resistvity as a function of wire width.*

b) Spherical geometry

G. Chen [6] investigated the reduction of the dissipation from embedded nanoparticles. The main result is as follows:

$$\frac{q}{q_F} = \frac{1}{1+\dfrac{4\Lambda}{3R}}. \tag{6.5}$$

The asymptotic behavior associated to this formula are

$$\begin{cases} \Lambda \to 0 \quad q \to q_F = 4\pi\lambda R\Delta T \\ \Lambda \to \infty \quad q \to 3\pi R^2 \dfrac{\lambda}{\Lambda}\Delta T \sim \pi R^2 C\upsilon\Delta T = \frac{S}{4}C\upsilon\Delta T. \end{cases} \tag{6.6}$$

The ballistic flux also depends on the surface area, but the geometrical factor is different.

Note that the cylindrical and spherical configurations introduced here deal with nanostructures embedded in a full medium. In our case, half spaces are to be considered and the flux are divided by 2, while the ratio q/q_F stays identical.

6.4.2. Equation of Phonon Radiative Transfer

In this section, we report on results obtained in the infinite 2D Cartesian geometry as a function of temperature. The equation of phonon radiative transfer (EPRT) was originally described by Majumdar [1]. He made a connection between the transport theory in dielectric thin films and the radiation theory, based on the analogy between photons and phonons as discrete wave packets of energy. The intensity of phonons can be defined as [7]

$$I_\omega(\theta,\phi,\overrightarrow{r},t) = \sum_p \upsilon(\theta,\phi) f_\omega(\overrightarrow{r},t)\hbar\omega D(\omega), \tag{6.7}$$

where the summation is over all photons polarization, $\upsilon(\theta,\phi)$ is the velocity vector in the direction of θ and ϕ within a unit solid angle, $\hbar\omega$ is the energy at which the phonons propagate and $D(\omega)$ is the density of states per unit volume. When f varies only in x–direction, the scattering term reduces the Boltzmann equation to

$$\frac{\partial f_\omega}{\partial t} + v_x\frac{\partial f_\omega}{\partial x} = -\frac{f_\omega - f_\omega^0}{\tau}, \tag{6.8}$$

where f_ω is the non–equilibrium thermodynamic distribution function depending on ω, v_x is the x component of the phonon velocity, and t is time. Multiplying Eq. 6.8 by $v\hbar\omega D(\omega)$ and using the intensity of phonon I_ω, the equation for phonon radiative transfer is obtained as

$$\frac{1}{v}\frac{\partial I_\omega}{\partial t} + \mu\frac{\partial I_\omega}{\partial x} = -\frac{I_\omega - I_\omega^0(T(x))}{v\tau(\omega, T)}, \tag{6.9}$$

where v_x is the velocity component in polar coordinate and defines by $v_x = v\mu$, so that $\mu = \cos(\phi)$ where $0 < \phi < \pi$ is the angle between the phonon propagation and the x direction. I_ω^0 is the equilibrium intensity corresponding to a blackbody intensity at temperatures below the Debye temperature. In the steady state, Eq. 6.9 can be written as

$$v\mu\tau\frac{\partial I(x,\mu)}{\partial x} + I(x,\mu) = I^0(T(x)), \tag{6.10}$$

where $I(x,\mu)$ and $I^0(T(x))$ are two unknown intensities. Once the intensity is found by solving the EPRT, the total heat flux can be determined as

$$q(x) = \int_{-1}^{1}\int_0^{\omega_D} \mu I(x,\mu) d\omega d\mu. \tag{6.11}$$

Integrating both sides of Eq. 6.10 aver all direction and frequencies, one finds

$$\int_{\mu=-1}^{\mu=1}\int_{\omega=0}^{\omega=\omega_D}\left(v\mu\tau\frac{\partial I(x,\mu)}{\partial x} + I(x,\mu)\right)d\omega d\mu = \int_{\mu=-1}^{\mu=1}\int_{\omega=0}^{\omega=\omega_D} I^0(T(x))d\omega d\mu. \tag{6.12}$$

This allows to determine the local energy.

Heat flux can also be computed within the EPRT frame in bidimensional geometry in Cartesian coordinates [8, 9]. The EPRT simulation was performed by Dr Elyes Nefzaoui (Laboratory ESYCOM at ESIEE, Paris). Accounting for the real configuration, the thickness of the substrate is 300 µm and a heat source of width 2 µm is deposited on top of the substrate in the computations. Ballistic regime is simulated within the EPRT frame considering different MFP values. In this simulation, the MFP value at each temperature is computed from the curve of silicon MFP that is presented in Chapter 1 (see Fig. 1.2). Numerical simulations are solved with the discrete ordinates method (DOM). A temperature field is presented in Fig. 6.14. For this figure, the wire temperature is set to 400 K, while the other boundaries are set to 300 K (see Fig. 6.14). A 100 × 100 grid mesh

is used. The wire is considered as a source of fixed temperature at the boundary of the computational domain here reduced to an area $L_x L_y = 6 \times 3\ \mu m^2$ which is smaller than that accounted for in Fig. 6.15.

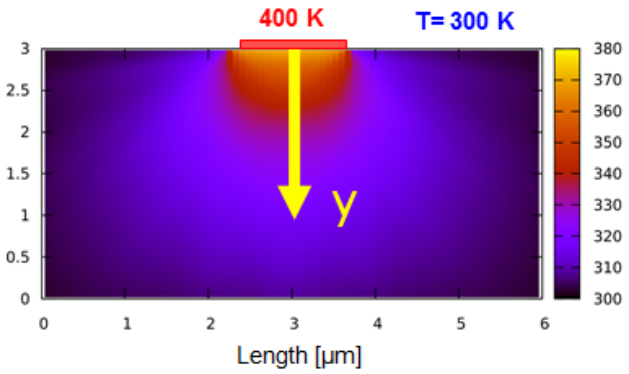

Figure 6.14. *Local temperature distribution related to the heat source size.*

The results obtained for the normalized thermal conductance with EPRT (see Fig. 6.15) show a very different temperature dependence from the thermal conductivity of the bulk silicon (see Fig. 1.5 - Si-bulk). They also deviate from the trend observed with the specific heat (see Fig. 1.4). This may be due to the inherent approximation of EPRT. A decrease is observed as in Fig. 6.6 (a), but the shape is different.

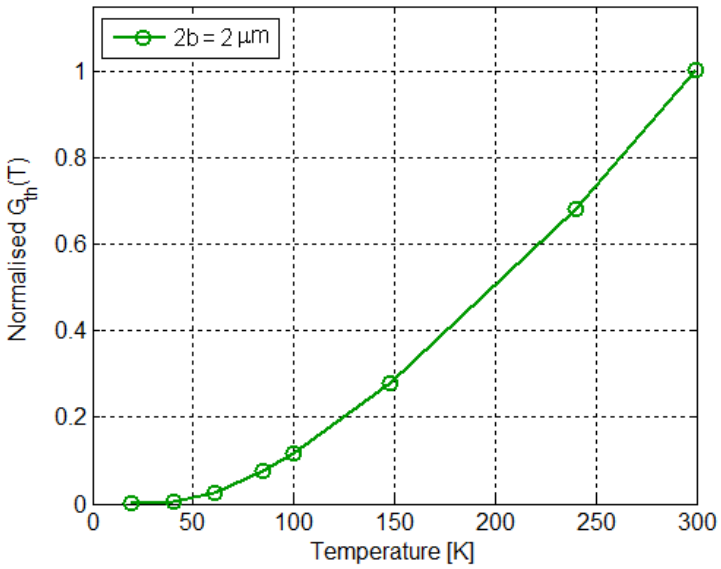

Figure 6.15. *2D numerical analysis: Normalized thermal conductance based on 2 µm wire width.*

6.4.3. Analysis of similar experiments with optical means

Recent works by Zeng and Chen [10, 11, 12, 13] and Hoogeboom-Pot et al. [14] underline the collective effects of a periodic array of wires similar to our case. We note that two approaches are possible for describing the heat dissipation reduction due to ballistic effect. Either a reduced thermal conductivity is attributed to the substrate, as in Zeng and Chen, or the ballistic reduction is treated by considering an additional boundary conductance. The second approach is that of Hoogeboom-Pot et al. Thermal resistance due to a constriction, R_c, can be approximated as a sum of a diffusive and ballistic term as shown in Eq. 6.4. In the case of Hoogeboom-Pot et al, the replace the thickness (case of a single line) by the periodicity. As their periodicity is always four times the wire width, the thermal resistance can be expressed as

$$R = \frac{45}{8\pi}\frac{1}{Cv2bL} + \frac{\ln\left(\frac{4\times 2b}{2b}\right)}{\pi\kappa L} \equiv \frac{\ln(4)}{\kappa_{eff}\pi L}, \tag{6.13}$$

where κ_{eff} is the effective thermal conductivity. The effective boundary resistivity values are 2.1 to 3.8 $\times 10^{-9}$ $\mathrm{m}^2.\mathrm{K}.\mathrm{W}^{-1}$ for wire widths range from 500 nm down to 250 nm. In comparison to the asymptotic values of Eq. 6.2, we find that TBR equals to 1.58 $\times 10^{-9}$ $\mathrm{m}^2.\mathrm{K}.\mathrm{W}^{-1}$, which is close. The obtained results of the thermal resistance and r are presented in Fig. 6.16. The shape is different to that of Siemens et al. [5] (see Fig. 6.12) where the lines are separated. When the wire width is comparable or smaller than the phonon mean free path in the substrate, the thermal resistance is predicted by Fourier law. In order to have a better understand of the ballistic effect, we calculate the effective thermal conductivity by equating

$$R_b + R_d = \frac{\ln\left(\frac{D}{2b}\right)}{\pi L\kappa_{eff}}. \tag{6.14}$$

The comparison between two configurations of the single and periodic arrays of wires is presented in Fig. 6.17.

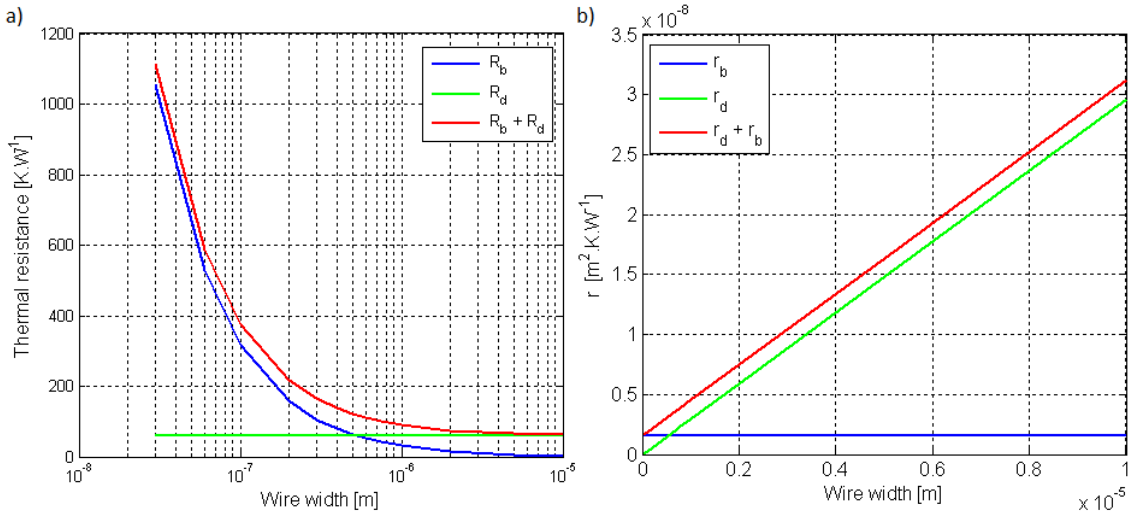

Figure 6.16. *Analytical prediction of the ballistic and diffusive components of (a) a thermal resistance and of (b) a thermal resistivity for thermal transport with periodic array of wires.*

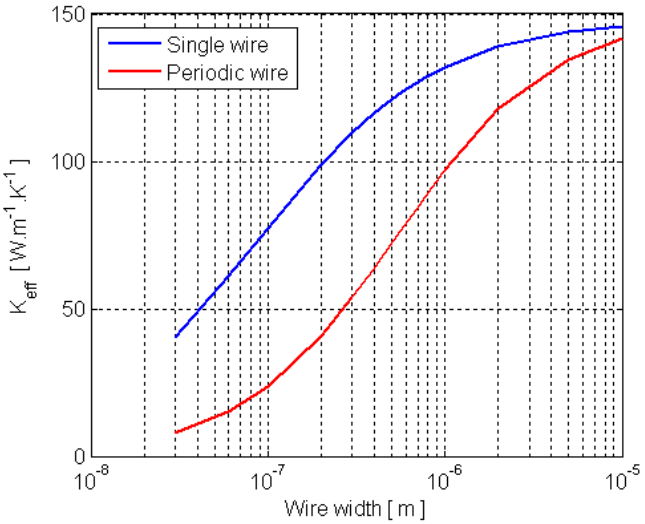

Figure 6.17. *Effective thermal conductivity of different configurations as a function of wire width.*

It is striking that the filter applied by the configurations leads to different results. In both cases, as nanowires shrink in size, the ballistic effect becomes stronger. It can be noticed that the effective thermal conductivity with the periodic nanowires is smaller than the one of the single wire. One would question the application of the periodicity in Eq. 6.13.

6.5. Discussion and comparison of the ballistic conductances

6.5.1. Comparison with FEM results

To focus on the different regimes of thermal transport, we choose here two different devices of different widths of 200 nm and 10 µm, respectively. It is useful to present the results by finding the deviation to usual Fourier law predictions. Controlling the wire widths and the temperature value down to 20 K, we can probe different ranges of Kn. Since there is more than one order of magnitude of difference between 2D and 3D FEM for diffusive regime, we made a 3D FEM based on the same geometry for both devices (DC regime). We normalized our experimental results by the 3D FEM results as presented in Fig. 6.18 and Fig. 6.19. A large reduction of thermal conductance in comparison to diffusive prediction is observed both as a function of temperature and as a function of wire width. For instance, Fig. 6.18 shows a reduction while the Knudsen number does not appear larger than one. Note that by computing Kn from Fig. 1.2, it is probably underestimated by a factor [300 / Value at 300 K in Fig. 1.2] at room temperature close to the diffusive regime, the DC simulation may also depart a bit from the 5 Hz experiment. In the ballistic regime, this effect may be less pronounced.

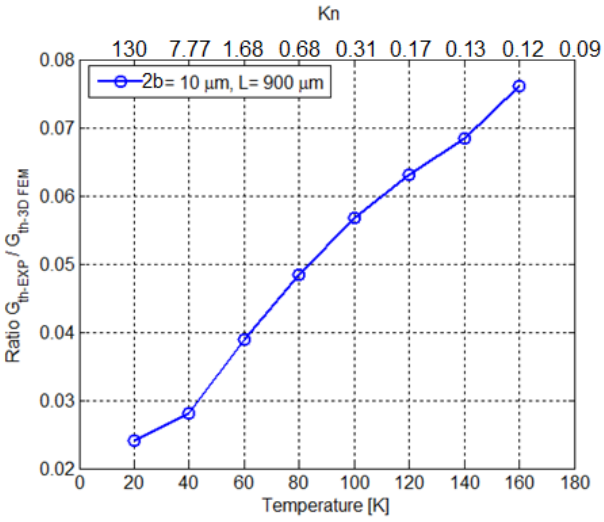

Figure 6.18. *Ratio of experimental and DC FEM thermal conductances as a function of temperature with a 10 µm wire width.*

Fig. 6.19 shows a decrease by a factor larger than ten due to the ballistic effect. This means that the contributions of phonons with different MFPs can impact strongly heat conduction. Following the asymptotic formulas given previously (see Section 6.4.1), the reduction should be inversely proportional to Kn, with a prefector depending on the geometry (cylindrical or spherical). Here the observed reduction seems to soften at low temperatures.

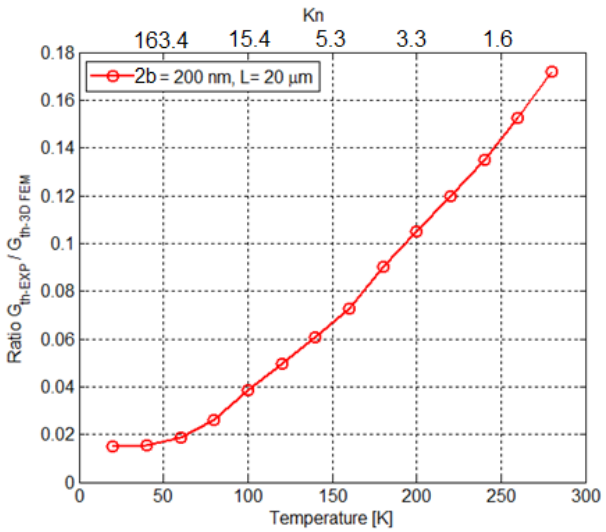

Figure 6.19. *Ratio of experimental and DC FEM thermal conductances as a function of temperature with a 200 nm wire width.*

6.5.2. Comparison with analytical formula

Our measurements are performed on different wire width and the results are compared to the analytical Eq. 6.4. Fig. 6.20 represents the comparison between both experimental and analytical results of the thermal resistance as a function of wire width. The comparison between the experimental (blue) and the prediction (red) shows a large difference especially at the microscale while at the nanoscale heat sources the results are close. As presented in Chapter 5, our measurements are performed at low frequency, this means that the spreading resistance will be larger than the substrate thickness. In this case the additional layer (PCB) to the system can impact the total thermal resistance. Prediction 2 (dashed red line) represents the thermal resistance by taking into account the additional thickness of PCB (see Chapter 3). Results obtained with the prediction 2 at the microscale becomes closer to the experimental one. Let us recall that our lines are certainly not fully

2D at low temperatures. This may not be an issue as the functional dependence in the ballistic and diffusion regimes are close (see Eqs. 6.2 and 6.6).

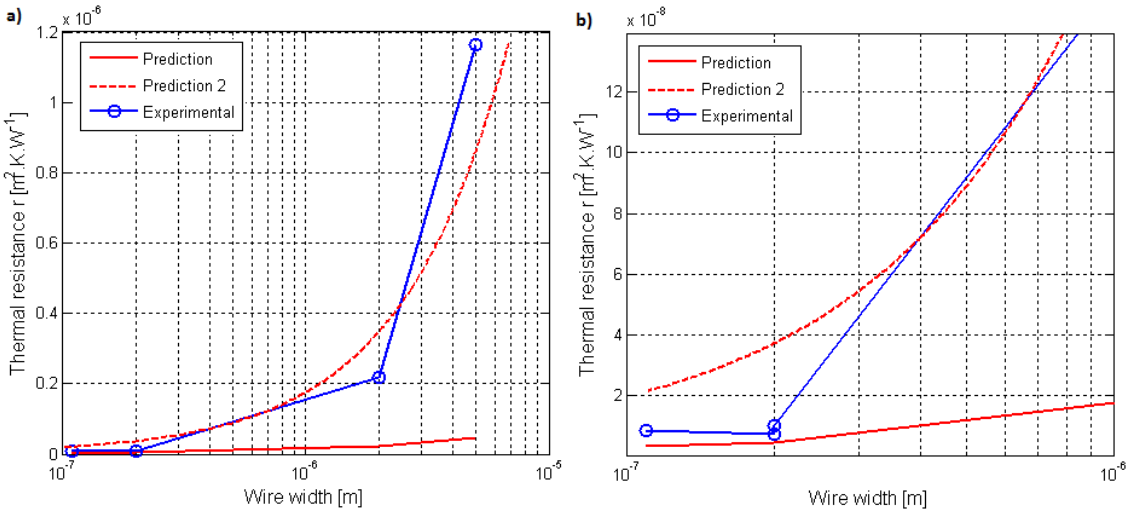

Figure 6.20. *(a) Thermal resistance as a function of wire width, (b) zoom on the smaller widths.*

Thermal resistance normalized by the predicted total resistance is presented in Fig. 6.21. For the nanoscale heat sources, the ratio is between 0.2 and 0.4 while for the microscale heat sources it is larger. Unprecise evaluation of the Knudsen number, and errors in the geometrical factors of Eq. 6.3 could be a reason. However, the ratios stay close to 1.

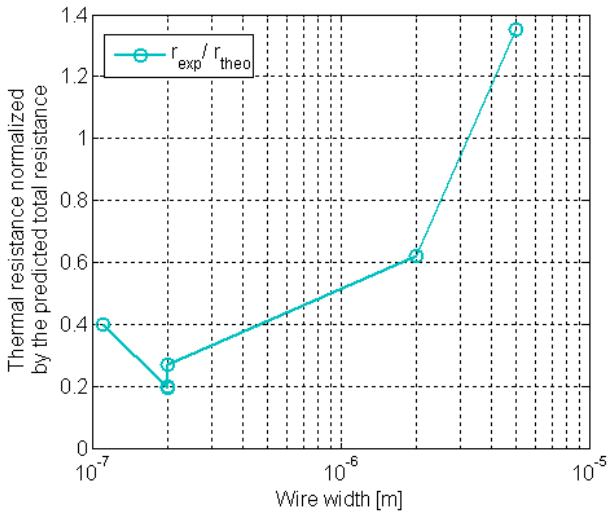

Figure 6.21. *Thermal resistance normalized by the predicted total resistance as a function of wire width.*

6.6. Conclusion

Different measurements have been performed on various device widths at room and low temperatures. We have probed a range of Knudsen numbers [27 - 12000] with different wire widths [200 nm - 10 microns] by setting the temperature in a range [20 K – 300 K], so that the ballistic regime has been clearly targeted. At room temperature, it has been demonstrated that wire surface area is key to the determination of heat dissipation. We have found an approximate logarithmic dependence of the thermal conductance on the surface. When including the widths larger than 1 μm. As a result, the observed trend is the same as that found with a diffusive simulation. The ballistic theory predicts a linear dependence on the surface in all cases.

Strikingly, the thermal conductance dependence on temperature observed experimentally is very different from the diffusive one. Results obtained with simulations including phonon transport in the ballistic regime have also shown very different temperature dependencies compared to 2D and 3D FEM calculations, and trends closer to the ones that we have found experimentally. The ratio of the experimental and DC 3D FEM thermal conductance as a function of temperature has been found to be as low as 0.02 for various widths. In comparison with previous results involving ridges, similar trends and order of magnitude are found. In the case of ridges the thermal conductance could be reduced in comparison to the wire-on-substrate geometry. Finally, we find that a Wexler approximation considering a diffusive resistance involving the layer located below the silicon substrate allows to understand our results. The diffusive resistance is indeed much larger than that of the silicon. In the end, we have shown a transition from diffusive to ballistic heat transfer for the first time for the single wire.

References

[1] A. Majumdar, J. Carrejo and J. Lai, *Thermal imaging using the atomic force microscope*, Applied Physics Letters **62**, 2501 (1993).

[2] P.-O. Chapuis, M. Prunnila, A. Shchepetov, L. Schneider, S. Laakso, J. Ahopelto and C. Sotomayor Torres, *Thermal Investigations of ICs and Systems (THERMINIC), 2010 16th International Workshop*, 1 (2010).

[3] L. Lees and C.-Y. Liu, *Kinetic theory description of conductive heat transfer from a fine wire*, (1962).

[4] G. Wexler, *The size effect and the non-local Boltzmann transport equation in orifice and disk geometry*, Proceedings of the Physical Society **89**, 927 (1966).

[5] M. E. Siemens, Q. Li, R. Yang, K. A. Nelson, E. H. Anderson, M. M. Murnane and H. C. Kapteyn, *Quasi-ballistic thermal transport from nanoscale interfaces observed using ultrafast coherent soft X-ray beams*, Nature materials **9**, 26 (2010).

[6] G. Chen, *Nonlocal and nonequilibrium heat conduction in the vicinity of nanoparticles*, Journal of Heat Transfer **118**, 539 (1996).

[7] W. Vincenti and C. Kruger, *Introduction to Physical Gas Dynamics RE Krieger*, Huntington, NY 223 (1977).

[8] R. Yang, G. Chen, M. Laroche and Y. Taur, *Simulation of nanoscale multidimensional transient heat conduction problems using ballistic-diffusive equations and phonon Boltzmann equation*, Journal of Heat Transfer **127**, 298 (2005).

[9] A. Mittal and S. Mazumder, *Generalized Ballistic-Diffusive Formulation and Hybrid SN-PN Solution of the Boltzmann Transport Equation for Phonons for Nonequilibrium Heat Conduction*, Journal of Heat Transfer **133**, 092402 (2011).

[10] R. Yang and G. Chen, *Thermal conductivity modeling of periodic two-dimensional nanocomposites*, Physical Review B **69**, 195316 (2004).

[11] L. Zeng and G. Chen, *Disparate quasiballistic heat conduction regimes from periodic heat sources on a substrate*, Journal of Applied Physics **116**, 064307 (2014).

[12] L. Zeng, K. C. Collins, Y. Hu, M. N. Luckyanova, A. A. Maznev, S. Huberman, V. Chiloyan, J. Zhou, X. Huang, K. A. Nelson *et al.*, *Measuring phonon mean free path distributions by probing quasiballistic phonon transport in grating nanostructures*, Scientific reports **5**, (2015).

[13] Y. Hu, L. Zeng, A. J. Minnich, M. S. Dresselhaus and G. Chen, *Spectral mapping of thermal conductivity through nanoscale ballistic transport*, Nature nanotechnology **10**, 701 (2015).

[14] K. M. Hoogeboom-Pot, J. N. Hernandez-Charpak, X. Gu, T. D. Frazer, E. H. Anderson, W. Chao, R. W. Falcone, R. Yang, M. M. Murnane, H. C. Kapteyn *et al.*, *A new regime of nanoscale thermal transport: Collective diffusion increases dissipation efficiency*, Proceedings of the National Academy of Sciences **112**, 4846 (2015).

Conclusions and perspectives

The goal of the work detailed in this manuscript was to investigate phonon heat dissipation from micro– to nanoscale heat sources, and especially look at the consequences of the transition from the diffusive regime to the ballistic one. The analysis was based on the fact that the thermal transport regime can be probed either by changing the characteristic length of the material or by selecting the mean free path of the heat carriers by controlling temperature. The objective was to study in particular 2D and 3D configurations.

Our measurements were performed electrically using a four–probe technique, involving the deposition of metallic wires. To design properly the experiments and to analyze them, analytical and finite–element method based numerical studies in the diffusive regime were first performed. Requirements on the wire were found: for instance, the ratio width over thickness needs to stay smaller than 20 if one wants to keep it isothermal. In addition, the length of the wire should be at least 150 times its width if the connection to the pads is not felt strongly, but the value required can be much larger (600) under strong influence. Since this ratio is not easy to achieve experimentally, smaller ratios had to be considered experimentally and it was shown that full 3D simulations may be required to analyze the experimental results. In particular, such simulations allowed highlighting that the usual plateau observed in 2D at low frequency does not necessarily exist in 3D. Finally, attention was paid to the impact of potential thermal boundary

resistances between the wire and the substrate. For large values, the sensitivity to the dissipation in the substrate is totally lost.

To meet the goals of the project, a full setup involving a liquid helium cryostat for electro–thermal measurements involving electronic connections and the automatic control of the experiments was developed. At the sample level, the investigations required the use of highly–resistive silicon wafers in order to avoid detrimental electron leakage within the substrate. A threshold for the resistivity of silicon, which depends on the deposited device sizes, was determined. Thanks to colleagues at NanoLyon-INL, wires widths ranging from 10 microns down to few tens of nanometers could be investigated. The current density flowing in the wires with the smallest cross-sections (50 nm x 20 nm in the smallest design) are very high but stay in principle large enough to avoid destruction by electromigration. The success rate of the electro–thermal experiments proved to be moderate for the narrowest wires. For the widest wires (10 microns), the electro–thermal investigations were performed on various amorphous and crystalline substrates such as sapphire and alumina. It was found that a factor 5.6 between the thermal penetration depth and the substrate thickness is sufficient to achieve a good agreement with literature values. Multilayer materials were investigated, and the results, which do not show a clear trend as a function of layer thickness, seemed in agreement with measurements performed with another technique. The technique will also be used for the characterization of membranes in the future (see Appendix C).

The dependence of electrical resistivity on temperature was investigated on micro and nanodevices. Some deviation to that theoretically predicted for monocrystalline silicon was observed: the temperature coefficient of electrical resistivity seems to become independent of temperature for the thinnest and narrowest wires. This can be attributed to the reduction of grain sizes, where electrons scatter. Measurements were performed with the narrowest wire having a width of 109 nm. An approximate logarithmic dependence on wire surface was found for the thermal conductance of the largest wire, and the aspect ratio did not show a clear trend. Estimations of the Knudsen number were larger than 1000 for various wire widths at low temperature, so the ballistic regime was clearly investigated. The thermal conductance dependence on temperature showed a behavior very different from the one predicted by the diffusive behavior, which resembles more the trend of the specific heat. This behavior was also closer to the one observed in 2D simulations performed within the frame of the Equation of Phonon Radiative Transfer. The ratio with the Fourier prediction was found to be close to 0.02 for various widths. Finally, we noticed that the values of thermal conductance obtained are close to those

obtained in an earlier experiment involving a ridge below the heater.

The results obtained here will be useful in electronics, in the field of thermal packaging and may be useful for the future design of 2D–3D thermoelectric devices. There are also a number of perspectives opened by this work.

On the practical side, the setup is ready and usual 3ω measurements can be performed. To improve the control of experiment, especially for the narrowest wires, it would be important to study longer wires: the results would be more easily compared to the Cartesian 2D ideal configuration. A shorter thermalization time would also be helpful. In addition, it could be interesting to perform measurements both in the real static regime (not low–frequency) or at higher frequencies to extend the range of the probed volume. Currently, it is however not expected that the frequency range will be able to overlap with that of the optical pump–probe experiments (GHz).

Related to the physics studied, we note that the impact of the thermal boundary resistance in the devices could be studied, while it can dictate the overall heat transfer in some cases. Some theoretical analysis should be devoted to this point, as both the ballistic conductance and thermal boundary resistance are expected both to follow the behavior of the heat capacity. Splitting their effects appears therefore difficult, but is an important challenge. Moreover, the ballistic regime will still deserve investigations. In our work, we considered only a single nanowire. Two groups recently reported the observation that the thermal conductance of an array of wires dissipates more than what would be found by summing the dissipation of each wire. Our technique allows studying the same issue with an electrical means, where no dynamics may complicate the analysis. Other geometries could also be envisaged, with for instance a smaller heating part due to a local constriction. Note that the analysis here was always performed as a function of the average mean free path, while materials possess a distribution of mean free path. It could be useful to consider it to be more quantitative.

Appendices

APPENDIX A

Central resistance of a 4–terminal device

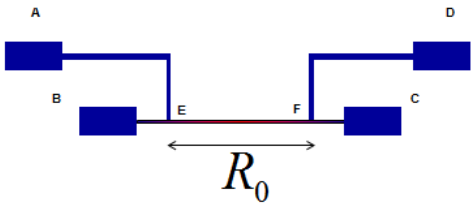

Figure A.1. *4-terminal resistance device*

To calculate the resistance of the central wire, we have to measure first the resistance values of the following branches: $R_{AD}, R_{AB}, R_{AC}, R_{BC}, R_{CD}, R_{BD}$ (see Fig A.1), using an Ohm–meter. The matrix X is defined by

$$\begin{pmatrix} R_{AD} \\ R_{AB} \\ R_{AC} \\ R_{BC} \\ R_{CD} \end{pmatrix}$$

We then solve the equation

$$MX = B. \tag{A.1}$$

M is defined as follows

$$\begin{pmatrix} 1 & 1 & 1 & 0 & 0 \\ 1 & 0 & 0 & 1 & 0 \\ 1 & 1 & 0 & 0 & 1 \\ 0 & 1 & 0 & 1 & 1 \\ 0 & 0 & 1 & 0 & 1 \end{pmatrix} X = \begin{pmatrix} R_{AD} \\ R_{AB} \\ R_{AC} \\ R_{BC} \\ R_{CD} \end{pmatrix}$$

B =[R_{AD}, R_{AB}, R_{AC}, R_{BC}, R_{CD} , R_{BD}]
Only 5 data are required to determine R_0. Then additional data R_{BD} can be used to check if there is a

X=inv(M)B
R_{AE}=X(1)
R_{EF}=X(2)
R_{FD}=X(3)
R_{EB}=X(4)
R_{FC}=X(5)

Calculating the value of the aforementioned resistance, the resistance of the central wire can be obtained as $R_0 = R_{EF} = X(2)$.

APPENDIX B

Temperature dependence of electrical resistivity of silicon

The electrical conductivity is

$$\sigma = \frac{1}{\rho} = n_i e \mu_e + p_i e \mu_h, \tag{B.1}$$

where p_i is the concentration of holes, n_i is the concentration of electrons, μ_h is the hole mobility in $[\mathrm{m}^2.\mathrm{V}^{-1}.\mathrm{s}^{-1}]$, μ_e is the electrons mobility in $[\mathrm{m}^2.\mathrm{V}^{-1}.\mathrm{s}^{-1}]$, the subscript i means intrinsic and e is electric charge. When undoped, the number of electrons is equal to the number of holes, because thermal excitation of electrons leaves behind a hole in a valance band. Thus the concentration can be expressed as

$$n_i = p_i = 2\left(\frac{k_B T}{2\pi\hbar^2}\right)^{3/2} (m_e m_h)^{3/4} e^{\frac{-E_g}{2k_B T}}, \tag{B.2}$$

where E_g is the band gap energy, m_e and m_h are the effective masses of electrons and holes respectively. The previous equation can be rewritten as

$$n_i \approx (n_0 N_d)^{1/2} e^{\frac{-E_g}{2k_B T}}, \tag{B.3}$$

with $n_0 = \left(\frac{k_B T}{2\pi\hbar^2}\right)^{3/2}$, N_d being the concentration of electrons. The density of holes at equilibrium can be expressed as

$$p_0 = \frac{n_i^2}{N_d}. \tag{B.4}$$

The carrier mobilities can be determined by analyzing the scattering mechanism due to the ionized impurities and interaction with either acoustic or optical phonons. According to Matthiessen's rule, the mobility of the silicon substrate can be determined from compound mobilities. Based on the Caughey-Thomas model, the temperature dependence of the mobilities can be expressed as

$$\mu_h(T) = \mu_{min} + \frac{\mu_{min}\left(\frac{300}{T}\right)^{\theta_1} - \mu_{min}}{1 + \left(\frac{N_d}{N_{ref}\left(\frac{T}{300}\right)^{\theta_2}}\right)^{\phi.}}, \tag{B.5}$$

where the parameters are defined for Table B.1.

Parameters	Value
$\mu_{max}(\mathrm{cm}^2.\mathrm{V}^{-1}.\mathrm{s}^{-1})$	470
$\mu_{min}(\mathrm{cm}^2.\mathrm{V}^{-1}.\mathrm{s}^{-1})$	37.4
N_{ref}	$3\ e^{16}$
$\phi.$	1.05
θ_1	-0.57
θ_2	-2.23

Table B.1. *Parameters used in Caughey-Thomas model for calculating the holes mobilities for Si.*

The temperature dependence of hole mobility is shown in Fig. B.1. The electrical resistivity can be computed theoretically from the mobility and compared to the experimental results found in Chapter 4.

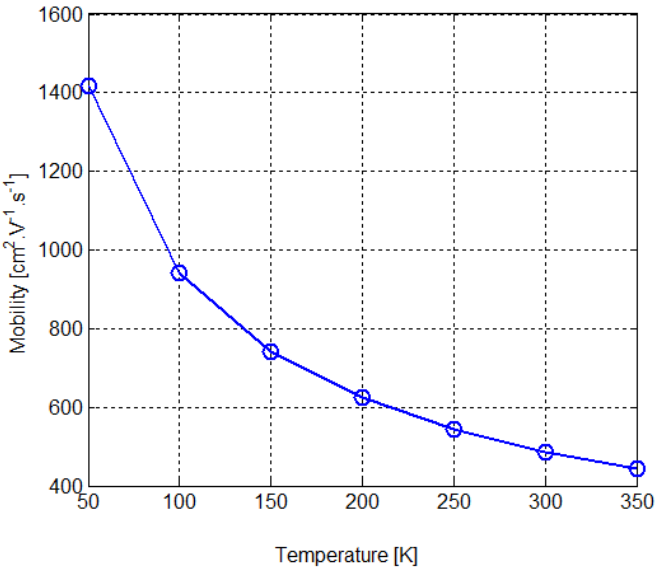

Figure B.1. *Temperature dependence of hole mobility.*

APPENDIX C

3ω structures for measurement of SiN thermal conductivity

Thermal conductivity measurement of a thin film can be performed by means of a membrane on which the 3ω device stands. This requires some adaptation from the bulk technique. Such design has been implemented in the frame of a collaboration with EPFL (Dr E. Lemaire and D. Briand).

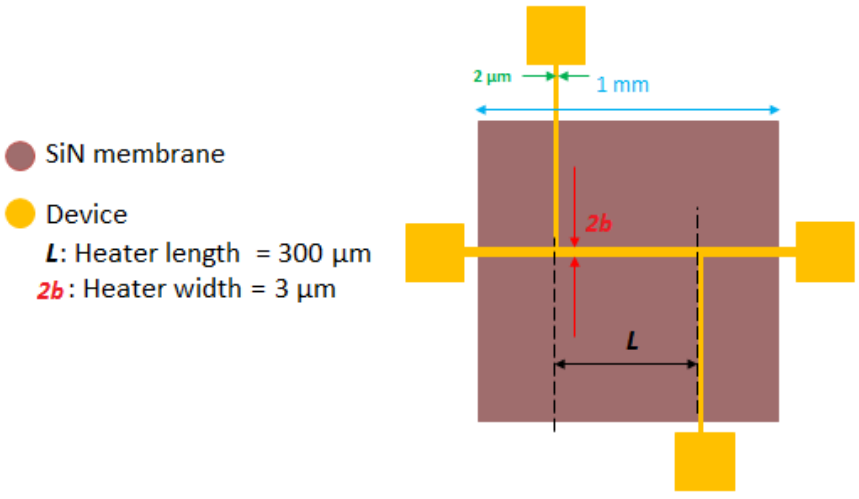

Figure C.1. *Top view of a four-probe device on top of SiN membrane.*

a)

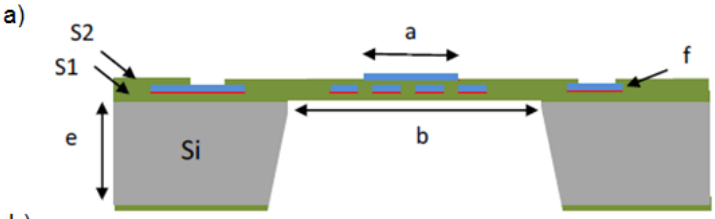

b)

	Materials	Thickness	Main dimensions
Top metal layer pad	Ta + Pt or Ti + Au	d = 6 nm + 50nm or d = 15 nm + 150nm	Shape radius = a a = 50 µm
Membrane	SiN (layer S1) + SiN (layer S2) +	S1 = 500 nm S2 = 500 nm	Square b*b b = 1 mm
Heater	Ta + Pt	F = 15 nm + 225 nm	220 x 220 µm^2 to 440 x 440 µm^2-
Chip	Si	e = 390 µm	3 x 3 mm^2

Figure C.2. *(a) Schematic cross section of the sample. (b) Example of dimensions and thickness of the chip.*

Abstract

The context of this PhD is the reduction of sizes involved in material development and the confinement of heat in modern devices, which are known to lead to the apparition of hot spots. The goal is to investigate heat conduction from micro- to nanoscale wide Joule-heated wires standing on flat layered materials. A particular focus is given to the analysis of phonon heat dissipation when departing from the well-known Fourier diffusive conduction and entering the ballistic regime.

The manuscript starts with a summary of the main observed effects on the effective thermal conductivity in nanoscale materials, especially in light of the values of thermally-averaged phonon mean free paths and the associated Knudsen number. Then the advantages and drawbacks of various measurement techniques are discussed. The analysis of the experimental configuration requires 2D analytical and 3D finite-element method based numerical studies of diffusive heat conduction from a finite source into a medium. Limitations of the 3ω method due to wire length, substrate geometry and thin oxide layers are highlighted. The electro-thermal setup developed and the procedure used to deposit the devices on top of the samples are then detailed. A set of well-known materials with mean free path ranging from few nanometers to hundreds of nanometers is characterized with microwires. The thermal conduction properties of multilayer materials are investigated. Heat dissipation from finite sources on top of silicon substrates is then measured as a function of temperature. The mean free path is known to become large when temperature decreases. As a result, this configuration provides clues for understanding heat conduction from ballistic sources. The observed behavior is very different from the one predicted by Fourier's law and shows a strong reduction of the dissipation. It is found that the results are comparable to earlier measurements involving ridges. They are analyzed with various levels of approximations of predictions using the Boltzmann transport equation.

The results obtained may be useful in many fields, in particular for electronics and thermoelectric designs.

Keywords: nanoscale thermal transport, microscale heat transfer, phonon heat conduction, thermal conductivity, four–probe electrical technique